

Mapping Dark Matter and Dark Energy

by

Anna Kathinka Dalland Evans

Submitted
in partial fulfilment of the requirements
for the degree of

Philosophiae Doctor



Institute of Theoretical Astrophysics
Faculty of Mathematics and Natural Sciences
University of Oslo

Oslo, Norway

March, 2009

Preface

In science one tries to tell people, in such a way as to be understood by everyone, something that no one never knew before. But in poetry, it's the exact opposite.

Paul Dirac

In astronomy, we learn about the universe by studying the light that is emitted from distant stars and galaxies. Light rays travel through the far reaches of space until they arrive here on Earth and are recorded by our telescopes and other observation equipment. The light we observe can give information about objects located millions of light years away, but it also contains information about what lies between us and these objects. Whether it be interstellar dust or strong gravitational fields, the light rays are affected and carry the signatures back for us to unscramble. As a twist of fate, it appears that most of what is out there is actually invisible, or dark.

Chapter 1 gives a brief introduction to cosmology and the general physical framework within which research for this thesis has been conducted, the so-called standard - or concordance - cosmological model. This is the simplest model which is in general agreement with observations. However, the two major constituents of the standard model remain enigmatic. Cosmologists call them dark matter and dark energy, and in this thesis we are concerned with investigations into both of these most mysterious parts of the Universe.

The focus of Chapter 2 is the dark matter. How do we know that it exists and what do we actually know about it so far? In Chapter 3 I describe some important techniques for mapping out the dark matter distribution at different scales, based on a natural occurring phenomenon known as gravitational lensing. Specifically, the shapes and possible ellipticities of galaxy cluster dark matter halos are discussed, as observed in data from galaxy surveys (paper I) and from large-scale simulations (paper II).

In Chapter 4 I give an introduction to the other – and perhaps even more mysterious – dark component of the Universe: dark energy. Many different models of this largely unknown but major contributor to the energy budget of the Universe have been suggested. As one way of classifying dark energy models, a set of so-called statefinder parameters were introduced in 2004. In paper III we investigate the usefulness of these parameters by applying them to real and simulated supernovae observations.

Acknowledgements

I would like to thank my supervisor, prof. Øystein Elgarøy, for the opportunity to have all this fun doing research while actually getting paid for it, and for his bravery in getting me started (and forcing me to finish!) on a topic which was partly new territory for him, but very exciting to me.

My biggest, biggest thanks to the truly amazing dr. Sarah Bridle who has spent an enormous amount of time teaching me how to do science in general and weak lensing in particular. Your dedication and humour have been inspiring and your enthusiasm contagious. And thank you for letting me bombard you with frantic e-mails, you're a star!

I spent the autumn of 2005 at the Astrophysics Group at University College London, and would like to thank prof. Ofer Lahav for making this visit possible. Many thanks to all the people in this group for making my stay not only productive but also extremely enjoyable: special thanks to drs. Rassat, Lintott, Dunkley and Bridle for cosmo-conversations, dinners, concerts at the Barbican, haggis(!) and whisky tastings.

A ton of thanks to dr. Laurie Shaw, who not only provided excellent large-scale simulations but also many interesting discussions as well as a huge effort in speed-finishing paper II.

I would also like to thank all my office (in)mates at the Institute of Theoretical Astrophysics (ITA) in rooms 502 and 201 during the long haul that working on this thesis has sometimes been. Special thanks are due to dr. Morad Amarzguioui who was the very best of room companions before he unfortunately finished his phd and was lost to the world of industry.

Also to everyone eating lunch in the ITA kitchen at 12.30: thank you for many many diverting conversations on important subjects such as which side of a crispbread is up, whether glass is a liquid or a solid, and the assumed popularity of ice cream with goat cheese bits in it.

From the bottom of my soul, thanks to all the beautiful, hard-working people in my daughter's kindergarten who allow me to relax and concentrate on a daily basis! And to Nerina for providing me with chocolate in the crazy final stages of writing.

My most personal thanks to my husband Terje who takes care of me, persuades IDL to work and makes life fun, and to our wonderful daughter Ronja, who reminds me every day that funny-looking stones and deep puddles are more important things in life than a phd.

List of papers

Paper I: Evans, A. K. D., Bridle, S.,
Detection of dark matter halo ellipticity from lensing by galaxy clusters in SDSS,
Astrophysical Journal **695** (2009), 1446-1456

Paper II: Evans, A. K. D., Shaw, L., Bridle, S.,
Predictions of dark matter halo ellipticities measured by lensing,
To be submitted to Astrophysical Journal (Ap.J.)

Paper III: Evans, A. K. D., Wehus, I. K., Grøn, Ø., Elgarøy, Ø.,
Geometrical constraints on dark energy,
Astronomy and Astrophysics, **430** (2005), 399-410

Contents

Preface	i
Acknowledgements	iii
List of papers	v
 I Introduction	 1
1 Cosmological Framework	3
1.1 A <i>very</i> brief history of cosmology	3
1.2 The concordance model	4
1.2.1 Theory	6
2 Invisible Universe I: Dark Matter	9
2.1 Evidence for dark matter	9
2.2 Different types of dark matter	11
3 Probing the unseen with gravitational lensing	13
3.1 Classifications	15
3.2 Basic lensing theory	18
3.3 Weak lensing by gravitational clusters (paper I)	22
3.3.1 The glow that illuminates: Ellipticity and shear	24
3.3.2 The glare that obscures: Systematic errors	28
3.4 Predictions of weak lensing from N -body simulations (paper II) .	29
4 Invisible Universe II: Dark Energy	31
4.1 Evidence for dark energy	31

4.2	Cosmological models with dark energy	33
4.3	Investigating the statefinder parameters (paper III)	34
	Bibliography	44
	II Papers	45

Part I

Introduction

Chapter 1

Cosmological Framework

1.1 A *very* brief history of cosmology

On a philosophical level, cosmology is a field in which researchers' ultimate aims are to answer the fundamental questions: Where do we come from? How did it all begin? How will it all end?

In ancient times, people looked to philosophers, historians and story-tellers when they wanted to know the workings of the world. Throughout the Middle Ages, the appeal to the authority of Aristotle was the answer to questions of why natural phenomena occurred. Why does a stone fall to the ground? Because it is attracted to its natural element and wants to return to it. Why does a feather fall more slowly than a stone? Because its natural element is the air. Aristotelian views, such as the final cause, *telos*, of things (the final cause of a pen is to produce good writing), lasted long into the Renaissance.

Towards the end of the Renaissance there was a period of great activity and change in the natural sciences; Copernicus, Kepler, Newton and Galileo all lived and worked in this time period, which came to be known as 'the scientific revolution' (16th–17th centuries). It was a time which dramatically changed the way we look at problem-solving.

One of the main outcomes of the Scientific Revolution was to supplant Aristotle's final cause with a mechanical philosophy; that all natural phenomena can be explained by physical causes. Gradually, the Sun replaced the Earth as the centre of the Universe. The idea that heavy bodies by their nature move down while lighter bodies naturally move up, was replaced by the idea that all bodies – both on Earth and in the heavens – move according to the same physical laws. The concept that a continued force is necessary to keep a body on motion, was abandoned by the inertial concept that motion, once started, continues indefinitely unless acted on by another force. For a brief but comprehensive review, see [1].

Yet the most remarkable development of this time was not a specific discovery but a revolutionary new method of investigation. The new scientific method focussed on mathematics as a language in which to formulate the laws of physics, and empirical research as a reference frame from which to make hypotheses and

conduct experiments. Experimental outcomes replaced Aristotle’s teachings as the new authority for truth.

Cosmology is the astrophysical study of the history, structure, and dynamics of the Universe. Hence it was, for much longer than other branches of physics and astronomy, a field more dominated by speculation and conjecture than by observations and experiments. There were few possibilities for the accuracy of tests and predictions starting to emerge in other disciplines in science laboratories around the world. In very recent years, however, cosmology too has entered the world of precision sciences.

In November 1989, NASA launched the satellite COBE (COsmic Background Explorer) to investigate the already detected [2] cosmic microwave radiation (CMB) predicted by the hot Big Bang theory. COBE confirmed that the CMB spectrum is that of a nearly perfect blackbody with a temperature of $2.725 \pm 0.002\text{K}$. Subsequently, COBE data revealed tiny variations of temperature in different directions on the sky, at a level of one part in 100 000. These variations offer important clues to early structure formation in the Universe. For these discoveries, John C. Mather and George F. Smoot were awarded the Nobel Prize in Physics in 2006. The Nobel committee wrote in a public statement [3] that “[...] *the COBE-project can also be regarded as the starting point for cosmology as a precision science: For the first time cosmological calculations [...] could be compared with data from real measurements. This makes modern cosmology a true science [...]*”.

In the 20 years that have passed since the launch of COBE, cosmology has indeed grown to a true precision science that now places strong boundary conditions on cosmological models.

In this chapter I will give a very brief presentation of the cosmological framework that is now considered the standard concordance cosmological model, and within which the work of this thesis has been conducted.

1.2 The concordance model

concord —

From The Concise Oxford Dictionary

noun

1 agreement or harmony between people or things.

The Big Bang theory is today the sovereign cosmological model for the initial conditions and subsequent evolution of the Universe. Ironically, its now famous nickname originated by a man who spent a great deal of his life supporting the once competing steady state model. Sir Fred Hoyle (1915-2001) unwittingly coined the name in a radio broadcast in 1949, when he stated that current evidence was in conflict with theories that required all matter to have been created in ‘one Big Bang’ [4].

The Λ -Cold Dark Matter (Λ CDM) model is often referred to as the standard, or concordance, model in Big Bang cosmology. It is the simplest model that is in general agreement with observations. Based on overwhelming corroborating evidence from many different types of observations, it is believed that this model

describes the general characteristics and evolution of the Universe very well.

The Greek letter Λ stands for the cosmological constant, which is the dark energy term believed to be causing the expansion of the Universe to accelerate. The idea that the Universe is accelerating became generally accepted after 1998, when studies of large data sets of supernovae type Ia (SNIa) indicating this were published by two independent groups [5, 6]. Cold dark matter denotes that most of the matter in this model of the Universe is of a type that cannot be observed by its electromagnetic radiation. In addition to being dark, this matter component is non-relativistic (i.e. cold). In Chapters 2 and 4 I will describe the dark matter and dark energy in a little more detail.

In the Λ CDM model, the Universe is spatially flat, meaning that it has an energy density equal to the critical density. The critical density today is given by

$$\rho_{\text{crit},0} = \frac{3H_0^2}{8\pi G} . \quad (1.1)$$

The subscript ‘0’ indicates measurements of the quantity today, as opposed to at earlier times (i.e higher redshifts) in the history of the Universe. H_0 is the value Hubble parameter today, recent measurements giving $H_0 \sim 72 \pm 3 \text{ km s}^{-1} \text{ Mpc}^{-1}$ [7]. The critical density today is equivalent to a mass density of $9.9 \times 10^{-30} \text{ g/cm}^3$, which is equivalent to only ~ 6 protons per cubic meter [7].

Based on observational evidence, there is currently general agreement in the cosmological community that our Universe closely resembles the Λ CDM model. The COBE results [8] provided increased support for the Big Bang scenario in which the universe has expanded from a primordial hot and dense initial condition at some finite time in the past, and continues to expand to this day. The Big Bang is the only theory that predicts the kind of cosmic microwave background radiation measured by COBE. Anisotropies in the cosmic microwave background temperature were later measured to greater precision with data from the Wilkinson Microwave Anisotropy Probe (WMAP) satellite [9] with the conclusion that the Universe is flat with only a 2% margin of error. From this it follows that the density of the Universe equals the critical density given by Eq. 1.1.

Several probes of the large-scale matter distribution such as the Sloan Digital Sky Survey (SDSS) [10] show that the contribution of standard sources of energy density, whether luminous or dark, is only a fraction of the critical density. Combinations of the CMB and large-scale structure show that an extra unknown component, referred to as dark energy, is needed to explain the observations [11, 12]. The dark energy is believed to cause the observed acceleration of the expansion of the Universe.

For completeness, I mention here that the concordance model has 6 basic parameters [13]. The Hubble parameter H_0 determines the rate of expansion of the universe. Density parameters for baryons, dark matter and dark energy are given as Ω_b , Ω_m and Ω_Λ , which are ratios of these densities to the critical density: $\Omega_m = \rho_m / \rho_{\text{crit}}$ etc. Because the Λ CDM model assumes a flat Universe, the density of dark energy is not a free parameter but is related to the other densities by

$$\Omega_\Lambda = 1 - \Omega_b - \Omega_m . \quad (1.2)$$

The optical depth τ to reionization determines the redshift, and hence the time, when the Universe was reionized due to the formation of stars and galaxies that radiated with enough energy to ionize neutral Hydrogen. Information about density fluctuations is determined by the amplitude of the primordial fluctuations from cosmic inflation A_s and the spectral index n_s , which measures how the fluctuations change with scale ($n_s = 1$ corresponds to a scale-invariant spectrum).

Although the concordance model gives a consistent description of the dynamics of the Universe, two large mysteries remain. The ordinary (baryonic) matter that makes up our bodies, everything we see around us, the planets and stars, seems to be a very small fraction of the total energy density in the Universe. The concordance model seems to require the presence of about five times as much dark matter (see Chapter 2) and a resounding fifteen times more dark energy (see Chapter 4). Understanding these two major components of the Universe is the primary goal of cosmology today.

Extensions of the simplest Λ CDM model allow the dark energy component to vary with time. It is then sometimes referred to as quintessence, borrowed from the ancient Greeks who used the term to describe a mysterious ‘fifth element’ - in addition to air, earth, fire and water.

1.2.1 Theory

Einstein’s field equations form the basis for our interpretation of the Universe:

$$R_{\mu\nu} - \frac{1}{2}g_{\mu\nu}\mathcal{R} = \frac{8\pi G}{c^4}T_{\mu\nu} \quad (1.3)$$

The left-hand side of Eq. 1.3 expresses geometry by means of the Ricci tensor $R_{\mu\nu}$ and the Ricci scalar \mathcal{R} . These are given by the form of the metric of the space-time $g_{\mu\nu}$. The right-hand side of Eq. 1.3 corresponds to the matter content of the Universe, specified by the energy-momentum tensor $T_{\mu\nu}$.

To apply Einsteins general relativity to the dynamics of the Universe as a whole, we need to make an assumption about how matter is distributed. The simplest assumption is that the matter distribution in the Universe is homogeneous (i.e. the same everywhere) and isotropic (i.e. the same in all directions) when averaged over very large scales. This is called the Cosmological Principle. In a homogeneous and isotropic Universe filled with one or more perfect fluids, we can describe the metric through the Robertson-Walker line element which defines the distance between two infinitesimally separated points:

$$ds^2 = -dt^2 + a^2(t) [d\omega^2 + f_K(\omega)^2(d\theta^2 + \sin^2\theta d\phi^2)] , \quad (1.4)$$

where units have been chosen so that $c = 1$. (ω, θ, ϕ) are comoving spherical polar coordinates, ω is the comoving radial distance, and $f_K(\omega)$ depends on the curvature K of the Universe. For a flat model, $f_K(\omega) = \omega$. The scale factor $a(t)$ gives the rate of expansion of the Universe and is expressed in terms of the redshift as

$$\frac{a}{a_0} = (1 + z)^{-1} . \quad (1.5)$$

That is, if we observe at a redshift of e.g. $z = 1$, the scale factor at that time was only half of the value it has today.

From Einstein's field equation for a homogeneous and isotropic Universe we can derive the Friedmann equations for the time derivatives of the scale factor:

$$\frac{\ddot{a}}{a} = -\frac{4\pi G}{3}(\rho + 3p) \quad (1.6)$$

$$H^2 = \left(\frac{\dot{a}}{a}\right)^2 = \frac{8\pi G}{3}\rho - \frac{k}{a^2} . \quad (1.7)$$

The density ρ is the sum of all contributing parts (baryons, radiation and cosmological constant-term):

$$\rho = \rho_m + \rho_{rad} + \rho_\Lambda . \quad (1.8)$$

To produce acceleration, we must have $\ddot{a} > 0$. For Eq. 1.6 this means that

$$p < -\frac{\rho}{3} . \quad (1.9)$$

Since density is a positive quantity, this means that the dark energy component must have negative pressure. In terms of the equation of state,

$$w = \frac{p}{\rho} , \quad (1.10)$$

we can write the general density development as

$$\rho \propto a^{-3(1+w)} , \quad (1.11)$$

where the value of w will depend upon the component of the Universe. For baryonic matter, the pressure is essentially zero giving $w = 0 \Rightarrow \rho_m \propto a^{-3}$. For radiation, $w = 1/3$ and $\rho_{rad} \propto a^{-4}$. For a cosmological constant, $w = -1$ giving $\rho_\Lambda = \text{constant}$. So for baryonic matter and radiation, the density decreases with time but the density of the cosmological constant-term remains unchanged with time.

Chapter 2

Invisible Universe I: Dark Matter

The concordance model described in Chapter 1 gives a consistent description of the dynamics of the Universe that agree well with most of the existing observations. However, the model seems to demand the presence of large amounts of new and exotic types of energy and matter, and much of the effort of cosmologists today is directed towards understanding the so-called dark matter and dark energy. In this chapter the focus is on dark matter, while in Chapter 4 I describe the dark energy.

Although the idea of dark matter dates back to the 1930's, its true nature still eludes cosmologists. Dark matter exhibits the same gravitational attraction as ordinary matter, but it does not interact electromagnetically at all. So it is invisible, but can still be detected through its gravitational effects.

2.1 Evidence for dark matter

Most of our knowledge of the Universe comes from electromagnetic waves emitted by astronomical objects. Dark matter, on the other hand, does not interact with the electromagnetic spectrum. It is completely invisible, it does not emit, absorb or reflect light on any frequency. In fact, it does not interact with ordinary matter at all, and hence it is very difficult to detect. The evidence that dark matter actually exists comes from its gravitational effect on other objects that we *can* observe. Visible matter behaves in ways that cannot be explained in standard gravitational theories without additional, invisible matter.

Individual galaxies have been found to contain dark matter. In visible light, galaxies generally show a massive core, see Fig. 2.1. If the visible matter dominated, one would therefore expect that the rotational velocity of stars in the galaxy would decrease with radial distance from the core. Stars towards the edge of the spiral galaxy in Fig 2.1 would be rotating slower than stars closer to the centre. However, the velocity is found [14] to be very nearly constant as a function of radial distance from the centre of the galaxy. This implies that the galaxy that we see is embedded in a gigantic halo of dark matter, a halo which



Figure 2.1: The Andromeda galaxy in visible light. Image credits: John Lanoue.

extends far beyond the edges of the visible galaxy. The dark matter needed to uphold the observed rotational curves of stars is generally found to be five to ten times the mass of the visible galaxy.

Galaxy clusters are large conglomerations of 50-1000 galaxies, each galaxy containing hundreds or thousands of million stars. When observed visually, clusters appear to be collections of galaxies held together by mutual gravitational attraction. However their velocities are too large for the galaxies to remain gravitationally bound by their mutual attractions, implying the presence of the invisible mass component. More than 50 years ago, Fritz Zwicky was the first to find evidence that dark matter exists. His findings in a study of the Coma cluster [15] showed that the cluster would disperse if the entire attractive gravitational force only came from the luminous, visible matter.

X-ray studies have revealed the presence of large amounts of intergalactic gas in clusters. Since this gas is very hot, around 10^8K , it emits X-rays. The total mass of this gas is greater than that of the galaxies by roughly a factor of two. However this is still not enough mass to keep the galaxies in the cluster.

An effect known as gravitational lensing can be used to predict how much material there must be in a cluster to create its gravitational field. It turns out that the total mass deduced from this measurement is much larger than the ordinary matter of the stars and gas combined. In a typical cluster roughly 5% of the total mass is in the form of visible galaxies, 10% is in the form of hot X-ray emitting gas and the remainder is dark matter. It appears that the visible galaxy clusters are embedded in proportionally huge dark matter halos. In Chapter 3 we look at gravitational lensing in more detail, a very powerful tool with which to probe the dark matter distribution in the Universe.

Because dark matter seems to be the dominating matter component in the Universe, it is desirable to find out how it is distributed in the Universe. In Fig. 2.2 results from the Millennium Simulation by the international Virgo consortium are reproduced [16, 17]. This is the largest simulation ever of cosmic structure growth. It uses more than 10 billion particles to trace the evolution of the matter distribution in a cubic region of the Universe over 2 billion light-years on a side.

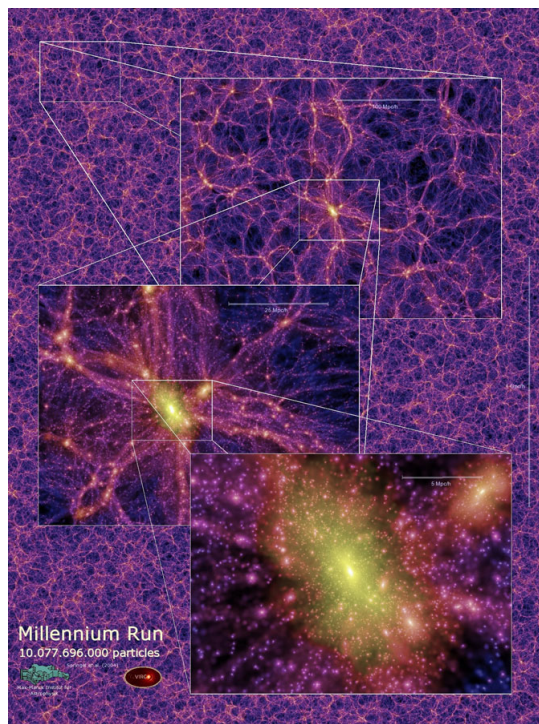


Figure 2.2: The distribution of dark matter in the universe on different scales. The figure shows a projected density field for a $15h^{-1}$ Mpc thick slice of the redshift $z = 0$ output. The largest scales have a total extension of more than 9 billion light years on a side. The overlaid panels zoom in by factors of 4 in each case, enlarging the regions indicated by the white squares. Image credits: The Millennium Simulation Project, Max Planck Institute for Astrophysics.

On the largest scales shown in Fig. 2.2, the universe appears nearly homogeneous. The series of enlargements overlaid show a complex web of dark matter up to the ‘smallest’ scales of order ~ 100 Mpc (about 300 million light years). The largest of these halos are rich clusters of galaxies, containing more than one thousand galaxies which are still resolved as halo substructure in the simulation.

2.2 Different types of dark matter

Some of the dark matter in the Universe could be – and probably is – Jupiter sized planets, brown dwarfs, or other such objects that we know exist but that simply does not shine sufficiently for us to be able to observe them. These types of objects have been nicknamed MACHOs (MASSive Compact Halo Objects). However, the nucleosynthesis theory of light element production in the Big Bang [18] places limits on how much baryonic matter (i.e. specifically protons and neutrons and in general atoms of any sort) that can exist in the universe. There is simply not enough baryons to make up for the missing matter content. A large portion of the dark matter must be so-called non-baryonic.

Non-baryonic matter is any sort of matter that is not primarily composed of

baryons. This might include ordinary matter such as neutrinos or free electrons. However, it may also include exotic species of supersymmetric particles. The supersymmetric extension of the standard model of particle physics contains several hypothetical candidates for dark matter particles, sometimes referred to as WIMPS (Weakly Interacting Massive Particles). These particles must interact only through the weak nuclear force and gravity, or at least with interaction cross-sections no higher than the weak scale. They must also have a large mass compared to standard particles. In standard theory, the particles that have little interaction with normal matter, such as neutrinos, are all very light and would therefore be moving at ultrarelativistic speeds. This hot dark matter can not explain observations of galaxy-sized clustering. So far, there has been no confirmed detection of a WIMP.

Unlike normal, everyday matter, non-baryonic dark matter particles are assumed to be collisionless, i.e. they are very hard to detect because they pass through practically everything. Observing dark matter particles is extremely difficult due to the fact that they are so weakly interacting. The collisionless nature of the dark matter has recently been confirmed from a study of 16 galaxy clusters by Høst et al. [19]. At the Large Hadron Collider at CERN, the intensive hunt for supersymmetric particles will soon be on its way.

As dark matter particles have not yet been observed, the existence of dark matter remains theoretical. Alternative gravity theories, such as Modified Newtonian Dynamics (MOND), claim to explain the observed gravitational fields without resorting to any mysterious dark matter. In these alternative theories, gravity behaves differently on cosmological distance scales than on smaller distances. If Einsteins theory of gravity is incomplete, then there might be no missing matter, only ordinary everyday matter that gives rise to gravitational fields that look differently than we expect them to.

However, the most direct evidence to date for the existence of dark matter poses severe problems for alternative gravity theories. This evidence comes from the Bullet Cluster [20], in actuality two colliding galaxy clusters. The stars, gas and dark matter components in the clusters will behave differently during collision, allowing for them to be studied separately. The stars in the cluster galaxies were not greatly affected by the collision, and most of them passed right through, gravitationally slowed but not otherwise altered. The hot gas of the two colliding components, seen in X-rays, represents most of the mass of the baryonic matter in the cluster pair. The gases interact electromagnetically, causing the gases of both clusters to slow much more than the stars. The third component, the dark matter, was detected indirectly by the gravitational lensing of background objects. In theories without dark matter, the lensing effect would be expected to be strongest around the X-ray gas (the major component of baryonic matter). However, the lensing proved to be strongest elsewhere, supporting the idea that most of the mass in the cluster pair is in the form of collisionless, non-baryonic dark matter. At a statistical significance of 8σ , it was found that the spatial offset of the center of the total mass from the center of the baryonic mass peaks cannot be explained with an alteration of the gravitational force law.

Chapter 3

Probing the unseen with gravitational lensing

There are two kinds of light – the glow that illuminates, and the glare that obscures.
James Thurber

Gravitational lensing is the bending of light rays from a distant source due to the gravitational field of a massive object (e.g. a galaxy or a galaxy cluster) that lies between us and the source. We can therefore never see the source itself, as it would have looked without the lens effect. Instead, we see what we call *images* of the source. These images can be shifted in position, multiplied, magnified, de-magnified and also deformed in appearance due to the presence of the gravitational field of the intervening material between us and the source. Analogues of these cosmological effects can be observed in daily life. Looking through a wine glass at a distant street light, looking in a fun-house mirror, mirages of atmospheric lensing due to a heated ground all illustrate the same concepts¹ applying to gravitational lensing in the Universe. Fig. 3.1 illustrates the concept of lensing in the laboratory, while Fig. 3.2 shows the distortions caused by the galaxy cluster Abell2218.

Gravitational lensing is a unique tool in the exploration of the Universe. It is a naturally occurring effect that can be used to detect mass independent of its nature, i.e. whether it is shining or not. The degree to which an object is lensed by intervening matter simply depends on the gravitational field of the mass concentration. In other words, the light paths respond equally to ordinary (luminous) matter as to the mysterious dark matter discussed in Chapter 2. This is important because there seems to be much more dark than luminous matter. Therefore, if we can measure the strength and distribution of the distortions caused by lensing, we might be able to infer something about the actual mass distribution in the Universe.

Other methods that probe the distribution of matter have to rely on luminous markers of various kinds, e.g. X-ray radiation from the hot intracluster gas in a galaxy cluster. The distribution of the gas traces the overall cluster gravitational field, and therefore allows calculation of the total mass distribution in the clus-

¹For some fun examples, see
<http://www.astro.ulg.ac.be/themes/extragal/gravlens/bibdat/engl/DE/didac.html>

ter. However, this last step necessarily involves some sort of mass-to-luminosity relation. Using gravitational lensing, there is no need to assume a relationship between the visible and the invisible matter in order to trace the dominating matter component. In addition, lensing can be used on scales where luminous markers do not even exist.

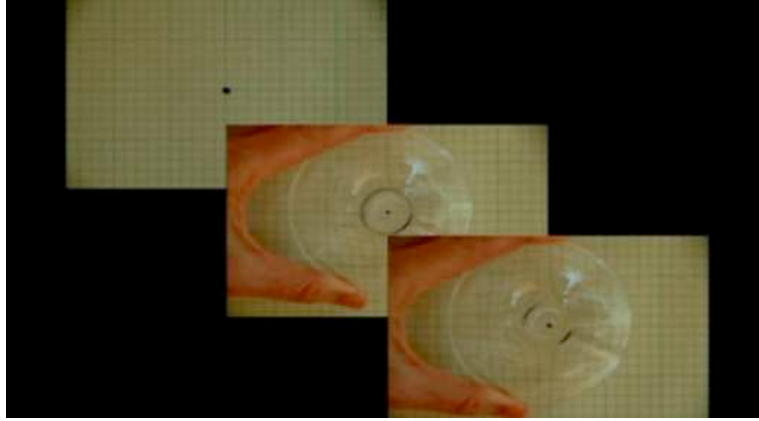


Figure 3.1: Illustrating what we can see through a gravitational lens: The gravitational lens can be illustrated by the cut-off bottom of a wine glass. The glass acts as a lens, analogous to a massive object in the Universe. We see through the lens (the piece of glass) towards the galaxy (the black dot on the graph paper) in the background. Left panel: What we would have observed without the lens (not possible to reconstruct in astronomical situations!). Middle panel: the lens is introduced, perfect alignment between lens and source. We see a ring (Einstein ring) around the original position of the lens, as well as the source (dot) in the middle. Right panel: Lens and source are displaced a little, producing two arcs on either side of the source. In astronomical observations the source in the middle would not be visible due to the lens obscuring it. Image Credits: Talk on-line by Patricia Burchat: *The search for dark energy and dark matter*, <http://www.ted.com>

Measurements of statistical properties of the lensing distortion can be related to properties of the dark matter distribution at different times in the history of the Universe, i.e. at different redshifts. The evolution of the dark matter (Chapter 2) distribution can yield information about dark energy (Chapter 4). It is often concluded that gravitational lensing holds great promise for understanding the nature of both dark matter and dark energy, see the report from the Dark Energy Task Force [21] and the report by the ESA-ESO Working Group on Fundamental Cosmology [22].

In this chapter I will first give a short introduction to some different types and applications of lensing phenomena (Sec. 3.1), and the basic equations underlying gravitational lensing theory (Sec 3.2). In Sec. 3.3 I focus more specifically on lensing by galaxy clusters, which is the topic of paper I. In Sec. 3.4 I describe how large-scale simulations of the projected matter distribution in the Universe can be used to simulate the lensing signal, which is what we investigated in paper II. For excellent reviews of lensing, see [23–25], and for reviews specifically concerning weak lensing, see [26–32].

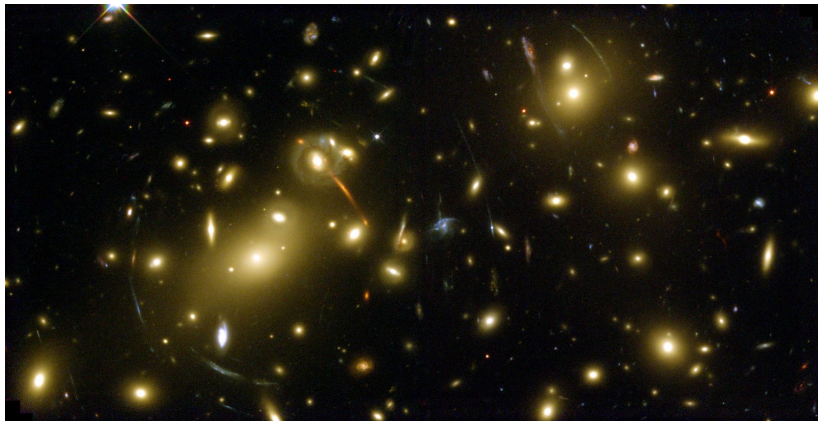


Figure 3.2: Looking at the effects of dark matter: The famous strong lensing caused by the galaxy cluster Abell2218, which is about 2 billion light years distant in the constellation Draco. The golden ‘fuzzy’ galaxies are galaxies in the cluster itself. The arcs and streaks are distorted shapes of galaxies that are actually much further away. Image credits: NASA, A.Fruchter and the ERO Team (STScI).

3.1 Classifications

For a few hundred years, gravitational lensing was a theoretical possibility. Both Newton’s and Einstein’s theory of gravity predict bending of light from nearby stars by the massive Sun, see Fig. 3.3, but the bending angle is different in the two theories. A Newtonian calculation, treating light as particles, predicts a shift in position of 0.87 arcseconds for the stars closest to the Sun. The general relativity calculation, taking into account the curvature of space, predicts a shift twice as large. A solar eclipse in 1919 enabled the first observational confirmation of gravitational lensing as well as a test of Newtonian versus Einsteinian gravity theories. With the Moon blocking out the glaring sunlight, astronomers could note the positions of stars close to the line of sight between the Earth and the Sun, and compare this to the positions of the same stars at other times of the year when they were visible at night. Observations taken during the eclipse in 1919 [33], though of poor quality by today’s standards, were convincing enough at the time to confirm Einstein’s predictions and was a major contribution towards the acceptance of general relativity.

The observations needed to confirm gravitational lensing by the Sun were difficult because the predicted shift in position was so small, less than two arcseconds². Mass concentrations much larger than the Sun will produce gravitational lensing effects that are more spectacular. Galaxy clusters have total masses of $\sim 10^{14} - 10^{15}$ times the mass of the Sun. Such a gigantic mass concentration will drastically alter the curvature of space, gathering and distorting light from incredibly distant light sources, focussing them into beautiful arcs in the sky like those seen in Fig. 3.2. However, observing gravitational lensing on this larger scale has not been possible until more recently.

²The angular size of the Moon is about 1800 arcseconds.

Strong gravitational lensing is the name given to the production of multiple images and large arcs of very distant background galaxies, caused by very massive lenses such as a galaxy cluster. The image of a background galaxy can be greatly magnified or distorted depending on its position relative to the lens. The first doubly-imaged object was found by Walsh et al. in 1979 [34], and since then hundreds of multiple-imaged sources have been found [35], as well as many stunning examples of strong distortions as shown in Fig. 3.2. The arcs get their squashed shape because light rays are bent toward the lens, so extrapolating backward shows that the source appears farther away, see Figs. 3.3 and 3.4. Therefore, light coming from areas that pass closer to the lens, appear to us to be further away from it, hence the arcs appear to bend around the cluster. Arcs or multiple images from strong lensing can provide powerful constraints on the projected mass in the lens that is contained within the arc, typically on scales confined to the central regions of the cluster, see [36].

Weak gravitational lensing is the introduction of a small coherent shape distortion in faint background galaxies due to lensing by foreground objects. The effect of weak lensing is more subtle, there are no multiple images or dramatic distortions as for strong lensing. The weak distortion is typically of the order of only a few percent. In fact, variations in the intrinsic elliptical shapes of the galaxies themselves is generally larger than the weak lensing signal. Because of the extremely low signal-to-noise for each individual galaxy, it is necessary to combine data from thousands of lensed galaxies in order to detect the weak lensing signal. Weak lensing can occur where the lens itself is an individual galaxy (so-called galaxy-galaxy lensing) as well as where the lens is a galaxy cluster. The first tentative detections of weak lensing by the tangential distorted images of cosmologically distant, faint galaxies due to lensing by foreground galaxies was made by Brainerd et al. [37] and confirmed by Fischer et al. [38]. Detection of cluster weak lensing dates from 1990, and was reported by Tyson et al. [39] from the detection of a coherent alignment of the ellipticities of faint blue galaxies behind clusters Abell 1689 and CL 1409+52.

Weak lensing can be used to find constraints on the mass profiles of the lens. Combining strong and weak lensing can significantly improve constraints on the mass density profile [40]. Statistics of the shear field can be used to measure the evolution of structures, measure cosmological parameters and explore models beyond the standard Λ CDM model, see Chapter 4.

Microlensing is the study of peaks and troughs in charted brightness curves of background stars or quasars, caused by individual stars or planetary sized objects, e.g. brown dwarf stars. As the term implies, the multiple images induced by microlensing have a separation of the order of *micro*arcseconds, which is too small for us to resolve with present-day technology. However, microlensing can be detected where it causes uncorrelated brightness variations in multiple macro-images of a source. Typically, light rays that are emitted from a source in different directions at the same time and which travel different routes towards us due to lensing, will arrive here at different times. We can measure this time delay using multiply imaged sources with variable emission, by compiling and comparing light curves as observed from the different images. In 1964, S. Refsdal [41] proposed a geometrical method to calculate the Hubble parameter today, H_0 , based on this time delay and the deformation of wavefronts as light waves move past the

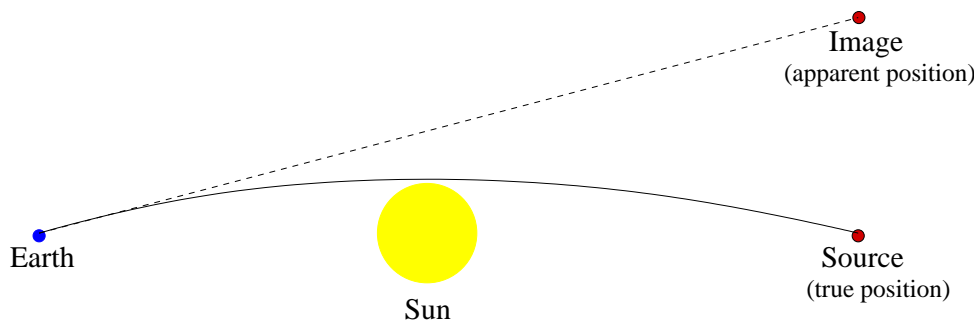


Figure 3.3: Gravitational deflection of a light ray from a distant source (a star). The drawing illustrates the principle involved in gravitational lensing, and is not drawn to scale. The light ray is bent towards the Sun (or another massive object), causing the apparent position of the image of the star to be located further away from the Sun. In reality, the angle of deflection is very small.

deflector towards the observer. If the mass distribution is known, an expression for H_0 can be derived solely in terms of observable quantities, see [24].

In some cases, a small lens, e.g. a planetary sized object, moves into the line connecting a source to us. When this happens, the image of the source is magnified in such a way that a distinct variability can be observed in the brightness curve of the distant source. In recent years, microlensing has been used to find MACHOs in our galaxies, as well as detecting extra-solar planets [42].

Cosmic shear is the weak lensing introduced by the deflections that light rays encounter by passing all of the large-scale structure on its way from the last scattering surface to us. This distortion is at $\sim 0.1 - 1\%$ even more subtle than cluster weak lensing or galaxy-galaxy lensing. In addition, the approximation called the thin-lens approximation, see Fig. 3.4, does not always work in this case because the large-scale structure can be elongated along the line of sight. To first order cosmic shear can measure a combination of the matter density of the Universe in units of the critical density, Ω_m , and the rms mass fluctuation in spheres of radius 8 Mpc also known as the normalisation of the power spectrum, σ_8 .

The first detections of cosmic shear were reported less than ten years ago, in the spring of 2000, when four independent groups published their results [43–46]. The most recent results [47, 48] use millions of galaxies to measure the clumpiness of dark matter to around 5 percent accuracy. Knowledge of the source redshifts is currently the dominating limiting factor for cosmic shear studies. In future surveys, the acquirement of large photometric redshift catalogues can remedy this and allow future studies to divide the survey into several redshift bins. Sources in redshift bins far away, i.e. at high redshift, will encounter (and be lensed by) much more intervening structure than sources in bins closer to us. This technique is called cosmic tomography [49] and makes it possible to map the three dimensional distribution of mass. Since the third dimension involves both distance and cosmic time, the results will be sensitive to the expansion history of the Universe during that time. Many proposed experiments that aim to study the properties of dark matter (Chapter 2) and dark energy (Chapter 4) have

focussed on weak lensing, such as the Dark Energy Survey (DES), Pan-STARRS and the Large Synoptic Survey Telescope (LSST).

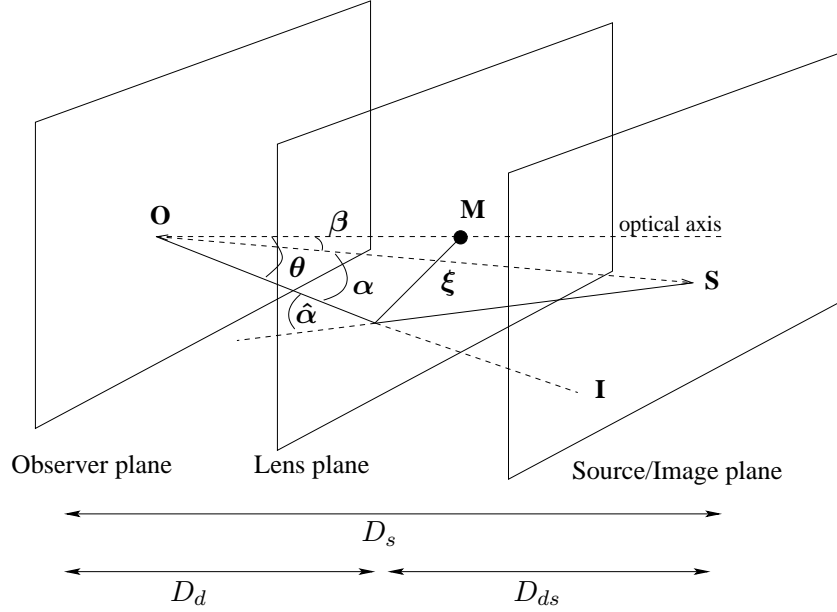


Figure 3.4: Geometry of the lensing situation and illustration of the thin-lens approximation. The source at S sends out a light ray (solid line) towards the observer located at O . The ray passes a massive object at M and is deflected by an angle $\hat{\alpha}$ as shown. The entire deflection is assumed to occur at the point where the light ray is passing through the lens plane. Position angle of the source with respect to the optical axis (along which the lens is located) is β

3.2 Basic lensing theory

Lensing can be described as a mapping of a source to an image of the source. In some cases the lensing is strong enough to produce striking arcs (see Fig. 3.2) or, in the case of perfect observer-lens-source alignment, rings.

Gravitational lensing changes the apparent solid angle of a source, but the surface brightness is conserved. A magnification of source size will lead to an amplification of the source signal. The total flux received from a gravitationally lensed image is therefore changed by a factor equal to the ratio of the solid angles of the image and the source:

$$\text{magnification} = \frac{\text{image area}}{\text{source area}} . \quad (3.1)$$

Fig. 3.4 illustrates the gravitational lensing situation. A distant source S located at β , sends a light ray towards the observer at O . Passing through the lens plane, the ray is deflected by an angle $\hat{\alpha}$ so that, as seen from O , the source appears to be located at I . The position(s) of the images I are the solutions θ of the lens equation:

$$\boldsymbol{\theta} - \boldsymbol{\beta} = \boldsymbol{\alpha}(\boldsymbol{\theta}) = \frac{D_{\text{ds}}}{D_{\text{s}}} \hat{\boldsymbol{\alpha}} . \quad (3.2)$$

D_{ds} , D_{d} and D_{s} are angular diameter distances between, respectively, deflector (lens) and source, observer and deflector and observer and source. In general, because we might have curved spacetimes, we have that: $D_{\text{ds}} \neq D_{\text{s}} - D_{\text{d}}$. The solutions $\boldsymbol{\theta}$ of the lens equation yield the angular positions of the images of the source.

To describe the shift in angle experienced by a light ray during lensing, it is conventional to define the 2×2 symmetric transformation matrix

$$\mathcal{A} = \frac{\partial \boldsymbol{\beta}}{\partial \boldsymbol{\theta}} . \quad (3.3)$$

In general, the magnification is given by the inverse of the determinant of the Jacobian matrix \mathcal{A} . Locations at which $\det \mathcal{A} = 0$ have formally infinite magnification. They are called *critical curves* in the lens plane. The corresponding locations in the source plane are called *caustics*.

Distances between source, lens and observer are so large that most of the deflection of light rays takes place at a very small part of the total extent of the light path. The lens can therefore be considered *thin* compared to the light path. This is called the thin-lens – or thin screen – approximation. The mass distribution of the lens can then be projected along the line of sight and replaced by a mass sheet (the lens plane) orthogonal to the line-of-sight and with surface mass density Σ :

$$\Sigma(\boldsymbol{\xi}) = \int \rho(\boldsymbol{\xi}, z) \, dz , \quad (3.4)$$

where $\boldsymbol{\xi}$ is a $2D$ vector in the lens plane, indicating the distance from the light ray to the centre of mass of the lens, as seen in Fig. 3.4.

Using the thin-lens approximation, we are assuming that all of the deflection occurs in the lens plane. The deflection angle $\hat{\boldsymbol{\alpha}}$ at position $\boldsymbol{\xi}$ is then the sum of the deflections due to all the mass elements in the plane:

$$\hat{\boldsymbol{\alpha}}(\boldsymbol{\xi}) = \frac{4G}{c^2} \int \int \frac{(\boldsymbol{\xi} - \boldsymbol{\xi}') \Sigma(\boldsymbol{\xi}')}{|\boldsymbol{\xi} - \boldsymbol{\xi}'|^2} \, d^2 \xi' . \quad (3.5)$$

The so-called convergence, κ , is a rescaling of the surface mass density with the critical density, so that

$$\kappa(\boldsymbol{\theta}) = \frac{\Sigma(\boldsymbol{\theta})}{\Sigma_{\text{crit}}} . \quad (3.6)$$

We have here defined the critical surface mass-density:

$$\Sigma_{\text{cr}} \stackrel{\text{def}}{=} \frac{c^2}{4\pi G} \frac{D_{\text{s}}}{D_{\text{d}} D_{\text{ds}}} \quad (3.7)$$

A lens which has $\Sigma > \Sigma_{\text{cr}}$ is referred to as being *supercritical*. Usually, multiple imaging occurs only if the lens is supercritical.

For a circular symmetric lens Eq. (3.5) reduces to the scalar angle

$$\hat{\alpha}(\xi) = \frac{4GM(\xi)}{c^2\xi} , \quad (3.8)$$

with $M(\xi)$ given by

$$M(\xi) = 2\pi \int_0^\xi \Sigma(\xi') \xi' d\xi' . \quad (3.9)$$

For the special case of a symmetric lens, we consider a lens with constant surface-mass density. The lens is then a disk with $\Sigma = \Sigma_0$, $M = \pi\xi^2\Sigma_0$. In practice, this works as a normal converging lens, producing one image only. We then have, from Eq. 3.2:

$$\alpha(\theta) = \frac{D_{\text{ds}}}{D_{\text{d}}} \frac{4G\Sigma\pi\xi^2}{c^2\xi} = \frac{D_{\text{d}}D_{\text{ds}}}{D_{\text{s}}c^2} \frac{4\pi G\Sigma}{\theta} \theta = \frac{\Sigma}{\Sigma_{\text{cr}}} \theta = \kappa\theta . \quad (3.10)$$

where we have also substituted $\xi = \theta D_{\text{d}}$, which can be seen from Fig. 3.4.

This solution can be written

$$\theta - \kappa\theta = \beta \Rightarrow \theta = \frac{\beta}{1 - \kappa} . \quad (3.11)$$

Due to rotational symmetry, a source which lies exactly on the optical axis, i.e. $\beta = 0$, is imaged as a ring if the lens is supercritical. This is called the Einstein ring, and its radius is θ_{E} , which can be calculated as follows. From Eq. 3.2 – assuming a symmetric lens with arbitrary mass profile – and from Eq. 3.8:

$$\alpha = \theta - \beta = \frac{D_{\text{ds}}}{D_{\text{s}}} \hat{\alpha} = \frac{D_{\text{ds}}}{D_{\text{s}}D_{\text{d}}} \frac{4GM(\theta)}{c^2\theta} . \quad (3.12)$$

The Einstein radius is the solution of this equation by solving for image position θ and setting $\beta = 0$, i.e. assuming that the source lies on the optical axis, see Fig. 3.4. We find that

$$\theta_{\text{E}} = \sqrt{\frac{4GM(< D_{\text{d}}\theta_{\text{E}})D_{\text{ds}}}{c^2D_{\text{d}}D_{\text{s}}}} . \quad (3.13)$$

The Einstein radius provides a natural angular scale to describe the lensing geometry. For multiple imaging, the typical angular separation of images is of order $2\theta_{\text{E}}$. In addition, sources which are closer than about θ_{E} to the optical axis experience strong lensing in the sense that they are significantly magnified, whereas sources which are located well outside the Einstein ring are magnified very little. For $\beta = 0$ we have that $\alpha = \theta \Rightarrow \Sigma = \Sigma_{\text{cr}}$. So, the mean surface mass-density inside the Einstein ring is the critical density Σ_{cr} , as defined in Eq. 3.7.

Convergence alone causes a magnification of the source, while the presence of the so-called shear causes the image to be stretched. The shear is a two-component quantity that can be written as a complex number:

$$\gamma = |\gamma|e^{2i\phi} . \quad (3.14)$$

The amplitude of the shear, $|\gamma|$, describes the degree of distortion and the phase ϕ yields the direction of the distortion. The factor 2 in the phase is due to the fact that the ellipse transforms back onto itself for a rotation of 180 degrees.

Introducing ψ as the scaled, projected Newtonian potential of the lens:

$$\psi(\boldsymbol{\theta}) = \frac{D_{\text{ds}}}{D_{\text{d}}D_{\text{s}}} \frac{2}{c^2} \int \Phi(D_{\text{d}}\boldsymbol{\theta}, z) \, dz , \quad (3.15)$$

where the Newtonian potential Φ has been integrated along the line of sight z and scaled by the ratio of distances.

Writing

$$\Psi_{,ij} \stackrel{\text{def}}{=} \frac{\partial^2 \Psi}{\partial \theta_i \partial \theta_j} , \quad (3.16)$$

the shear components can be expressed as linear combinations of $\Psi_{,ij}$:

$$\gamma_1 = \frac{1}{2}(\psi_{,11} - \psi_{,22}) \quad \gamma_2 = \psi_{,12} = \psi_{,21} . \quad (3.17)$$

Using the lens equation, Eq. 3.2, we can write the Jacobian matrix \mathcal{A} from Eq. 3.3 as

$$\mathcal{A}_{ij} = \delta_{ij} - \frac{\partial \alpha_i(\boldsymbol{\theta})}{\partial \theta_j} = \delta_{ij} - \psi_{,ij} , \quad (3.18)$$

where δ_{ij} is the Kronecker delta so that $\delta_{ij} = 1$ if $i = j$ and $\delta_{ij} = 0$ if $i \neq j$. The last part of Eq. 3.18 shows that the matrix of second derivatives of the scaled potential ψ describes the deviation of the lens mapping from the identity mapping. Using the definition of the shear components and

$$\nabla_{\boldsymbol{\theta}}^2 \psi = 2\kappa \Rightarrow \kappa = \frac{1}{2} \nabla \cdot (\nabla \psi) = \frac{1}{2}(\psi_{,11} + \psi_{,22}) , \quad (3.19)$$

we can further write the matrix as

$$\mathcal{A} = \begin{pmatrix} 1 - \gamma_1 - \kappa & -\gamma_2 \\ -\gamma_2 & 1 - \kappa + \gamma_1 \end{pmatrix} , \quad (3.20)$$

which is a common way of writing it. We see how the lens mapping depends on both the convergence and the shear. In the absence of shear, a circular source will be mapped onto a circle with modified radius, depending on κ . In other words, the presence of convergence causes a magnification (the source is mapped onto an image with the same shape but larger size), the shape-independent increase in size of the galaxy image. Shear introduces anisotropy into the lens mapping and causes an axis ratio different from unity: The circular source will be deformed into an ellipse. The orientation of the resulting ellipse depends on the phase of the shear.

For weak lensing, the diagonal of the Jacobian matrix in Eq. 3.20 will be approximately 1, implying weak distortions and small magnifications that cannot be identified in individual sources but only in a statistical sense.

3.3 Weak lensing by gravitational clusters (paper I)

Weak gravitational lensing can be observed either from galaxy-galaxy lensing, lensing by galaxy clusters or as cosmic shear. In this thesis the focus is on lensing by clusters, but the techniques of measuring the shear of the distorted ellipticities of lensed (background) galaxies are similar whatever the object acting as lens.

Most galaxies in the Universe are gravitationally bound to a number of other galaxies, forming a hierarchy of clustered structures, with the smallest such associations being termed groups, with masses around $10^{13} M_{\text{sun}}$. Galaxy clusters are the largest gravitationally bound structures in the Universe and high-mass clusters can be up to $10^{15} M_{\text{sun}}$. Clusters are often centered around a specific galaxy that is brighter and larger than the rest, the so-called brightest cluster galaxy (BCG). Typical cluster galaxies are red (i.e. old) ellipticals with little star-formation activity. Clusters contain stars, gas and dark matter in the approximate mass ratio 1:10:100, see Chapter 2. The visible cluster, consisting of galaxies and hot gas, is embedded in a huge, invisible dark matter halo.

Dark matter halo profiles are often parametrized by the Navarro-Frenk-White (NFW) [50] profile, which can be written as:

$$\rho(r) = \frac{\rho_s}{\left(\frac{r}{r_s}\right)\left(1 + \frac{r}{r_s}\right)^2}, \quad (3.21)$$

where

$$\rho_s = \delta_c \rho_{\text{crit},z} \quad (3.22)$$

$$\delta_c = \frac{200}{3} \frac{c^3}{\ln(1+c) - \frac{c}{1+c}} \quad (3.23)$$

$$(3.24)$$

and

$$r_s = \frac{R_{200}}{c}. \quad (3.25)$$

$\rho_{\text{crit},z}$ is the critical density of the Universe at the redshift of the cluster, and c is called the concentration parameter and is a measure of the density of the halo in the inner regions. According to simulations $c \sim 5$ for clusters, but generally depends on halo mass [51]. An NFW profile decreases as r^{-1} near the centre, as r^{-2} at intermediate radii characterized by the scale radius r_s , and as r^{-3} further out. The transition region can be specified by the concentration parameter. R_{200} is the radius within which the density is 200 times that of the critical (or mean) density at the redshift of the cluster.

Galaxy clusters in general cause weak lensing of galaxies that are further away than the cluster. While strong lensing is a rare phenomenon, weak lensing is much more common. It happens in principle everywhere we look, it is only a question of how accurate we can measure.

The shapes of dark matter halos can give important insight into the nature of dark matter. Studies find that cluster ellipticities are interesting because of

their implications for differentiating between cosmological models [52, 53], their dependence on cosmological parameters [54–56] and their effects on estimates of cluster density profiles [57]. In general, cosmological N -body simulations predict that gravitation causes matter on cluster scales to collapse into aspherical shapes [58], in particular triaxial prolate ellipsoids [59, 60].

Carter & Metcalfe [61] showed in 1980 that the aspherical shape of a cluster as measured by the positions of cluster galaxies, was connected to the velocity anisotropy of the cluster member galaxies’ orbits. Later observations of both the cluster galaxy distribution [62] and X-ray measurements of the intra-cluster gas [53] indicates an elliptical shape, as seen projected on the sky.

The ellipticity of the dark matter distribution in galaxy sized halos using gravitational lensing has been studied observationally using data from the Red-Sequence Survey (RCS), the Sloan Digital Sky Survey (SDSS) and the Canada-France-Hawaii Telescope Legacy Survey (CFHTLS) [63–65]. This measurement has proven to be extremely difficult. However, as Mandelbaum et al. [64] also commented, the stronger signal in clusters of galaxies means that there is more chance of making a detection of ellipticity in this higher mass data set.

In paper I we investigate the shapes of galaxy cluster dark matter halos, as well as the shape of the luminous matter as traced by the distribution of galaxies in the cluster. We have detected, for the first time, an ellipticity in the dark matter component of galaxy clusters.

We use a cluster catalogue compiled from the Sloan Digital Sky Survey (SDSS) [66]. This is the largest existing cluster catalogue to date, consisting of almost 14 000 clusters. Because the shear induced by a cluster will affect the shear field of its neighbours, we attempt to isolate the clusters by removing close neighbouring clusters. For each cluster, we determine whether there are any other clusters within a radius of $5h^{-1}$ Mpc, and remove them if they are less massive. By retaining the most massive cluster we hope that the shear field will be dominated by the remaining cluster. This process reduces the number of available clusters to 4281 between $0.1 < z < 0.3$.

Since the shear signal from a single cluster is very weak, we need to combine the shear patterns produced by many clusters. We produce one image consisting of a combination of the shear signal from the background galaxies of many clusters. We divide this image up into a grid with square pixels the size of 0.4 arcmin. The final result was found to be reasonably stable when changing the pixel size.

If this stacking was done without heed to the rotation angle of the clusters, it would tend to erase any ellipticity that was there in the first place. We therefore rotate and stack our clusters according to the method which is described by Natarajan & Refregier [67] for galaxy-galaxy lensing. This is the first time that this method has been applied to galaxy clusters.

Through the pattern imprinted on the shear maps by intervening massive cluster halos, we detected a dark matter ellipticity of these halos by ruling out a circular distribution at 99.6% confidence. The axis ratio $f = b/a$, where b is the semi-minor axis of the ellipse and a is the semi-major axis, of the combined dark matter halo was $f_{\text{DM}} = 0.48^{+0.14}_{-0.09}$ from a joint χ^2 -analysis for an NFW model.

Similarly, the distribution of the luminous matter, as traced by the number density of individual cluster members, is also clearly elliptical, with a joint axis ratio $f_{\text{LM}} = 0.60^{+0.004}_{-0.005}$. Thus the ellipticity of the luminous matter is consistent with the ellipticity of the galaxy number density distribution.

In order to interpret our results we need to take into account possible misalignments during stacking, i.e. we do not actually know whether the light and dark matter are aligned with each other. When we rotate clusters according to the distribution of the cluster members before stacking, we assume that the orientation of the light is correlated with the orientation of the mass. A result of f_{DM} consistent with 1 could indicate *either* a circular mass distribution *or* a random alignment between the light used for stacking and the dark matter. In the latter case, the circular result would be caused by the stacking of many clusters with different misalignments between the dark and the light matter.

3.3.1 The glow that illuminates: Ellipticity and shear

Weak lensing by clusters causes the intrinsic ellipticities of the background galaxies to be sheared, i.e. stretched and distorted. The shear caused by lensing can be determined from measuring the (deformed) elliptical images of distant galaxies. We do not have theoretical knowledge of the undistorted galaxy distribution, but a good assumption is that unlensed galaxies are randomly oriented. This is a reasonable assumption if there is no direction singled out in the Universe. In this section I describe how the ellipticity of background galaxies is related to the shear signal that we analysed in paper I.

Consider an isolated galaxy as seen on the sky, with surface brightness $I(x, y)$ centered at the origin. To quantify elongation in the horizontal, vertical or diagonal direction, we can use the quadrupole moments Q_{ij} of this galaxy, defined as:

$$Q_{xx} = \frac{\int I(x, y) x^2 \, dx dy}{\int I(x, y) \, dx dy} \quad (3.26)$$

$$Q_{xy} = \frac{\int I(x, y) xy \, dx dy}{\int I(x, y) \, dx dy} \quad (3.27)$$

$$Q_{yy} = \frac{\int I(x, y) y^2 \, dx dy}{\int I(x, y) \, dx dy} . \quad (3.28)$$

In practice, it is not always straightforward to say exactly where the image of one galaxy stops and the image of a neighbouring galaxy begins. To reduce contamination from neighbouring galaxies, a weight function $W(x, y)$ is often included in Eqs. 3.26 - 3.28. This is also the case in the oldest and most widely used method for cosmic lensing analysis, often referred to as the KSB method [68–70].

We can define the complex ellipticity e of the galaxy in terms of Eqs. 3.26 - 3.28:

$$e = \frac{Q_{xx} - Q_{yy} + 2iQ_{xy}}{Q_{xx} + Q_{yy}} . \quad (3.29)$$

Since $e = e_1 + ie_2$, we see that the ellipticity components e_1 and e_2 can be written

in terms of the quadrupole moments as

$$e_1 = \frac{Q_{xx} - Q_{yy}}{Q_{xx} + Q_{yy}} , \quad (3.30)$$

$$e_2 = \frac{2Q_{xy}}{Q_{xx} + Q_{yy}} . \quad (3.31)$$

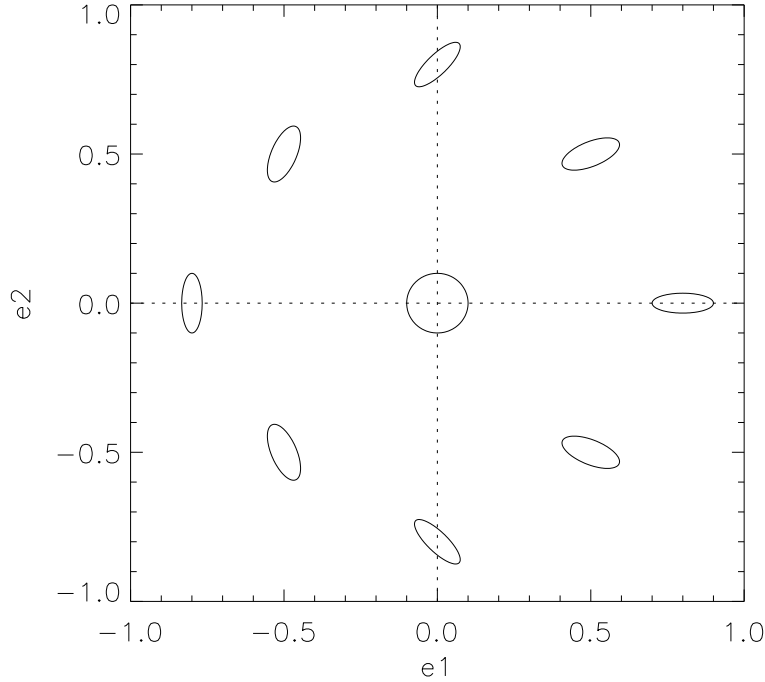


Figure 3.5: Ellipticity parameters e_1 and e_2 calculated for a series of ellipses using the definition of e in Eq. 3.32. Ellipses located further from the centre of this coordinate system are more elongated. Using the definition of Eq. 3.35 would produce a similar plot.

Fig. 3.5 shows how a circular source is transformed as a function of the ellipticity components e_1 and e_2 . A positive (negative) e_1 will stretch an image along the x (y) axis, while a positive (negative) e_2 will stretch it along the line $y = x$ ($y = -x$). In terms of the axis ratio $f = b/a$, where a is the semi-major axis of the ellipse and b is the semi-minor axis so that $f < 1$, the ellipticity can be written:

$$e = \frac{(1 - f)}{(1 + f)} . \quad (3.32)$$

From this it follows that Eqs. 3.30 and 3.31 can be written in terms of a and b as

$$e_1 = \frac{(a - b)}{(a + b)} \cos(2\theta) \quad (3.33)$$

$$e_2 = \frac{(a - b)}{(a + b)} \sin(2\theta) , \quad (3.34)$$

where θ is the angle measured anticlockwise from the positive x axis to the major axis of the ellipse.

Note that there is also a complementary definition of ellipticity often used, from which completely similar deductions can be made:

$$\epsilon = \frac{(1 - f^2)}{(1 + f^2)} . \quad (3.35)$$

This definition is sometimes referred to as the polarization. In paper I we use the axis ratio f to measure the ellipticity. We note here that, for an ellipse aligned along the abscissa (horizontal axis), $0 \leq f \leq 1$, where $f = 1$ represents a circle and a lower f -value gives a stronger ellipticity, $f = 0$ being a horizontal line. f -values greater than 1 produces an ellipse oriented along the ordinate (vertical axis).

In order to measure the distortion induced by lensing, we need to relate the ellipticity of the image to the ellipticity of the source. Due to the fact that surface brightness is invariant in gravitational light deflection, the transformation between the quadrupole moment tensor (Eqs. 3.26 - 3.28) of the image versus that of the source is

$$Q^s = \mathcal{A} Q \mathcal{A}^T , \quad (3.36)$$

e.g. see [71, 72]. The matrix \mathcal{A} is the Jacobi matrix (Eq. 3.3) of the lens mapping. Q is the matrix of quadrupole moments for the galaxy image and Q^s is the corresponding matrix for the source, i.e. representing the intrinsic, unlensed ellipticity.

The transformation between the ellipticity of the source e^s and the ellipticity of the image e is obtained from Eq. 3.36 and can be written, for $|g| \ll 1$, as

$$e = \frac{e^s + g}{1 + g * e^s} \quad (3.37)$$

see [73]. The asterisk $*$ denotes complex conjugation, and g is defined as the reduced shear:

$$g = \frac{\gamma}{1 - \kappa} . \quad (3.38)$$

We see that the condition $|g| \ll 1$ corresponds to the weak lensing regime, where $|\gamma| \ll 1$ and $\kappa \ll 1$.

Unfortunately we do not know have knowledge of the intrinsic ellipticities in the absence of lensing. The strategy is to locally average many galaxy images, assuming that the intrinsic ellipticities on average are *randomly oriented*, in other words that in the absence of lensing there is no preferred orientation for the shapes of galaxies. When averaged over a large population of galaxies, this gives $\langle e_1^s \rangle = \langle e_2^s \rangle = 0$. Taylor expanding Eq. 3.37 to first order in g for the two components e_i shows that e_i is roughly a noisy estimate of g_i , as $\sqrt{\langle e_i^{s2} \rangle}$ is an order of magnitude larger than the typical value of g_i . Applying the symmetries for a large population, we find that

$$\langle e \rangle \approx g . \quad (3.39)$$

Using the ellipticity definition of Eq. 3.35 and a similar transformation to the above, we get

$$\epsilon = \frac{\epsilon^2 + 2g + g^2\epsilon^*}{1 + |g|^2 + \mathcal{R}(g\epsilon^*)} \quad (3.40)$$

where \mathcal{R} denotes that the real part should be taken. Averaging over a population for which $\langle\epsilon_1^s\rangle = \langle\epsilon_2^s\rangle = 0$, $\langle\epsilon_1^s\rangle = \langle\epsilon_2^s\rangle$ and $\langle\epsilon_1^s\epsilon_2^s\rangle = 0$, we arrive at the relation

$$\langle\epsilon\rangle \approx \frac{g}{2(1 - \sigma_\epsilon^2)} , \quad (3.41)$$

where σ_ϵ^2 is the variance of the unlensed ellipticities ϵ . In terms of the two components of the ellipticity, $\sigma_{\epsilon_i}^2 = \langle\epsilon_i^2\rangle$. To sum up, then, the average ellipticity of many galaxies can be used to estimate the shear at the position of that galaxy.

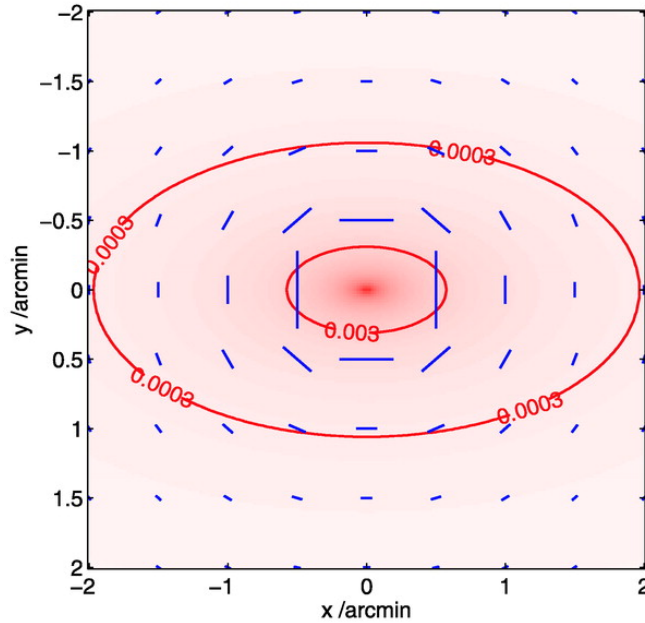


Figure 3.6: Fig.1 from Bridle & Abdalla [74]. Shading and contours show the convergence κ constructed for an elliptical NFW mass distribution ($e = 0.3$, $M_{200} = 1.2 \times 10^{12} h^{-1} M_{\text{sun}}$) at a redshift of $z_l = 0.3$, with sources at redshift $z_s = 0.8$. Shear sticks (lines) show the resulting shear map, where the length of the stick represents the shear strength and the direction of the shear is given by the angle of the stick with respect to the x -axis. For an elliptical lens aligned along the x -axis, the mass density falls more steeply in the y than in the x direction. The result of this is that the sticks on the x -axis are larger than sticks on the y -axis for the same angular distance from the lens center.

When studying weak lensing around galaxy clusters the shear signal is referred to as tangential shear since the distortion effect of a cluster is to introduce an alignment of background galaxy images tangentially to the line from the cluster centre to the galaxy.

From the mathematical definition of the shear in Eq. 3.14, we can define the tangential (γ_T) and cross (γ_\times) components of the shear of the background galaxies

as

$$\gamma_T = \gamma \cos(2\phi) \quad (3.42)$$

$$\gamma_\times = \gamma \sin(2\phi) , \quad (3.43)$$

where ϕ is the angle between the galaxy major axis and a tangent through the centre of the shear galaxy, with respect to the cluster centre. The cross component γ_\times is not expected to occur in nature, but can be a useful test for systematic errors.

The convergence and shear map for an elliptical NFW lens of ellipticity $e = 0.3$ aligned along the x -axis is shown in Fig. 3.6, a reproduction of fig.1 in Bridle & Abdalla [74]. The convergence map (shading and contours) is the projected mass density in units of the critical lens density. The shear field is shown by the overlaid shear sticks (red lines), where the length of the stick gives the amplitude of the shear and the direction of the stick gives the direction of the shear field at that point. We see that the shear at 45 degrees around from the major axis is approximately tangential to the centre of the lens. For a singular isothermal ellipsoid (SIE) model, the shear is exactly tangential.

3.3.2 The glare that obscures: Systematic errors

Weak lensing measurements are subject to a number of potential sources of systematic error, both from the lensing shape measurements and from interpretations of the lensing signal. In this section I will briefly touch upon some of the practical obstacles encountered in lensing analysis, and refer to [25, 72] for a more detailed descriptions of these issues.

The relationship between ellipticity and shear outlined in Sec. 3.3.1 would be adequate for calculating the shear in the absence of disturbances introduced by the atmosphere, pixelisation from the detector CCD chip and noise. One major observational problem that we have already mentioned in Sec. 3.3.1, is that the intrinsic shape of galaxies is not round, and different galaxies have different ellipticities. The observed ellipticity of the image of a galaxy is therefore a combination of intrinsic ellipticity and induced shear that it is not straightforward to separate. In addition, seeing by atmospheric turbulence as well as effects from the camera optics will tend to blur the images, making them appear more circular.

The blurring effects of the atmosphere can be described by a convolution. One tries to correct for the distorting effects by using the point spread function (PSF), which gives information on how a star is broadened by the convolution. Since the PSF represents the disturbance encountered by a point source (a star), it gives information on the convolution kernel itself and can therefore be used to *deconvolve* the extended source (galaxy). On large cameras, the PSF can vary substantially across the image introducing further complications for PSF reconstruction [75]. Corrections for anisotropic PSFs is one of the major sources of systematic errors challenging weak lensing measurements.

The perhaps least well characterized source of systematic error for weak lensing measurements [31] is called intrinsic alignments. There are reasons to believe that unlensed galaxy ellipticities are *not* randomly oriented, as assumed in Sec 3.3.1.

Galaxies at approximately the same redshift can align with other galaxies in response to a gravitational field, thus adding to the shear signal, so-called intrinsic-intrinsic alignments [76, 77]. This source of systematics can be greatly reduced with photometric redshift information, separating galaxies in the z direction so the tidal effects will be weak. On the other hand, the shapes of galaxies at different redshifts may be correlated with their surrounding density field. This same density field contributes to the lensing distortion of more distant galaxies [64, 78], leading to a suppression of the measured shear signal. This second type of correlation, often called gravitational-intrinsic alignments, affects galaxies at different redshifts and is therefore more difficult to correct for. However, it is important to overcome systematics introduced by both types of intrinsic alignments as it can bias cosmic shear results [79].

As regards cluster lensing, which is the topic of papers I and II, possibly the biggest potential systematic error is intrinsic alignment of cluster members pointing at the cluster centre [80–84]. A thorough assessment of the intrinsic alignment effect went beyond the scope of the papers, but does represent a problem because we did not make a significant attempt to remove cluster members from our analysis. To first order intrinsic alignments would make our observed shear maps less elliptical since the contamination by cluster members is greatest along the cluster major axis, and thus the strong gravitational shears expected along this axis will be partially cancelled out by the cluster members since they tend to point at the cluster centre. However, a full assessment of this effect would also have to take into account the variation in intrinsic alignment with respect to the cluster major axis, which appears to be more complicated [81] and possibly weakens the degree of cancellation preferentially along the cluster major axis.

3.4 Predictions of weak lensing from N -body simulations (paper II)

In paper II we apply the method for measuring cluster dark matter ellipticity from paper I to output from a large-scale N -body simulation. In general, we find excellent agreement with the observational results from paper I.

Some earlier numerical results provide a two-dimensional projected ellipticity [85, 86], which is useful for direct comparison with observations using gravitational lensing. However, the best-fit ellipse in previous work is conventionally found by taking moments of particle positions about the center of mass. We have simulated the expected ellipticity that would be observed using gravitational lensing, instead of isolating particles cut off at some circular radius (i.e. the virial radius or R_{200}) in the simulation box. As lensing measures the projected mass along the line of sight, ellipticities measured using gravitational lensing are potentially increased by the inclusion of physically close neighbors and filaments. However they may also be decreased by the contribution from coincidental overlaps by physically separated objects projected along the line of sight. By properly simulating gravitational lensing measurements, we can compare results from paper II directly to results from paper I.

We started with the output of a large ($N = 1024^3$ particles) cosmological dark

matter simulation of a cube of size $L = 320h^{-1}\text{Mpc}$. The cosmology was chosen to be consistent with that measured from the 3rd-year WMAP data combined with large-scale structure observations, see [87], namely a spatially flat ΛCDM model. Convergence maps were produced by projecting down a lightcone covering one octant of the sky and summing up the contribution of all the clusters lying along the line of sight of each map pixel. The projection was normalized by a factor depending on the redshift distribution $n(z_s)$ of background (lensed) galaxies, as measured by the Sloan Digital Sky Survey (SDSS).

We find that surrounding large-scale structure causes a large scatter between ellipticities as measured by lensing and ellipticities calculated directly from particles in the cluster simulation. When repeating the method of paper I of stacking many clusters to obtain the shear signal for an average cluster, the large-scale structure tends to cancel out. The resulting axis ratios agree well with those calculated using the conventional method.

Chapter 4

Invisible Universe II: Dark Energy

Until the end of the previous century, it was generally assumed that the Universe would expand slower and slower as gravity pulled on all existing matter. Depending upon how much matter there was in the Universe, it would either expand forever, or reach a point where it would begin to contract again. Completely contrary to expectations, in the late 1990's results were published indicating the exact opposite. The expansion of the Universe appears to be accelerating. This revolutionary discovery prompted a new era in cosmology. In order for the Universe to be expanding at an ever increasing rate, there must be something that is causing the acceleration. Currently, gravity is the only known force which can act at cosmological distances, but gravity is an attractive force. What then, is 'pushing' the Universe to expand faster and faster? Cosmologists call it dark energy and it turns out to be the major component of the Universe today.

4.1 Evidence for dark energy

Current estimates from NASA's Wilkinson Microwave Anisotropy Probe (WMAP) [13] show that the Universe consists of $\sim 4\%$ baryons, 21% cold dark matter and an astonishing 75% dark energy. WMAP measures the amplitude of temperature fluctuations in the cosmic microwave background radiation as a function of angular size on the sky, and from this information cosmological parameters can be inferred.

Early indications of the acceleration of the Universe actually dates back to a result from measuring the redshifts and magnitudes of galaxies by J.-E. Solheim as far back as 1966 [88]. He used cluster galaxies to measure the magnitude-redshift relation and found that the best-fit model describing the data included a non-zero cosmological constant and a negative deceleration parameter. During the 1980's, more tantalizing hints were reported, but the evidence was highly uncertain. Cosmic acceleration was not taken seriously by the cosmological community until results of luminosity distance versus redshift measurements of the more reliable supernova type Ia were published by two independent teams in 1998 [5, 6].

Supernovae of type Ia (SNIa) are the explosive deaths of white dwarf stars. These explosions are relatively uniform in their luminosities, making them ideal standard candles for measuring luminosity distances. To date, supernovae remain the most direct and well established method for constraining dark energy [21]. Current surveys include the SuperNova Legacy Survey (SNLS) [89], which expects to discover ~ 700 high-redshift supernovae, and ESSENCE Supernova Survey [90], which aims to measure the dark energy equation of state parameter to ± 0.1 by following ~ 200 type Ia supernovae over a period of five years. Future surveys such as The SuperNova Acceleration Probe (SNAP) will study more supernovae at higher redshifts as well as bringing more precise information on sources of systematic uncertainties such as a possible redshift-dependent luminosity evolution of the supernovae. SNAP [91] is now being proposed as part of the Joint Dark Energy Mission (JDEM).

Galaxy cluster and weak lensing surveys are also sensitive to dark energy. Since the number density of clusters as a function of mass and redshift is sensitive to the underlying cosmological model, cluster counts can be used to constrain cosmological parameters. For example, the formation epoch of galaxy clusters depends on the matter density parameter Ω_m of the Universe [92]. One way of detecting clusters is to measure peaks in the shear fields caused by weak lensing. Although the shear peaks-method is subjected to projection effects because lensing measures mass along the line of sight, new studies show that the projected peak and the 3-dimensional mass function scale with cosmology in an astonishingly close way [93].

The acceleration of the Universe will try to counteract the formation of structure. Therefore, in a universe with a strong dark energy term, the clusters we observe today must have formed earlier, and hence are expected to be more relaxed and contain less substructure, than if the Universe was matter-dominated. Like cluster counting, gravitational weak lensing observations probe the dark energy via both the expansion history of the Universe and the growth history of density fluctuations. There is a multitude of weak lensing statistics that can be performed (power spectra, cross-spectra, bispectra, etc.) which allows for the correction of many potential systematic errors [21].

In order to obtain precise weak lensing results for cosmological purposes, it will be necessary to measure the distortion of the shapes of galaxies to extremely high accuracy for millions of galaxies [72]. Future surveys will be bringing in the potential for a substantial increase in the accuracy of dark energy measurements *if* the distortion can be measured better than an accuracy of 0.0003. 2008 saw the launching of the GRavitational lEnsing Accuracy Testing 2008 (GREAT08) challenge, aimed at solving this practical problem.

Baryon Acoustic Oscillations (BAO) is a series of peaks and troughs predicted in the matter power spectrum, or equivalently a characteristic scale in the galaxy distribution. In the very early Universe the environment was so hot and dense that baryons and photons were coupled in a plasma. Fluctuations in this plasma were due to the competing forces of gravity and radiation pressure. In early 2005 a peak in the galaxy correlation function at $100h^{-1}\text{Mpc}$ was reported by the SDSS team [94], which was an excellent match to the predicted imprint of acoustic oscillations on low-redshift clustering of matter. The scale of the

acoustic oscillations provide a standard ruler with great potential to be used for constraining dark energy from future galaxy surveys [21, 95] through its effect on the angular distance versus redshift-relation.

The integrated Sachs-Wolfe (ISW) effect is caused by gravitational red- or blueshifts affecting CMB photons propagating from the last scattering surface and encountering gravitational potentials (i.e. large matter concentrations). With dark energy dominating the Universe today, the gravitational potential will be time dependent. In other words, the energy gained by photons falling into a potential well does not cancel out the energy loss as the photons climb out of the well. This large-scale effect can be measured by cross-correlating large-scale structure observations with CMB anisotropies caused by the ISW-effect [96, 97].

By modifying Einstein’s field equations it might be possible to explain current and future observations without introducing an explicit ‘dark energy’. As an example, gravity may be modified on large scales due to the presence of a large extra dimension. A proper treatment of this subject is beyond the scope of this thesis.

4.2 Cosmological models with dark energy

One of the simplest ways to incorporate the acceleration of the Universe into theoretical models, is to revive the cosmological constant Λ term, (see Chapter 1). Ironically, Λ was originally introduced by Einstein as a way of *preventing* his model of the Universe from evolving. In its simplest form, general relativity predicted that the Universe must either expand or contract. As seemed natural at the time, Einstein thought the universe was static, so he added the Λ term to his equations to stop the expansion. Alexander Friedmann (1888-1925) realized that this was an unstable fix, like balancing a pencil on its point. He proposed an expanding universe model. When in 1929 Hubble’s study of nearby galaxies showed evidence that the universe was indeed expanding, Einstein saw no further use of the cosmological constant and rejected it. Years later, he famously commented to George Gamow that he viewed the introduction of the cosmological constant term as “the greatest blunder of my life” [98]. Modern field theory, however, associates the cosmological constant with the energy density of the vacuum, and on these grounds it has been revived as a driving force for the acceleration of the Universe.

A cosmological constant is not the only possibility for producing an accelerating expansion, and a large number of models have been proposed. These models are mostly phenomenological in nature, i.e. they lack a basis in the current framework of particle physics and cosmology. The hope is that some of these models for dark energy can be connected to extensions of the Standard Model of particle physics, e.g. supersymmetric models or string theory.

Models where the dark energy is a scalar field rolling slowly down a potential, the so-called quintessence models, have become particularly popular. Quintessence differs from the cosmological constant in that it can vary in space and time. It is possible to find classes of scalar-field models which have the interesting property that the scalar fields approach a common evolutionary track from a wide range of

initial conditions. In these so-called ‘tracker’ models the scalar field density (and its equation of state) remains close to that of the dominant background matter during most of the cosmological evolution. A scalar field with these properties may arise naturally in models with large extra dimensions.

Although it is possible to compare models of dark energy to each other and to observations on a model-by-model basis, it is often useful to classify models using some sort of general parameters. The dark energy equation of state parameter w is often used, where the equation of state is parametrized by $p = w\rho$ (see Chapter 1). A cosmological constant has $w = -1$ while more general models of dark energy will have a time dependent w .

4.3 Investigating the statefinder parameters (paper III)

Several theoretical models describing an accelerated universe have been suggested. They are often tested against the SNIa data using the relationship between luminosity distance and redshift, $d_L(z)$:

$$d_L(z) = (1+z) \int_0^z \frac{dz'}{H(z')} . \quad (4.1)$$

In 2003 a method of classifying dark energy models using geometrical quantities derived from the third derivative of the scale factor was proposed by Sahni and coworkers [99, 100]. The so-called statefinder parameters r and s are defined as

$$r = \frac{\ddot{a}}{aH^3} = \frac{\ddot{H}}{H^3} + 3\frac{\dot{H}}{H^2} + 1 \quad (4.2)$$

$$s = \frac{r-1}{3(q-\frac{1}{2})} , \quad (4.3)$$

where $a = a(t)$ is the scale factor of the expansion of the Universe defined in Chapter 1 and dots represent the derivatives with respect to time. We have that $H = \dot{a}/a$, and q is the deceleration parameter

$$q = -\frac{a\ddot{a}}{\dot{a}^2} = -\frac{\ddot{a}}{aH^2} . \quad (4.4)$$

The introduction of the statefinders is motivated by the fact that they simply reduce to $(r, s) = (1, 0)$ for the Λ CDM model. This makes it easy to detect any deviation from Λ CDM.

In paper III, we investigate the usefulness of the statefinder parameters as theoretical classification of dark energy models. We also consider their use in obtaining constraints on dark energy from present and future SNIa data sets.

In order to extract the statefinders in a model-independent way from the data, one has to parametrize $H(z)$ in an appropriate way. The ansatz of [100] was:

$$H(x) = H_0 \sqrt{\Omega_{m0}x^3 + A_0 + A_1x + A_2x^2} , \quad (4.5)$$

where $x = (1 + z)$. The luminosity distance-redshift relationship is then given by

$$d_L = \frac{1+z}{H_0} \int_1^{1+z} \frac{dx}{\sqrt{\Omega_{m0}x^3 + A_0 + A_1x + A_2x^2}} . \quad (4.6)$$

After fitting some or all (depending on the model) of the parameters Ω_{m0} , A_0 , A_1 and A_2 using both existing and simulated supernovae data, we could then reconstruct the statefinders by substituting Eq. 4.5 into the definitions for r (Eq. 4.2) and s (Eq. 4.3) using the best-fit value of the parameters.

We reconstructed the statefinders from several dark energy models, including Λ CDM with and without curvature, flat quiescence models (i.e. models where w is a constant but can be different from -1), the modified polytropic Cardassian model and the generalized Chaplygin Gas model. For comparison, we also calculate the statefinders directly from Eq. 4.2 and Eq. 4.3 using the expression for $H(z)$ specified by each model.

We conclude that even with SNAP-quality data there may be difficulties in distinguishing between dark energy models solely based on the statefinder parameters. Our findings also indicate that it is non-trivial to extract the statefinders from the data in a model-independent way. While a useful theoretical and visual tool, applying the statefinders to observations is not straightforward.

Bibliography

- [1] http://en.wikipedia.org/wiki/Scientific_Revolution.
- [2] A. A. Penzias and R. W. Wilson. A Measurement of Excess Antenna Temperature at 4080 Mc/s. *ApJ*, 142:419–421, July 1965.
- [3] <http://nobelprize.org/>.
- [4] B. May, P. Moore, and C. Lintott. *Bang, The Complete History of the Universe*. Carlton Books, 2006.
- [5] A. G. Riess et al. Observational Evidence from Supernovae for an Accelerating Universe and a Cosmological Constant. *AJ*, 116:1009–1038, September 1998.
- [6] S. Perlmutter et al. Measurements of Omega and Lambda from 42 High-Redshift Supernovae. *ApJ*, 517:565–586, June 1999.
- [7] <http://map.gsfc.nasa.gov/>.
- [8] G. F. Smoot et al. Structure in the COBE differential microwave radiometer first-year maps. *ApJ*, 396:L1–L5, September 1992.
- [9] D. N. Spergel et al. First-Year Wilkinson Microwave Anisotropy Probe (WMAP) Observations: Determination of Cosmological Parameters. *ApJS*, 148:175–194, September 2003.
- [10] <http://www.sdss.org/>.
- [11] G. Efstathiou et al. Evidence for a non-zero Λ and a low matter density from a combined analysis of the 2dF Galaxy Redshift Survey and cosmic microwave background anisotropies. *MNRAS*, 330:L29–L35, February 2002.
- [12] M. Tegmark et al. Cosmological parameters from SDSS and WMAP. *Phys. Rev. D*, 69(10):103501–+, May 2004.
- [13] E. Komatsu et al. Five-Year Wilkinson Microwave Anisotropy Probe Observations: Cosmological Interpretation. *ApJS*, 180:330–376, February 2009.
- [14] V. C. Rubin and W. K. J. Ford. Rotation of the Andromeda Nebula from a Spectroscopic Survey of Emission Regions. *ApJ*, 159:379–+, February 1970.

- [15] F. Zwicky. Die Rotverschiebung von extragalaktischen Nebeln. *Helvetica Physica Acta*, 6:110–127, 1933.
- [16] <http://www.mpa-garching.mpg.de/galform/virgo/millennium/>.
- [17] V. Springel et al. Simulations of the formation, evolution and clustering of galaxies and quasars. *Nature*, 435:629–636, June 2005.
- [18] R. A. Alpher, H. Bethe, and G. Gamow. The Origin of Chemical Elements. *Physical Review*, 73:803–804, 1948.
- [19] O. Host et al. Measurement of the Dark Matter Velocity Anisotropy in Galaxy Clusters. *ApJ*, 690:358–366, January 2009.
- [20] D. Clowe et al. A Direct Empirical Proof of the Existence of Dark Matter. *ApJ*, 648:L109–L113, September 2006.
- [21] Andreas Albrecht et al. Report of the dark energy task force. 2006.
- [22] J. A. Peacock et al. ESA-ESO Working Group on "Fundamental Cosmology". Technical report, October 2006.
- [23] P. Schneider, J. Ehlers, and E. E. Falco. *Gravitational Lenses*. Gravitational Lenses, XIV, 560 pp. 112 figs.. Springer-Verlag Berlin Heidelberg New York. Also Astronomy and Astrophysics Library, 1992.
- [24] S. Refsdal and J. Surdej. Gravitational lenses. *Reports of Progress in Physics*, 57:117–185, 1994.
- [25] C. S. Kochanek, P. Schneider, and J. Wambsgannss. *Gravitational Lensing: Strong, Weak & Micro*. Springer-Verlag: Berlin, 2006.
- [26] R. D. Blandford and R. Narayan. Cosmological applications of gravitational lensing. *ARA&A*, 30:311–358, 1992.
- [27] Y. Mellier. Probing the Universe with Weak Lensing. *ARA&A*, 37:127–189, 1999.
- [28] A. Refregier. Weak Gravitational Lensing by Large-Scale Structure. *ARA&A*, 41:645–668, 2003.
- [29] D. Munshi, P. Valageas, L. Van Waerbeke, and A. Heavens. Cosmology with Weak Lensing Surveys. *ArXiv Astrophysics e-prints*, December 2006.
- [30] M. Bartelmann and P. Schneider. Weak gravitational lensing. *Phys. Rep.*, 340:291–472, January 2001.
- [31] H. Hoekstra and B. Jain. Weak Gravitational Lensing and Its Cosmological Applications. *Annual Review of Nuclear and Particle Science*, 58:99–123, November 2008.
- [32] http://en.wikipedia.org/wiki/Weak_gravitational_lensing.
- [33] F. Dyson, A. S. Eddington, and C. R. Davidson. A Determination of the Deflection of Light by the Sun's Gravitational Field, from Observations Made at the Total Eclipse of May 29, 1919. *Phil. Trans. Roy. Soc. A.*, 220:291–333.

- [34] D. Walsh, R. F. Carswell, and R. J. Weymann. 0957 + 561 A, B - Twin quasistellar objects or gravitational lens. *Nature*, 279:381–384, May 1979.
- [35] <http://www.cfa.harvard.edu/castles/>.
- [36] B. Fort and Y. Mellier. Arc(let)s in clusters of galaxies. *A&A Rev.*, 5:239–292, 1994.
- [37] T. G. Brainerd, R. D. Blandford, and I. Smail. Weak Gravitational Lensing by Galaxies. *ApJ*, 466:623–+, August 1996.
- [38] P. Fischer et al. Weak Lensing with Sloan Digital Sky Survey Commissioning Data: The Galaxy-Mass Correlation Function to $1 H^{-1}$ Mpc. *AJ*, 120:1198–1208, September 2000.
- [39] J. A. Tyson, R. A. Wenk, and F. Valdes. Detection of systematic gravitational lens galaxy image alignments - Mapping dark matter in galaxy clusters. *ApJ*, 349:L1–L4, January 1990.
- [40] M. Oguri et al. Subaru Weak Lensing Measurements of Four Strong Lensing Clusters: Are Lensing Clusters Over-Concentrated? *ArXiv e-prints*, January 2009.
- [41] S. Refsdal. On the possibility of determining Hubble’s parameter and the masses of galaxies from the gravitational lens effect. *MNRAS*, 128:307–+, 1964.
- [42] Probing lensing anomalies network, <http://planet.iap.fr>.
- [43] D. M. Wittman et al. Detection of weak gravitational lensing distortions of distant galaxies by cosmic dark matter at large scales. *Nature*, 405:143–148, May 2000.
- [44] D. J. Bacon, A. R. Refregier, and R. S. Ellis. Detection of weak gravitational lensing by large-scale structure. *MNRAS*, 318:625–640, October 2000.
- [45] L. Van Waerbeke et al. Detection of correlated galaxy ellipticities from CFHT data: first evidence for gravitational lensing by large-scale structures. *A&A*, 358:30–44, June 2000.
- [46] N. Kaiser, G. Wilson, and G. A. Luppino. Large-Scale Cosmic Shear Measurements. *ArXiv Astrophysics e-prints*, March 2000.
- [47] R. Massey et al. COSMOS: Three-dimensional Weak Lensing and the Growth of Structure. *ApJS*, 172:239–253, September 2007.
- [48] L. Fu et al. Very weak lensing in the CFHTLS wide: cosmology from cosmic shear in the linear regime. *A&A*, 479:9–25, February 2008.
- [49] B. Jain and A. Taylor. Cross-Correlation Tomography: Measuring Dark Energy Evolution with Weak Lensing. *Physical Review Letters*, 91(14):141302–+, October 2003.

- [50] J. F. Navarro, C. S. Frenk, and S. D. M. White. A Universal Density Profile from Hierarchical Clustering. *ApJ*, 490:493–+, December 1997.
- [51] U. Seljak. Analytic model for galaxy and dark matter clustering. *MNRAS*, 318:203–213, October 2000.
- [52] T. Suwa et al. Cluster Morphology as a Test of Different Cosmological Models. *ApJ*, 588:7–17, May 2003.
- [53] R. A. Flores et al. The Shape of Galaxy Cluster Dark Matter Haloes: Systematics of Its Imprint on Cluster Gas, and Comparison to Observations. *ArXiv Astrophysics e-prints*, August 2005.
- [54] S. Ho, N. Bahcall, and P. Bode. Cluster Ellipticities as a Cosmological Probe. *Astrophys. J.*, 647:8–12, August 2006.
- [55] N. Rahman et al. Morphology and Evolution in Galaxy Clusters I: Simulated Clusters in the Adiabatic limit and with Radiative Cooling. *ArXiv Astrophysics e-prints*, May 2004.
- [56] R. J. Splinter, A. L. Melott, A. M. Linn, C. Buck, and J. Tinker. The Ellipticity and Orientation of Clusters of Galaxies in N-Body Experiments. *ApJ*, 479:632–+, April 1997.
- [57] M. Meneghetti et al. The effects of ellipticity and substructure on estimates of cluster density profiles based on lensing and kinematics. *MNRAS*, 381:171–186, October 2007.
- [58] S. F. Kasun and A. E. Evrard. Shapes and Alignments of Galaxy Cluster Halos. *ApJ*, 629:781–790, August 2005.
- [59] J. Dubinski and R. G. Carlberg. The structure of cold dark matter halos. *ApJ*, 378:496–503, September 1991.
- [60] M. S. Warren et al. Dark halos formed via dissipationless collapse. I - Shapes and alignment of angular momentum. *ApJ*, 399:405–425, November 1992.
- [61] D. Carter and N. Metcalfe. The morphology of clusters of galaxies. *MNRAS*, 191:325–337, May 1980.
- [62] V. Strazzullo, M. Paolillo, G. Longo, E. Puddu, S. G. Djorgovski, R. R. De Carvalho, and R. R. Gal. Morphology of low-redshift compact galaxy clusters - I. Shapes and radial profiles. *MNRAS*, 359:191–210, May 2005.
- [63] H. Hoekstra, H. K. C. Yee, and M. D. Gladders. Properties of Galaxy Dark Matter Halos from Weak Lensing. *Astrophys. J.*, 606:67–77, May 2004.
- [64] R. Mandelbaum et al. Ellipticity of dark matter haloes with galaxy-galaxy weak lensing. *MNRAS*, 370:1008–1024, August 2006.
- [65] L. C. Parker et al. The Masses and Shapes of Dark Matter Halos from Galaxy-Galaxy Lensing in the CFHT Legacy Survey. *ApJ*, 669:21–31, November 2007.

- [66] B. P. Koester et al. A MaxBCG Catalog of 13,823 Galaxy Clusters from the Sloan Digital Sky Survey. *ApJ*, 660:239–255, May 2007.
- [67] P. Natarajan and A. Refregier. Two-Dimensional Galaxy-Galaxy Lensing: A Direct Measure of the Flattening and Alignment of Light and Mass in Galaxies. *ApJ*, 538:L113–L116, August 2000.
- [68] N. Kaiser, G. Squires, and T. Broadhurst. A Method for Weak Lensing Observations. *ApJ*, 449:460–+, August 1995.
- [69] G. A. Luppino and N. Kaiser. Detection of Weak Lensing by a Cluster of Galaxies at $Z = 0.83$. *ApJ*, 475:20–+, January 1997.
- [70] H. Hoekstra et al. Weak Lensing Analysis of CL 1358+62 Using Hubble Space Telescope Observations. *ApJ*, 504:636–+, September 1998.
- [71] P. Schneider and C. Seitz. Steps towards nonlinear cluster inversion through gravitational distortions. 1: Basic considerations and circular clusters. *A&A*, 294:411–431, February 1995.
- [72] S. Bridle et al. Handbook for the GREAT08 Challenge: An image analysis competition for cosmological lensing. *ArXiv e-prints*, February 2008.
- [73] C. Seitz and P. Schneider. Steps towards nonlinear cluster inversion through gravitational distortions. III. Including a redshift distribution of the sources. *A&A*, 318:687–699, February 1997.
- [74] S. Bridle and F. B. Abdalla. The Galaxy-Galaxy Lensing Contribution to the Cosmic Shear Two-Point Function. *ApJ*, 655:L1–L4, January 2007.
- [75] M. Jarvis and B. Jain. Principal Component Analysis of PSF Variation in Weak Lensing Surveys. *ArXiv Astrophysics e-prints*, December 2004.
- [76] R. A. C. Croft and C. A. Metzler. Weak-Lensing Surveys and the Intrinsic Correlation of Galaxy Ellipticities. *ApJ*, 545:561–571, December 2000.
- [77] A. Heavens, A. Refregier, and C. Heymans. Intrinsic correlation of galaxy shapes: implications for weak lensing measurements. *MNRAS*, 319:649–656, December 2000.
- [78] C. M. Hirata and U. Seljak. Intrinsic alignment-lensing interference as a contaminant of cosmic shear. *Phys. Rev. D*, 70(6):063526–+, September 2004.
- [79] S. Bridle and L. King. Dark energy constraints from cosmic shear power spectra: impact of intrinsic alignments on photometric redshift requirements. *New Journal of Physics*, 9:444–+, December 2007.
- [80] L. Ciotti and S. N. Dutta. Alignment and Morphology of Elliptical Galaxies - the Influence of the Cluster Tidal Field. *MNRAS*, 270:390–+, September 1994.
- [81] M. Kuhlen, J. Diemand, and P. Madau. The Shapes, Orientation, and Alignment of Galactic Dark Matter Subhalos. *ApJ*, 671:1135–1146, December 2007.

- [82] M. J. Pereira, G. L. Bryan, and S. P. D. Gill. Radial Alignment in Simulated Clusters. *ApJ*, 672:825–833, January 2008.
- [83] A. Knebe et al. On the relation between the radial alignment of dark matter subhaloes and host mass in cosmological simulations. *MNRAS*, pages L40+, March 2008.
- [84] A. Faltenbacher et al. Spatial and Kinematic Alignments between Central and Satellite Halos. *ApJ*, 675:146–155, March 2008.
- [85] P. F. Hopkins, N. A. Bahcall, and P. Bode. Cluster Alignments and Ellipticities in Λ CDM Cosmology. *Astrophys. J.*, 618:1–15, January 2005.
- [86] D. J. Paz et al. Shapes of clusters and groups of galaxies: comparison of model predictions with observations. *MNRAS*, 366:1503–1510, March 2006.
- [87] D. N. Spergel et al. Three-Year Wilkinson Microwave Anisotropy Probe (WMAP) Observations: Implications for Cosmology. *ApJS*, 170:377–408, June 2007.
- [88] J.-E. Solheim. Relativistic world models and redshift-magnitude observations. *MNRAS*, 133:321–+, 1966.
- [89] <http://www.cfht.hawaii.edu/SNLS/>.
- [90] <http://www.ctio.noao.edu/essence/>.
- [91] <http://snap.lbl.gov>.
- [92] D. Richstone, A. Loeb, and E. L. Turner. A lower limit of the cosmic mean density from the ages of clusters of galaxies. *ApJ*, 393:477–483, July 1992.
- [93] L. Marian, R. E. Smith, and G. M. Bernstein. The cosmology dependence of weak lensing cluster counts. *ArXiv e-prints*, November 2008.
- [94] D. J. Eisenstein et al. Detection of the Baryon Acoustic Peak in the Large-Scale Correlation Function of SDSS Luminous Red Galaxies. *ApJ*, 633:560–574, November 2005.
- [95] A. Rassat, A. Amara, L. Amendola, F. J. Castander, T. Kitching, M. Kunz, A. Refregier, Y. Wang, and J. Weller. Deconstructing Baryon Acoustic Oscillations: A Comparison of Methods. *ArXiv e-prints*, October 2008.
- [96] S. Ho et al. Correlation of CMB with large-scale structure. I. Integrated Sachs-Wolfe tomography and cosmological implications. *Phys. Rev. D*, 78(4):043519–+, August 2008.
- [97] A. Rassat, K. Land, O. Lahav, and F. B. Abdalla. Cross-correlation of 2MASS and WMAP 3: implications for the integrated Sachs-Wolfe effect. *MNRAS*, 377:1085–1094, May 2007.
- [98] Donald Goldsmith. *Einstein’s Greatest Blunder? The Cosmological Constant and other fudge factors in the physics of the universe*. Harvard University Press, 1997.

- [99] V. Sahni et al. Statefinder - a new geometrical diagnostic of dark energy. *JETP Lett.*, 77:201–206, 2003.
- [100] U. Alam, V. Sahni, T. Deep Saini, and A. A. Starobinsky. Exploring the expanding Universe and dark energy using the statefinder diagnostic. *MNRAS*, 344:1057–1074, October 2003.

Part II

Papers

Paper I

Evans, A. K. D.; Bridle, S.,
A detection of dark matter halo ellipticity using galaxy cluster lensing in SDSS,
Astrophysical Journal **695** (2009), 1446-1456

A DETECTION OF DARK MATTER HALO ELLIPTICITY USING GALAXY CLUSTER LENSING IN THE SDSS

ANNA KATHINKA DALLAND EVANS¹ AND SARAH BRIDLE²

¹ Institute of Theoretical Astrophysics, University of Oslo, Box 1029, 0315 Oslo, Norway

² Department of Physics and Astronomy, University College London, Gower Street, London, WC1E 6BT, UK

Received 2008 June 18; accepted 2009 January 22; published 2009 April 7

ABSTRACT

We measure the ellipticity of isolated clusters of galaxies in the Sloan Digital Sky Survey (SDSS) using gravitational lensing. We stack the clusters, rotating so that the major axes of the ellipses determined by the positions of cluster member galaxies are aligned. We exclude the signal from the central $0.5 h^{-1}$ Mpc to avoid problems with stacking alignment and cluster member contamination. We fit an elliptical Navarro–Frenk–White (NFW) profile and find a projected, two-dimensional axis ratio for the dark matter of $f = b/a = 0.48^{+0.14}_{-0.09}$ (1σ), and rule out $f = 1$ at 99.6% confidence thus ruling out a spherical halo. We find that the ellipticity of the cluster galaxy distribution is consistent with being equal to the dark matter ellipticity. The results are similar if we change the isolation criterion by 50% in either direction.

Key words: cosmology: observations – dark matter – galaxies: clusters: general – galaxies: halos – large-scale structure of universe

Online-only material: color figures

1. INTRODUCTION

Cosmological simulations can be used to predict many different statistics of the mass distribution in the universe. The most commonly employed statistic is the two-point correlation function, or its Fourier counterpart, the power spectrum. Three-point statistics are much harder to predict and measure, and higher orders are rarely discussed. A more popular statistic is the number of peaks in the mass distribution, as given by the number of clusters of galaxies. The dark matter power spectrum and the number of clusters of galaxies are often cited as among the best ways to constrain the properties of dark energy (e.g., Albrecht et al. 2006).

Uncertainties on cosmological parameters are decreased when two measurements have different parameter degeneracies and are often referred to as “complementary.” In this paper, we consider a statistic which may offer complementary constraints on cosmology: the *shapes* of peaks in the mass distribution, as probed by the ellipticity of galaxy cluster dark matter halos. In addition, this may place important constraints on modifications to the law of gravity since we may compare the results from both dark and light matter, as also tested by studying the dark and light matter distributions in the bullet cluster (Clowe et al. 2006).

Predictions of cluster ellipticities come mostly from numerical simulations (West et al. 1989; de Theije et al. 1995; Jing & Suto 2002; Floor et al. 2003; Ho & White 2004; Flores et al. 2007; Rahman et al. 2006). The ellipticity is expected to depend on cosmological parameters (Evrard et al. 1993; Splinter et al. 1997; Buote & Xu 1997; Suwa et al. 2003; Rahman et al. 2004) and to evolve with redshift (Kasun & Evrard 2005; Allgood et al. 2006), an evolution which itself might depend on cosmology (Hopkins et al. 2005; Ho et al. 2006). The distribution of subhalos within a cluster halo is found to be an indicator of the overall halo ellipticity (Bode et al. 2007) but is slightly less elliptical.

The ellipticity of the brightest cluster galaxy and the ellipticity of the distribution of cluster member galaxies are much easier to observe than any other cluster ellipticity measure. This has been studied by a number of authors (West & Bothun 1990;

Plionis et al. 1991; Rhee et al. 1991; Strazzullo et al. 2005). Most recently, Wang et al. (2008) studied groups of galaxies in the Sloan Digital Sky Survey (SDSS) and found an alignment between the brightest cluster galaxy (BCG) and the distribution of galaxies, which was strongest in the most massive groups and between red BCGs and red group member galaxies.

In this paper, we focus on measuring the dark matter ellipticity directly using gravitational lensing. We also compare this ellipticity to the ellipticity of the cluster member galaxy distribution to see how reliable a tracer of ellipticity the light is, and therefore whether it can be used by itself for cosmological studies.

Gravitational lensing has been used very successfully to measure the mass and profile of clusters of galaxies by many authors. The work most relevant to our study is that of Sheldon et al. (2001); Sheldon et al. (2007b) and Sheldon et al. (2007a) who stack the lensing signal from many clusters of galaxies to find an average signal. Natarajan & Refregier (2000) proposed that when stacking the shear signal from many halos the stack could be made while retaining information about the major axis of the halo, as observed from the distribution of light. The stacked shear map should then provide a constraint on the ellipticity of the dark matter halo, if indeed the mass and light were aligned. They considered lensing by galaxies, but we apply the same technique to clusters of galaxies here.

The ellipticity of the dark matter distribution has been studied observationally for galaxy-sized halos using gravitational lensing using data from the Red-Sequence Cluster Survey (Hoekstra et al. 2004), the SDSS (Mandelbaum et al. 2006), and the Canada–France–Hawaii Telescope Legacy Survey (CFHTLS; Parker et al. 2007). This has proved to be extremely difficult and we present here, for the first time, results from stacking galaxy cluster halos. Cypriano et al. (2004) has previously made measurements of the cluster dark matter ellipticity using gravitational lensing measurements from individual clusters. They found a good agreement between the dark matter halo orientation and the orientation of the brightest cluster galaxy.

When calculating angular diameter distances and the mean density of the universe, we assume a flat cosmology with

$\Omega_m = 0.3$. The Navarro–Frenk–White (NFW) halo profile has a very weak dependence on the fluctuation amplitude. We assume $\sigma_8 = 0.8$ for this calculation.

The structure of this paper is as follows. In Section 2, we describe our data set and operations we have performed on the data such as rotating and stacking and removal of neighboring clusters. In Section 3, we use two theoretical models—a Singular Isothermal Ellipsoid (SIE) and NFW (see Navarro et al. 1997) model—of the mass and light distribution, and look at correction factors from the redshift distribution and cluster decontamination. Our results, and some interpretations of these, are presented in Section 4. Conclusions are summarized and discussed in Section 5.

2. DATA

In this section, we describe the catalogues used and the operations we carried out before comparing with models, including cluster selection and stacking and rotating.

2.1. Catalogues

We use the cluster catalogue of Koester et al. (2007a), which is at the present time the largest existing galaxy cluster catalogue, consisting of 13,823 galaxy clusters from the SDSS (York et al. 2000). The cluster galaxies are red-sequence members (occupying the so-called E/S0 ridgeline in color–magnitude space), brighter than $0.4L_*$ in the i band and between redshifts $0.1 < z < 0.3$. They also lie within a circular aperture of radius R_{200} , which is the estimated radius within which the density of galaxies with $24 < M_r < 16$ is 200 times the mean density of such galaxies. The number of cluster members inside this aperture is $10 \leq N_{\text{gals}}^{r200} \leq 188$; the lower limit is a requirement for inclusion into the catalogue. We refer to Koester et al. (2007a) for details of the catalogue and to Koester et al. (2007b) for a description of the cluster selection algorithm.

In order to define an isolated sample, we removed clusters found to be too close to each other, as seen on the sky. Details on this close neighbor removal can be found in Section 2.2. Clusters that are too close to the survey edge are also removed, with the requirement that the minimum distance from the cluster center to the survey edge is $7 h^{-1}$ Mpc. We are left with a total of 4281 clusters to analyze for our purposes. We have also organized the clusters into four redshift bins between $z = 0.10$ and $z = 0.30$, each of width 0.05 in z . Since these cluster redshifts are photometric, with uncertainties of ~ 0.01 (Koester et al. 2007a), the spectroscopic bin width will be very slightly larger than the photometric bin width. We do not take into account this small broadening in our analysis, because we expect it to have negligible effect on the ellipticity results.

The shear galaxy catalogue is the same as used in Sheldon et al. (2004), except that the area covered is larger, $\sim 6325 \text{ deg}^2$. There is approximately one galaxy per square arcminute in this catalogue. Galaxies in the shear catalogue have extinction-corrected r -band Petrosian magnitudes less than 22. Stars have been removed from the catalogue by the Bayesian method discussed in Scranton et al. (2002). Unresolved galaxies and objects with photo- z errors greater than 0.4 have also been removed. To correct the shapes of galaxies for effects of point-spread function (PSF) dilution and anisotropy, the techniques of Bernstein & Jarvis (2002) were used, with modifications specified in Hirata & Seljak (2003). We refer to Sheldon et al. (2004) for full details of the compilation of the shear catalogue.

We do not want to include in the shear catalogue galaxies which are already in the cluster member catalogue. Therefore we remove from the shear catalogue all galaxies which are close, as seen on the sky, to a cluster member. We cut on a physical (as opposed to angular) distance of $0.012 h^{-1}$ Mpc, as calculated at the redshift of the cluster. This distance corresponds to 5 arcsec at redshift $z = 0.2$. In principle, this cut may also remove some real background galaxies; however, the shear measurements of these galaxies will in any case likely be adversely affected by the light contamination by the cluster members. Note that we do not eliminate *all* cluster members from the shear catalogue with this cut, only those clusters that fit the selection criteria set by the maxBCG selection method (red galaxies, brighter than $0.4 L_*$; Koester et al. 2007a).

2.2. Postage Stamp Size and Close Neighbor Removal

In order to avoid contamination of the shear signal from neighboring structures, we only include in our analysis galaxies which are sufficiently close to a cluster, as seen on the sky. We decide this distance by considering the predicted contribution of neighboring clusters to the shear signal, and then use this to decide the required separation of neighboring clusters.

We include in our shear catalogue galaxies in a square postage stamp of $10 \times 10 h^{-1}$ Mpc centered on each cluster. This choice was made using Figure 8 of Johnston et al. (2007), which shows model fits for the lensing signal split up into contributions from several components. We want the lensing signal in our postage stamp to be dominated by the central cluster, not by the contribution from neighboring mass concentrations such as nearby clusters and filaments. Our interest therefore lies in comparing their NFW profile (green line) to the contribution from neighboring halos (blue line). The results in their Figure 8 are shown for 12 richness (N_{gals}^{r200}) bins. The mean of the N_{gals}^{r200} values of our cluster sample is ~ 24 , directing us to the panel $N_{\text{gals}}^{r200} [18-25]$. We match our postage stamp limit at the radius where the NFW contribution is roughly equal to that of the contribution from neighboring clusters. Note that we are also removing close neighbors (see below), so the contribution from neighboring halos would actually be even lower for our case, so our cut may be conservative.

Clusters that are *too* close to each other in projected separation represent a challenge for our analysis. The mass distribution of a cluster will affect the shear field of its neighbor. This could have a significant effect on the measured ellipticity. While it is possible to isolate clusters in three dimensions within a simulation, we are plagued by overlaps on the sky since gravitational lensing measures the projected mass. We therefore endeavor to remove this complication by selecting relatively isolated clusters for this analysis. For proper comparison with theory, a similar sample should be made from simulations. However, in this paper, we are primarily concerned with the first significant detection of ellipticity in a large sample.

We do not want the shear from a neighbor to appear within our postage stamp, but this is unavoidable to some extent, because the shear at one point is affected by mass far away (shear is nonlocal). The effect on the measured ellipticity of having neighbors is twofold. (1) It can make the distribution more circular, if the neighbor position is uncorrelated with the cluster major axis. This will occur due to chance alignments close to the line of sight, particularly from clusters in different redshift bins. (2) It can make the distribution more elliptical, if the neighbor position is correlated with a major axis direction. Pairs of clusters which are physically close will probably be

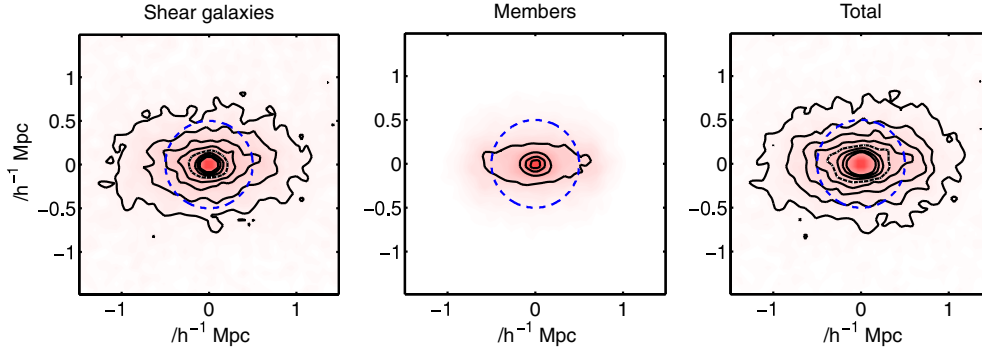


Figure 1. Total number of galaxies per unit area for redshift bin 3 ($0.20 < z < 0.25$) for illustration. From left to right: shear galaxies, cluster members, and total galaxies (shear galaxies plus cluster members). The left and right panels include galaxies which are uncorrelated with the cluster. We draw our contours relative to the constant background level (which is the same number in both left and right panels, since the cluster member catalogue does not contribute). For the left and right panels, contours are equally spaced from 1.2 to 2.6 times the background level, in steps of 0.2. The dashed contour shows 2 times the background level. For the central panel the contours are 0.2, 0.4, 0.6, 0.8 times the same background level. The dashed circle shows location of mask, see text. For comparison, a $3 \times 10^{14} h^{-1} M_{\odot}$ cluster at a redshift of 0.2 has $R_{200} \sim 1.4 h^{-1} \text{ Mpc}$, where R_{200} is the radius within which the mean density of the cluster is 200 times the mean matter density at the cluster redshift. We have zoomed in to show the central part of the postage stamp for clarity.

(A color version of this figure is available in the online journal.)

aligned along the major axis of the cluster (e.g., Plionis et al. 1991).

We therefore remove clusters that are closer than $5 h^{-1} \text{ Mpc}$ (corresponding to half the width of the postage stamp) to neighboring clusters. When a cluster has one or more neighbors with an angular separation corresponding to less than $5 h^{-1} \text{ Mpc}$, calculated at the middle of the redshift bin of the cluster (see later), we discard it if any of the neighbors have a higher N_{gals}^{r200} . The neighbor removal was done consecutively from low-to-high redshift. This process reduced the number of available clusters to 4281. In a later section, we analyze the use of different minimum close neighbor distances.

Although we remove a cluster's less rich neighbors from our sample, the shear pattern of the remaining cluster will already have been affected by its neighbor(s). However, by retaining the richest of the neighboring clusters, we hope that the shear field is dominated by this cluster.

2.3. Stacking and Rotating

On average, we have only around 1 shear galaxy per square arcminute and the uncertainty on the shear for a single galaxy is an order of magnitude larger than the shear we are trying to measure. Therefore we need to use the shear signal from many clusters in order to obtain a significant signal. We therefore stack the clusters on top of each other to improve the signal-to-noise ratio. In other words, we use information from the postage stamp field of shear galaxies for all clusters simultaneously.

The stacking could be carried out in either physical or angular space. For our method, the two approaches are exactly equivalent if the redshift bins are small enough. We stack in angular space and use redshift bins of redshift width 0.05. This causes a radial blurring, because two clusters of the same physical size will be stacked on top of each other in angular space to have different angular sizes. The blurring of the shear and light maps will be of at worst plus and minus 20% (for the lowest redshift bin). Since superposing ellipses of different scalings retains the original ellipticity, this results in a slightly smoother cluster profile but will not affect our ellipticity results. We find that our results are fairly similar even when comparing two very different profiles, see Section 3.

Straightforward stacking of elliptical clusters with random orientations would erase any ellipticity and produce a circular average cluster. Before stacking, we therefore rotate each cluster

to lie along an x -axis, which is the major axis as defined by the ellipticity of the cluster members (see Figure 1). This rotate-and-stack method is described by Natarajan & Refregier (2000) for use in galaxy–galaxy lensing, and we have, for the first time, applied this technique for use on cluster lensing.

We calculate the direction of a cluster major axis from the positions of the cluster members, as defined in the cluster catalogue. We do not take into account the luminosity of each cluster member. The cluster center (x_c, y_c) was taken to be the position of the BCG as defined by the maxBCG algorithm (Koester et al. 2007b). However, the position of the BCG is not necessarily coincident with the cluster's actual center of mass. For comparison, we therefore calculate the center of each cluster as given by the mean position of the cluster members. The mean physical offset (for redshift bin $0.20 < z < 0.25$) between the two center definitions is $\sim 0.15 h^{-1} \text{ Mpc}$, and the standard deviation $0.09 h^{-1} \text{ Mpc}$. Compared to our mask radius of $0.5 h^{-1} \text{ Mpc}$, therefore, the shift in center position is relatively small. Any effect this mis-centering does have will increase the ellipticity of the members, which we do not focus on here, and cause the misalignment angle to tend toward the direction from the BCG to the center of the cluster member distribution. This would in itself be an alternative and potentially useful way to stack the clusters to obtain the results presented here. Therefore, we do not consider this effect further.

To find the ellipticity angle of rotation of the cluster, we use the quadrupole moments of the cluster members. The quadrupole moments are given by

$$Q_{xx} = \langle (x_i - x_c)^2 \rangle_i \quad (1)$$

$$Q_{xy} = \langle (x_i - x_c)(y_i - y_c) \rangle_i \quad (2)$$

$$Q_{yy} = \langle (y_i - y_c)^2 \rangle_i, \quad (3)$$

where the summation i is over the cluster members. We convert this into the ellipticity components e_1 and e_2 of the cluster through the relations

$$e_1 = \frac{Q_{xx} - Q_{yy}}{Q_{xx} + Q_{yy} + 2\sqrt{Q_{xx}Q_{yy} - Q_{xy}^2}} \quad (4)$$

$$e_2 = \frac{2Q_{xy}}{Q_{xx} + Q_{yy} + 2\sqrt{Q_{xx}Q_{yy} - Q_{xy}^2}}. \quad (5)$$

The angle of the cluster, anticlockwise from the positive x axis, is then

$$\theta^{\text{rot}} = \frac{1}{2} \text{atan}\left(\frac{e_2}{e_1}\right). \quad (6)$$

We rotate the positions of the cluster member galaxies and the positions of the shear galaxies using the following transformation:

$$x^{\text{rot}} = d \cos(\theta - \theta^{\text{rot}}) \quad (7)$$

$$y^{\text{rot}} = d \sin(\theta - \theta^{\text{rot}}), \quad (8)$$

where (d, θ) are the polar coordinates of the galaxy to be rotated, relative to the cluster center. For clusters with ellipticities close to zero, θ^{rot} in Equation (6) has little meaning. From the cluster members alone, 18% of our clusters have an ellipticity ($e = \sqrt{e_1^2 + e_2^2}$, using Equations (4) and (5)) of less than 0.1 and only 5% have ellipticities less than 0.05. Therefore, the angle is reasonably well defined. Two per cent of the clusters have an ellipticity greater than 0.5. The cluster selection criteria by Koester et al. (2007a) and/or our isolation criteria have therefore done a reasonable job of identifying isolated clusters. In addition, the clusters seem relatively undisturbed, i.e., have low ellipticity. This also illustrates that it would not be particularly useful to bin the clusters according to the cluster member ellipticity because the range is relatively small (and our final signal to noise is quite low).

Figure 1 shows the number of galaxies per unit area, for z bin 3, after stacking and rotating. The left panel shows galaxies from the shear galaxy catalogue, with cluster member catalogue galaxies removed, the middle panel shows cluster galaxies from the cluster member catalogue and the right panel shows the sum of shear galaxies and cluster members.

The left-hand panel clearly contains a significant number of cluster members, despite the fact that the galaxies from the cluster member catalogue are not included. As described in Koester et al. (2007b), cluster members for this catalogue were identified using the maxBCG algorithm. This algorithm employs the red-sequence method, based on the observational fact that cluster galaxies occupy a narrow region (a so-called *ridgeline*) in a color–magnitude diagram. This method is designed to conservatively select red galaxies at the central area of a cluster. As an illustration, we investigate the central region of the stacked cluster in the third redshift bin ($0.2 < z < 0.25$). In the central square arcminute, the number of galaxies in the member catalogue is $\sim 40\%$ of the number of galaxies in the (members removed) shear catalogue, after subtracting the constant background level, i.e., most of the cluster members are not in the cluster member catalogue.

The existence of these extra members allows a very convenient check on our stacking and rotating: the rotation angles were calculated from the cluster member catalogue alone, whereas the left-hand panel does not include the galaxies used to decide the rotation angle. Therefore, the fact that we see ellipticity in this panel means that the angle calculated from the members catalogue is correlated with the angle of the extra cluster members. If, for example, we had calculated rotation angles from a very small number of galaxies from the cluster member catalogue, there would be a large degree of randomness due to shot noise, and the alignment of measured and true ellipticity would be random to a large extent, resulting in a circular pattern in the left panel of Figure 1.

The object of this paper is to calculate the ellipticity of the dark matter, as measured from gravitational lensing, and compare it with that of the light-emitting galaxies. Any misalignment in the stacking and rotating will tend to make the dark matter appear less elliptical. However, this misalignment will have the same effect on the ellipticity of the light, as measured from the extra cluster members (left-hand panel) alone. Therefore, we can compare like with like, and assess the *relative* ellipticity of the dark and light matter, despite any misalignment.

We have chosen the contour levels so that a fair comparison can be made between the left and central panels: the outermost contour corresponds to the same cluster member density in each. Therefore, we see that at large radii most of the cluster members are not included in the cluster member catalogue. For all the axis ratio measurements reported in this paper we exclude the central regions (see Section 3.3), this is shown by the dashed circle in Figure 1. Outside this excluded region, we see that the contours change only a little from the left to the right panel. This is convenient because it means that it is not too important whether we compare the dark matter ellipticity with the light ellipticity derived from either the left- or the right-hand panel.

We calculate the tangential, $\hat{\gamma}_T$, and cross, $\hat{\gamma}_X$, components of the shear $\hat{\gamma}$ for each shear galaxy

$$\hat{\gamma}_T = \hat{\gamma} \cos(2\alpha) \quad (9)$$

$$\hat{\gamma}_X = \hat{\gamma} \sin(2\alpha), \quad (10)$$

where α is the angle between the shear galaxy major axis and a tangent through the center of the shear galaxy, with respect to the cluster center. We calculate the shear estimate for each galaxy from the polarizations (ϵ) in the shear galaxy catalogue

$$\hat{\gamma} = \frac{1}{2S_{\text{Sh}}} \epsilon, \quad (11)$$

where the factor $S_{\text{Sh}} \sim 0.88$ is the average responsivity of the source galaxies to a shear, see Sheldon et al. (2001) and references therein, and $\epsilon = (a^2 - b^2)/(a^2 + b^2)$, where a is the semimajor and b is the semiminor axis of the shear galaxy. We have redone our main NFW dark matter ellipticity result using a value S_{Sh} which is 20% higher, and find only a negligible change. Note that the tangential and cross shears are invariant with respect to rotation of the cluster coordinates. We bin the shear galaxy catalogue into square pixels of size 0.4×0.4 on the sky, but our main results are insensitive to this exact value. We average the shear estimates in each pixel.

Figure 2 shows the smoothed tangential shear. As expected, the tangential shear is largest in the cluster center. To interpret this figure further it is helpful to consider the tangential and cross shears pattern predicted from popular cluster models, discussed further in Section 3. Cluster ellipticity causes little, if any, cross shear, depending on the cluster profile. For an elliptical SIE, the cross shear is exactly zero. For an elliptical NFW with a major to minor axis ratio of 0.5 (our best fit result), a mass of $1 \times 10^{14} h^{-1} M_{\odot}$ and cluster redshift 0.15, the maximum cross shear occurs when approaching the center of the lens. Just outside our mask radius of $0.5 h^{-1} \text{ Mpc}$, the maximum cross shear is 0.0012 for a source redshift of 0.3. This value is 10% of the maximum tangential shear outside the mask, and is therefore small compared to our uncertainties. The main effect of cluster ellipticity is to produce an ellipticity in the tangential shear map. Therefore, the tentative visual indication of some

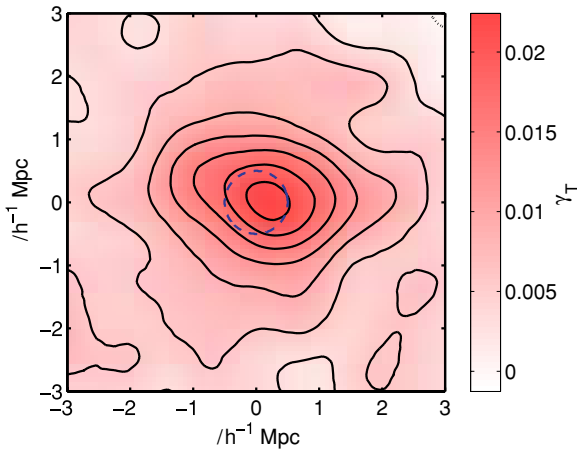


Figure 2. Tangential shear, $\hat{\gamma}_T$, as measured from all galaxies in the background galaxy catalogue for a zoomed-in view of the postage stamp. To reduce the noise, we have smoothed with a Gaussian with standard deviation $1 h^{-1}$ Mpc. The location of the mask is shown by the dashed circle.

(A color version of this figure is available in the online journal.)

horizontal elongation in this figure is our first hint of dark matter ellipticity.

To compare the data with models, we must incorporate the errors on the shear estimates. The errors on the shear measurements are given by

$$\sigma_{\gamma_T}^2 = \sigma_i^2 + \sigma_{\text{SN}}^2, \quad (12)$$

where σ_i is the uncertainty in the shape measurement due to the finite number of photons falling in each detector element, plus detector noise, and σ_{SN} is the “shape noise” due to intrinsic variance in the unlensed galaxy shapes (assumed the same for all galaxies).

We calculate the shape measurement uncertainty σ_i from the uncertainties in the two components of the ellipticity e_1 and e_2 , using

$$\sigma_i = \frac{1}{2S_{\text{Sh}}} \frac{\sigma_{e1} + \sigma_{e2}}{2}. \quad (13)$$

The first factor converts from e to γ and the second part assumes that the uncertainty on the two ellipticity components is essentially equal and uncorrelated, which is approximately true for some shear estimators (e.g., Figure 2 of Bridle et al. 2002). If these assumptions are true then it follows that the ellipticity uncertainty on a component is independent of rotation.

We estimate the shape noise σ_{SN} by calculating the rms dispersion in $\hat{\gamma}_T$ values as a function of σ_i . We compare this to σ_{γ_T} for various σ_{SN} values and find $\sigma_{\text{SN}} = 0.24$ to be the best fit.

To find the error on the shear for each pixel, we take the mean of the errors σ_{γ_T} and divide by the square root of the number of galaxies in the pixel. Galaxies will have a range of sizes and therefore of measurement errors. When we calculate the average shear in each pixel we do not weight the galaxies according to their ellipticity errors. This is because this would tend to upweight the better measured galaxies. As better measured galaxies may preferentially tend to be cluster members that have leaked into the shear galaxy catalogue, this might preferentially weight up cluster members. This would have to be taken into account when removing the bias on the shear due to cluster member contamination (see Section 3.3), which would be difficult. We therefore use all the galaxies in the shear galaxy

catalogue without weighting. Due to the cuts already made in creating the shear galaxy catalogue, the difference in weight between the noisiest and least noisy galaxies is only 30%; therefore, the weighting would not make a large difference to our analysis.

3. MODELING

3.1. Mass and Light Distributions

The shear of galaxies depends on the mass and structure of the cluster acting as a lens. To model the cluster mass distribution, we use two alternative theoretical models: an SIE and an NFW model. The NFW model is preferred from simulations, but we also include results from the simpler SIE model to show an extreme and simple example of the dependence of our results on the cluster profile.

The SIE model corresponds physically to a distribution of self-gravitating particles with a Maxwellian velocity distribution with one-dimensional velocity dispersion σ_v . The convergence (normalized mass density) $\kappa = \Sigma/\Sigma_{\text{crit}}$ of an SIE is given by

$$\kappa = 2\pi \frac{\sigma_v^2}{c^2} \frac{D_{\text{ds}}}{D_s} r^{-1}, \quad (14)$$

where r is the generalized radius

$$r = (x^2 f + y^2 f^{-1})^{1/2} \quad (15)$$

and $f = b/a$ is the axis ratio of the ellipse ($b < a$), σ_v is the velocity dispersion, and c is the speed of light. x and y are coordinates in the plane of the sky at the cluster redshift. The distances D_{ds} and D_s are the angular diameter distances between the lens (deflector) and the source, and from the observer to the source, respectively. The SIE peaks sharply in the central parts, but we mask out the central regions (see Section 3.3). For the SIE model, we have the simple relation that the normalized surface density equals the tangential shear $\gamma_T = \kappa$ (Kassiola & Kovner 1993; Kormann et al. 1994).

The NFW model is a more complicated but more realistic model based on numerical simulations. In order to implement the NFW, we need the projected mass of the cluster. To calculate the projected mass, we use the equations given in Wright & Brainerd (2000) and Bartelmann (1996) using our generalized radius of Equation (15) to make the cluster mass distribution elliptical. We use M_{200} , the mass enclosed within the radius at which the density is 200 times the mean density of the universe, for consistency with simulations. We derive the concentration parameter, c , where $c \propto M^\beta$ according to Equation (12) of Seljak (2000), where we interpret the virial mass M as M_{200} . We use $\beta = -0.15$, as appropriate for an NFW model. The shear for an elliptical mass distribution is calculated using the equations in Keeton (2001) which are derived from those in Schramm (1990). A shear map using these equations is illustrated in Figure 1 of Bridle & Abdalla (2007).

We calculate probability as a function of our free parameters in each redshift bin, and marginalize over all but the axis ratio f . We then obtain a single result for f from combining all the redshift bins by multiplying the probabilities from different redshift bins together for each f value. This is the correct calculation if we believe that the other parameters have different values in each redshift bin, but that f is the same for all redshift bins.

3.1.1. Estimation of the Light Matter Axis Ratio (f_{LM}) using Galaxy Positions

When stacking the clusters (Section 2.3), we calculated individual cluster ellipticities based on the cluster galaxies in the members catalogue. We do not use these results as our measure for the light matter ellipticity for the stacked cluster, because they are relatively noisy due to the small number of members (~ 10 for the least rich clusters). Furthermore, we know that the members catalogue does not in fact contain all the cluster members, and has some selection criteria that may affect the ellipticity (requirement on proximity to cluster center). We therefore use a χ^2 analysis to find the light matter ellipticity of the clusters. We model the light map as coming from (1) noncluster galaxies which have a constant density across the postage stamp plus (2) a contribution from the cluster galaxies which is assumed to have a galaxy density proportional to the mass profiles of Equation (14)

$$n^{\text{pred}}(\mathbf{r}) = K\kappa(\mathbf{r}) + n_0, \quad (16)$$

where n_0 is the background level of galaxies per pixel and K is a constant. Note that we do not assume that the light is some constant multiple of the mass, only that the light map is proportional to an SIE or NFW profile (which may have different parameters than the dark matter distribution). We do not tie the dark and light map parameters together, because we wish to investigate whether the dark and light distributions both have the same ellipticity. For practical purposes, we fix the mass at $M_{200} = 10^{14} h^{-1} M_\odot$ in this calculation, which corresponds approximately to clusters of the mean richness we used (Johnston et al. 2007, Table 6). The value used affects the concentration parameter and therefore the mass profile of the cluster, which affects the weighting of the map. If we use a value a factor of 10 higher, our light ellipticity results change by less than 1σ and in any case our main results, on the dark matter ellipticity, are changed imperceptibly because the uncertainties on those are dominated by the much larger uncertainty on the dark matter quantities.

We calculate probabilities in the resulting three-dimensional space (f_{LM} , K , and n_0) by calculating a χ^2 between the predicted number (Equation (16)) and the observed number

$$\chi^2 = \sum_i \frac{(n^{\text{pred}}(\mathbf{r}_i) - n_{\text{obs}}(\mathbf{r}_i))^2}{\sigma_{n_i}^2} \quad (17)$$

and calculating probabilities from this, $\text{Pr} = e^{-\chi^2/2}$.

Our assumption is that the errors are Poisson, therefore in the limit of large numbers the error on the number of galaxies, as used in the χ^2 calculation, is $\sigma_{n_i} = \sqrt{n^{\text{pred}}(\mathbf{r}_i)}$. We calculate our main results for each of the three stacked light maps shown in Figure 1.

3.1.2. Estimation of the Dark Matter Axis Ratio (f_{DM}) from the Stacked Shear Map

To estimate the ellipticity of the dark matter distribution, we calculate probability as a function of the cluster axis ratio f_{DM} and cluster mass. We calculate the probability from χ^2 between the observed and predicted shears, using the uncertainty on the shear values from Equation (12). We marginalize over the cluster mass with a flat prior to obtain the probability as a function of the two-dimensional axis ratio f_{DM} .

3.2. Redshift Distributions

As discussed in Section 2, we divide our cluster sample up into four redshift bins. Due to the large photometric redshift uncertainties we decided not to use the redshift information in the shear galaxy catalogue. Therefore the “shear galaxies” may be in front of, behind, or part of the cluster. The shear for each lens–source pair depends on the redshift of both the lens (cluster) and the source (shear galaxy). To calculate our theoretical model, we need a prediction for the distance ratio in Equation (14) at each possible redshift. This must be averaged, weighted by the number of galaxies at each redshift. In other words, we need to calculate

$$\left\langle \frac{D_{ds}}{D_s} \right\rangle = \frac{\int_{z_L}^{\infty} (D_{ds}/D_s) n(z_s) dz_s}{\int_0^{\infty} n(z_s) dz_s}. \quad (18)$$

Note that the integration in the nominator starts at the lens redshift, z_L , so that galaxies between us and the lens do not contribute to the shear signal, as they are not influenced by the presence of the cluster. We estimate $n(z_s)$ from Figure 3 and Equation (8) in Sheldon et al. (2001), and as a result we use $z_c = 0.22$. However, our results are quite insensitive to these numbers because we focus only on the ellipticity of the dark matter halo and not on its mass.

We obtain $\langle D_{ds}/D_s \rangle = [0.51, 0.37, 0.26, 0.17]$ for the four redshift bins. The values are low for high redshift bins, because a large fraction of the galaxies are between us and the cluster, and therefore do not contribute to the shearing effect. The calculation of D_{ds}/D_s is approximate, because we assume all clusters to be located at the center of their redshift bin. However, this does not affect the ellipticity of the theory prediction. The distance ratio is incorporated into the predictions using Equation (14).

3.3. Cluster Decontamination

Because spectroscopic redshifts are not available for all shear catalogue galaxies, there will always be a degree of contamination by cluster members in the shear signal (as seen in Figure 1(a)). Since we assume that the cluster members have no systematic alignment (but see Section 5 for an assessment of the implications of this assumption), members that have leaked into the shear galaxy catalogue will tend to dilute the shear signal. We correct for this dilution in our analysis. The corrected shear is given by

$$\gamma_{\text{cor}} = \frac{n(\mathbf{r})}{n_0} \hat{\gamma}, \quad (19)$$

where $n(\mathbf{r})$ is the total number of galaxies in the shear galaxy catalogue at a two-dimensional position \mathbf{r} from the center, n_0 is the number of galaxies not in the cluster (see Equation (16)) and $\hat{\gamma}$ is the observed, uncorrected shear. We use the best fit n_0 value from the χ^2 fit to the light matter distribution. Inside the cluster, we have $n(\mathbf{r}) > n_0$, so the observed shear will be boosted by correcting for the contamination.

We mask the central regions from our analysis for several reasons. (1) In the very central regions, cluster members will obscure the shear galaxies. (2) The cluster center may be incorrect and thus the central parts may appear erroneously circular after the stacking. (3) There is actually an uncertainty associated with the correction factor that we have not taken into account. This error is due to Poisson fluctuations in the true number of noncluster members per pixel, and will be more significant when the value of the correction factor is large, which occurs in the central region where the observed number

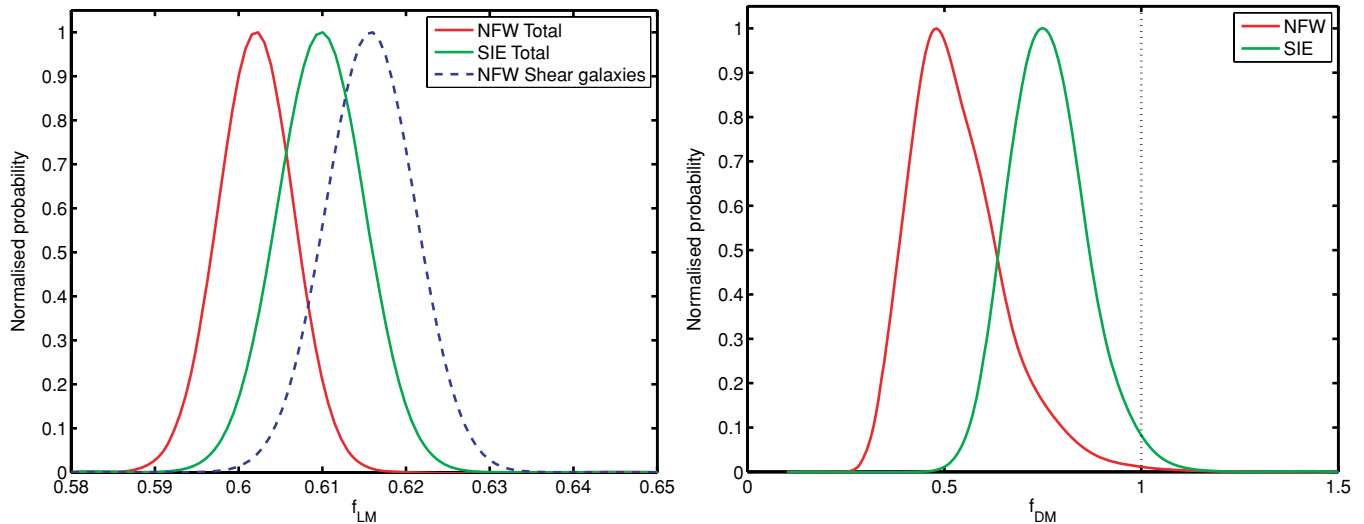


Figure 3. Left panel: relative probability distribution of the axis ratio $f_{\text{LM}} = b/a$ for the galaxy number density map from the shear catalogue plus member catalogue, thus including all cluster members. This includes clusters at all redshifts for an NFW model (dark, red line) and an SIE model (light, green line). The dashed line shows the result from shear catalogue galaxies only (for an NFW model). Right panel: relative probability distribution for the dark matter axis ratio f_{DM} . The dark, red line shows result from the NFW model, and the light, green line shows result from the SIE model. The dotted vertical line shows $f_{\text{DM}} = 1$ corresponding to a circular distribution.

(A color version of this figure is available in the online journal.)

Table 1
Axis Ratio Results for the Light Maps

Population	z	SIE (f_{LM})	NFW (f_{LM})
Shear galaxies	$0.10 \leq z \leq 0.15$	$0.548 + 0.013 - 0.013$	$0.620 + 0.015 - 0.015$
Total	$0.10 \leq z \leq 0.15$	$0.555 + 0.014 - 0.014$	$0.614 + 0.012 - 0.013$
Members	$0.10 \leq z \leq 0.15$	$0.302 + 0.006 - 0.006$	$0.544 + 0.006 - 0.007$
Shear galaxies	$0.15 \leq z \leq 0.20$	$0.672 + 0.011 - 0.011$	$0.649 + 0.012 - 0.012$
Total	$0.15 \leq z \leq 0.20$	$0.657 + 0.012 - 0.011$	$0.631 + 0.010 - 0.010$
Members	$0.15 \leq z \leq 0.20$	$0.261 + 0.005 - 0.005$	$0.475 + 0.006 - 0.006$
Shear galaxies	$0.20 \leq z \leq 0.25$	$0.581 + 0.012 - 0.012$	$0.583 + 0.011 - 0.010$
Total	$0.20 \leq z \leq 0.25$	$0.578 + 0.011 - 0.010$	$0.575 + 0.009 - 0.009$
Members	$0.20 \leq z \leq 0.25$	$0.254 + 0.004 - 0.004$	$0.456 + 0.005 - 0.005$
Shear galaxies	$0.25 \leq z \leq 0.30$	$0.637 + 0.010 - 0.009$	$0.619 + 0.008 - 0.008$
Total	$0.25 \leq z \leq 0.30$	$0.624 + 0.008 - 0.008$	$0.602 + 0.007 - 0.007$
Members	$0.25 \leq z \leq 0.30$	$0.235 + 0.003 - 0.003$	$0.434 + 0.004 - 0.004$
Joint (total)	$0.10 \leq z \leq 0.30$	$0.610 + 0.005 - 0.005$	$0.602 + 0.004 - 0.005$

of galaxies in the shear galaxy catalogue peaks sharply. For all these reasons, we mask out the central region using a circular mask with $r_{\text{mask}} = 0.5 h^{-1}$ Mpc. The radius of the mask was set where the correction factor increases above 1.5 (as calculated for $0.20 < z \leq 0.25$), shown by the dashed circle in Figure 1. This corresponds to 3.3 arcmin at $z = 0.225$.

4. RESULTS

We now present our results on the stacked cluster ellipticity, focusing first on the NFW profile.

4.1. Results for the Light Matter Axis Ratio (f_{LM})

The left panel of Figure 3 shows the one-dimensional relative probability of the axis ratio f_{LM} , marginalized over K and n_0 (see Equation (16)). The solid lines represent results from using the total cluster members, i.e., galaxies in both the shear galaxy catalogue and cluster member catalogue (corresponding to the right-hand panel of Figure 1). The blue, dashed line shows results from using only the (members-removed) shear catalogue galaxies, corresponding to the left-hand panel of

Figure 1, for the NFW model. This shows that the light matter distribution is clearly elliptical with an axis ratio of $f_{\text{LM}} \sim 0.6$. The errors on f_{LM} are calculated by finding the 68% iso-probability limits from the probability distribution $P(f_{\text{LM}})$ after marginalizing over the other fit parameters. We find an error of ~ 0.005 .

Table 1 shows three light matter ellipticity results for each redshift bin and for each theoretical model (SIE and NFW): (1) for the shear catalogue galaxies with cluster members removed; (2) for the total cluster members; and (3) for the cluster members and (members from the cluster catalogue plus the extra members included in the shear galaxy catalogue). The results from the NFW and SIE are qualitatively similar. The last line in Table 1 shows the joint results combining all bins, for the total cluster members.

There is a clear detection of ellipticity based on the number density of shear catalogue galaxies alone. We see that the distribution of galaxies in the members catalogue is more elliptical than that of the shear catalogue. This is not surprising because we stacked the galaxies according to the members catalogue. Even if the galaxies in the members catalogue had

Table 2
Axis Ratio Results for the Dark Matter Distribution

z	SIE (f_{DM})	NFW (f_{DM})
$0.10 \leq z \leq 0.15$	$0.754 + 0.230 - 0.186$	$0.614 + 0.400 - 0.176$
$0.15 \leq z \leq 0.20$	$0.522 + 0.159 - 0.115$	$0.269 + 0.158 - 0.054$
$0.20 \leq z \leq 0.25$	$0.958 + 0.251 - 0.199$	$0.599 + 0.379 - 0.208$
$0.25 \leq z \leq 0.30$	$0.853 + 0.306 - 0.215$	$0.614 + 0.444 - 0.266$
Joint analysis	$0.747 + 0.102 - 0.094$	$0.480 + 0.136 - 0.086$

been sampled from a circular distribution then the finite number of galaxies would provide a rotation direction, so we would have in effect stacked the random noise to produce an ellipticity for the cluster members, while making the light map from the shear catalogue more circular.

This extra induced ellipticity could be simulated, but in fact there is no need, because the axis ratio from the shear galaxy catalogue alone is very similar to that based on the total catalogue containing both the shear catalogue *and* the cluster member catalogue. Therefore, we do not consider the results from only the cluster member catalogue any further.

The similarity of the ellipticities from the shear galaxy catalogue and the total catalogue is largely due to the fact that there are very few galaxies from the members catalogue outside our mask radius. The important conclusion for our paper is that any misalignment in the rotating and stacking will affect the light and dark matter ellipticity the same. The ellipticity observed in the light map makes us believe that the rotation angles are not completely random and therefore that we can hope to detect some ellipticity in the dark matter, if indeed the dark matter halo is elliptical.

4.2. Results for the Dark Matter Axis Ratio (f_{DM})

Ellipticity results for the dark matter analysis can be found in Table 2, for each individual redshift bin as well as for the joint result combining all redshift bins. For the NFW model, the joint result of $f_{DM} = 0.48^{+0.14}_{-0.09}$ excludes a circular mass distribution ($f_{DM} = 1$) by over 3σ (if the probability distribution is Gaussian). The lowest axis ratio is in the second redshift bin ($0.15 < z < 0.20$). We re-analyzed redshift bin 2 by dividing it into sub-bins, but found the result unchanged on removing the clusters with the lowest axis ratio. The joint result for the remaining redshift bins was then $f_{DM} = 0.607^{+0.21}_{-0.14}$. This is a weaker detection than our final result including the second redshift bin, but still a tentative detection of dark matter ellipticity.

The right panel of Figure 3 shows the probability as a function of the axis ratio for the dark matter distribution. The dark (red) line shows the result from using an NFW model, and the light (green) line shows the result from an SIE model. The vertical dotted line is showing $f_{DM} = 1$, which represents a circular mass distribution.

We can see from the figure that the probability is not totally Gaussian, with a tail to larger f_{DM} values. (Note that an axis ratio greater than unity corresponds to an ellipse aligned along the y axis.) We find that 99.6% of the probability is below $f_{DM} = 1$; therefore we consider this to be a reasonable detection of dark matter ellipticity. Note that the best-fit NFW result is quite a bit more elliptical than the SIE result, but the NFW result has a longer tail extending to higher f_{DM} values than the SIE. For the SIE model, 98.2% of the probability is below $f_{DM} = 1$. The NFW is a more realistic profile, so we trust these results most.

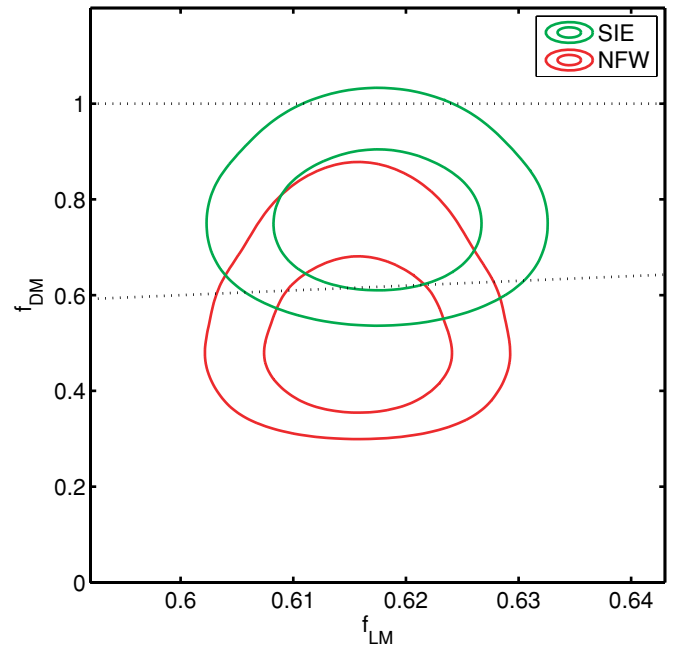


Figure 4. 68% and 95% contours of the two-dimensional probability distribution for the axis ratio of the dark matter (f_{DM}) vs. the axis ratio of the total galaxy number density distribution (f_{LM} , representing the light matter). Light (green) contours show the result from using an SIE profile as modeling the cluster, and dark (red) contours show result from using an NFW profile. The horizontal dotted line shows $f_{DM} = 1$, and the dotted line rising towards the right shows $f_{DM} = f_{LM}$.

(A color version of this figure is available in the online journal.)

Figure 4 shows 68% and 95% contours of the two-dimensional probability distribution for the axis ratio of the dark matter (f_{DM}) versus the axis ratio of the light matter (f_{LM}). The dotted lines also shown on the plot are $f_{DM} = 1$ (horizontal dotted line) and $f_{DM} = f_{LM}$ (dotted line rising toward the right). The two colors shown represent the different profiles used as cluster models: light (green) contours are for the SIE model, and dark (red) contours are for the NFW. We see that $f_{DM} = 1$, that is, a circular dark matter distribution, crosses just within the outermost (95%) contour for the SIE model and the NFW contours are both below the $f_{DM} = 1$ line.

Figure 5 shows the one-dimensional probability distribution as a function of the ratio of axis ratios of the dark and light matter: f_{DM}/f_{LM} . Again, the light (green) line is for the SIE model profile and the dark (red) line is for the NFW model. The vertical dotted line shows where we have $f_{DM} = f_{LM}$, that is, the axis ratio as deduced from the shear values equals the axis ratio as deduced from the distribution of the cluster galaxies. Both profiles are consistent with having the same ellipticity in the light and in the dark matter, $f_{DM}/f_{LM} = 1$. We find $f_{DM}/f_{LM} = 0.91^{+0.19}_{-0.25}$ for the NFW model and $f_{DM}/f_{LM} = 1.26^{+0.16}_{-0.17}$ for the SIE. The higher SIE result is driven by the larger f_{DM} for the SIE, which makes the dark matter distribution appear more round.

4.3. Dependence on Close Neighbor Distance

We made a decision to exclude all clusters with a more massive neighbor within an angular size corresponding to $5 h^{-1}$ Mpc at the cluster redshift. In this section, we test how dependent our results are on this decision. Table 3 shows that our main result changes little as the cut is made 50% smaller or larger. As expected, when a larger radius is used, fewer clusters survive in the catalogue, therefore the uncertainties become larger.

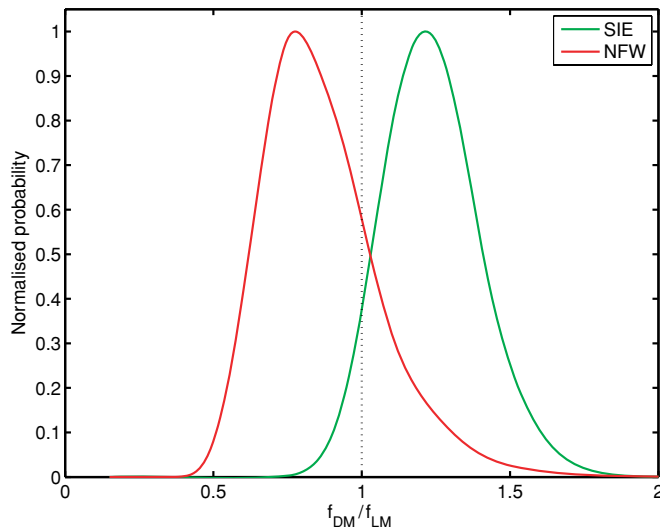


Figure 5. One-dimensional probability distributions as a function of the ratio $f_{\text{DM}}/f_{\text{LM}}$. Light (green) line is for the SIE result while dark (red) line is for the NFW result.

(A color version of this figure is available in the online journal.)

Table 3

Effect of Neighbor Removal on Measured Ellipticity. Results are Shown for the NFW Profile Only.

Cut/ h^{-1} Mpc	No. of Clusters	Light Matter f_{LM}	Dark Matter f_{DM}
2.5	6934	$0.587 \pm 0.004 - 0.004$	$0.459 \pm 0.155 - 0.077$
5	4281	$0.602 \pm 0.004 - 0.005$	$0.480 \pm 0.136 - 0.086$
7.5	2542	$0.625 \pm 0.006 - 0.006$	$0.614 \pm 0.205 - 0.139$

Using a smaller radius does increase the ellipticity which is to be expected if the main effect is to include more physically associated clusters which are more likely to lie along the major axis of the cluster, perhaps due to formation along an intervening filament. We find similar results for the light ellipticity. Our main results are unchanged by changing the cluster isolation criterion.

4.4. Misalignment Simulations

In order to interpret our results, we need to take into account possible misalignments during stacking. When we rotate clusters according to the distribution of the cluster members before stacking, we assume that the orientation of the light is correlated with the orientation of the mass. A result of f_{DM} consistent with 1 could indicate *either* a circular mass distribution *or* a random alignment between the light used for stacking and the dark matter. In the latter case, the circular result would be caused by the stacking of many clusters with different misalignments between the dark and the light matter.

In order to quantify this effect, we simulate many clusters all with the same input axis ratio f_{in} . The misalignment angles between the light and the dark matter for the simulated clusters are random, with a standard deviation σ_θ . For each value of f_{in} and σ_θ , we rotate and stack the clusters in the same way as for the SDSS data. Therefore, if σ_θ is large, the input ellipticity will be smeared out a great deal, and the output axis ratio f_{out} will be close to unity. If σ_θ is small the output ellipticity will be more similar (or in the case of zero misalignment, equal) to f_{in} .

Figure 6 shows the output dark matter axis ratio as a function of degree of misalignment σ_θ and the input axis ratio f_{in} . In order for the input ellipticity to be very elliptical ($f \rightarrow 0$), the

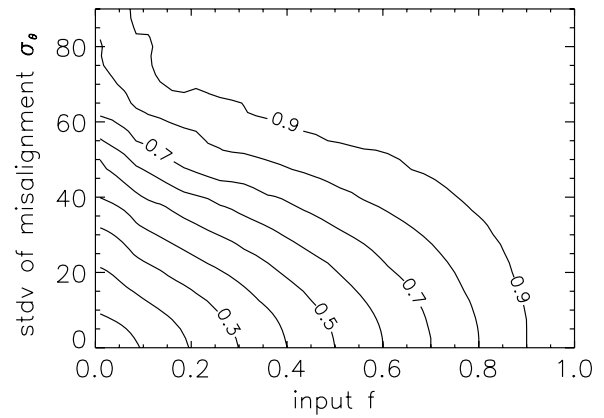


Figure 6. Contours show output axis ratios for simulated misalignments between the light and dark matter. Axes show the input axis ratio f_{in} and standard deviation σ_θ (in degrees) of the angle distribution of the simulated clusters.

misalignment between the dark and light matter must be $\sim 50^\circ$ for our dark matter f_{DM} of ~ 0.5 (see Table 2). We conclude that the misalignment angle must be less than $\sim 50^\circ$. If there is any misalignment between the light and the dark matter, the dark matter will be even more elliptical than the results shown in the table and can be read off Figure 6 for a given misalignment angle.

5. CONCLUSIONS AND DISCUSSION

We have used galaxy clusters from the catalogue of Koester et al. (2007a) and shear maps as used in Sheldon et al. (2004) to investigate the light and dark matter ellipticities of galaxy cluster halos. We rotate the selected clusters so that their major axes are aligned, and stack them according to the method which is described in Natarajan & Refregier (2000) for galaxy–galaxy lensing. This is the first time that this method has been applied to cluster lensing.

Through the pattern imprinted on the shear maps by intervening massive cluster halos, we have detected a dark matter ellipticity of these halos at a 99.6% level, with an axis ratio of $f_{\text{DM}} = 0.48^{+0.14}_{-0.09}$ from a joint χ^2 analysis for an NFW model, using 4281 clusters between $0.10 < z \leq 0.30$. We have corrected for dilution of the shear signal by cluster members left in the shear galaxy catalogues but have masked out the central areas where this correction factor grows too large.

The light matter distribution of the clusters, as traced by the number density of individual cluster members, is also clearly elliptical, with a joint axis ratio $f_{\text{LM}} = 0.60^{+0.004}_{-0.005}$ for the NFW model. Using the shear catalogue alone gives very similar results to using the shear catalogue concatenated with the cluster member catalogue, which means that we are essentially comparing like with like when comparing dark and light map ellipticities. This is because both the light matter (shear catalogue) and the dark matter have been stacked in the same way.

We find that the ellipticity of the dark matter distribution is consistent with the ellipticity of the galaxy number density distribution. Our result is limited by the uncertainty in the ellipticity of the dark matter distribution. The results for the NFW and SIE agree within the errors, but any differences could be attributed to a changing ellipticity with radius. We have not attempted to measure this effect since the uncertainties are too large.

Shear maps from neighboring clusters will influence each other, making the pattern more elliptical or less, depending on the redshift of the neighbors. In order to reduce this effect as much as possible, we use only the cluster with the highest number of members (N_{gals}^{r200}) when two (or more) clusters are closer together than $5 h^{-1}$ Mpc, as seen on the sky. We find that increasing or decreasing the minimum distance to a close neighbor by 50% does not significantly affect our main results.

We have also simulated the effect that a possible misalignment between the light and dark matter could have, and concluded that, according to our results, the light and dark matter must be misaligned by less than $\sim 50^\circ$.

Our measurement is very insensitive to overall calibration biases in shear measurements, since these are degenerate with cluster mass, rather than cluster ellipticity. It is unlikely that biases in shear measurement would vary with an angle around the cluster: residual PSF anisotropies would be oriented at random with respect to the cluster major axis and would cancel out on stacking; the cluster member light may leak into the postage stamps used to measure shears of background galaxies, but we remove the central region where the number of confirmed cluster members is significant.

Possibly the biggest potential systematic is intrinsic alignment of cluster members pointing at the cluster center (Ciotti & Dutta 1994; Kuhlen et al. 2007; Pereira et al. 2008; Knebe et al. 2008; Faltenbacher et al. 2008) which would be a problem for us, because we have not made a significant attempt to remove cluster members from our analysis and our background catalogue is not particularly deep. A thorough assessment of this effect is beyond the scope of the current work. To first order, this would make our observed shear maps less elliptical since the contamination by cluster members is greatest along the cluster major axis, and thus the strong gravitational shears expected along this axis will be partially canceled out by the cluster members which have the opposite ellipticity since they tend to point at the cluster center. However, a full assessment of this effect would also have to take into account the variation in intrinsic alignment with respect to the cluster major axis, which appears to be more complicated (Kuhlen et al. 2007) and possibly weakens the degree of cancellation preferentially along the cluster major axis.

In Hopkins et al. (2005), the authors use a large-scale, high-resolution N -body simulation to predict cluster ellipticities and alignments in a Λ cold dark matter (Λ CDM) universe. They find an ellipticity

$$\langle \epsilon \rangle = 1 - \langle f \rangle = 0.33 + 0.05z \quad (20)$$

for the redshift range $0 < z < 3$. This redshift evolution is negligible for the redshift range considered here, and due to the large uncertainties we do not try to detect any trends with redshift. For a redshift in the middle of the redshift range of our cluster sample ($z = 0.2$), this formula yields an axis ratio of $f = 0.66$ which is in good agreement with our result of $f_{\text{DM}} = 0.48^{+0.14}_{-0.09}$.

Ho et al. (2006) have used numerical simulations of cluster formation with the aim of investigating the possibility of using cluster ellipticities as a cosmological probe. They find that the mean ellipticity of high-mass clusters is approximated by

$$\bar{e}(z) = 0.245 \left[1 - 0.256 \frac{\sigma_8(z)}{0.9} + 0.00246 \frac{\Omega_m}{0.3} \right]. \quad (21)$$

Using $\sigma_8(z) = 0.8$ and $\Omega_m = 0.3$, this gives an ellipticity of $e \sim 0.2$, or $f \sim 0.8$. This result is more circular than our main

result. However, to make a proper comparison of our result with theory, it would be necessary to make a theoretical prediction that takes into account our observation method, especially the overlaps in the shear field due to close neighbors and the impact of selecting the most isolated clusters.

Hoekstra et al. (2004) report on a first weak-lensing detection of the flattening of galaxy dark matter halos, using data from the Red-Sequence Cluster Survey. They find an average galaxy dark matter halo ellipticity of $\langle \epsilon \rangle = 0.33^{+0.07}_{-0.09}$. They also find a detection that dark matter halos are rounder than the light map. In a later work, Mandelbaum et al. (2006) did not find a definite detection of this effect in the larger SDSS data set. However, Parker et al. (2007), measuring the ratio of tangential shear in regions close to the semiminor versus that close to the semimajor axes of the lens, find some evidence of a halo ellipticity of ~ 0.3 using early data from the CFHTLS. Mandelbaum et al. (2006) commented that the stronger signal in clusters of galaxies means that there is more chance of making a detection of ellipticity in this higher mass data set. Therefore, we have confirmed the detection of dark matter halo ellipticity, extending the measurement to cluster scales. We find no evidence for different ellipticities for the light and dark matter distribution on cluster scales.

Mandelbaum et al. (2006) focus on measuring the ratio of (dark matter) halo ellipticity to galaxy (light) ellipticity ϵ_h/ϵ_g , where $\epsilon = (a^2 - b^2)/(a^2 + b^2)$. They find $\epsilon_h/\epsilon_g = 0.60 \pm 0.38$ (68% confidence) for elliptical galaxies, which is most comparable with our result of $f_{\text{DM}}/f_{\text{LM}} = 0.91^{+0.19}_{-0.25}$ (68% confidence), where $f = b/a$. Repeating our calculation using the different ellipticity parameters, we find $\epsilon_h/\epsilon_g = 1.37^{+0.35}_{-0.26}$. It is expected that our value is greater than unity, since we find that the dark matter is more elliptical (lower axis ratio) than the light matter. However, it is not significantly larger. The result of Mandelbaum et al. (2006) is the opposite side of unity, but the difference is not significant and we note that our result is for clusters and that of Mandelbaum et al. (2006) is for galaxies.

The anisotropy of the lensing signal around individual galaxies, if definitely detected, has been said to pose a serious problem for alternative theories of gravity (Hoekstra et al. 2004). For galaxy clusters it is more complicated, as the dominant source of baryons is the intracluster gas. Lensing by clusters has been found to pose a problem for Modified Newtonian Dynamics (MOND), as there seems to be a need to include a dark matter component (Sanders 2003; Takahashi & Chiba 2007).

Because the gas—the dominant baryonic component of clusters—is collisional, we can suppose that on cluster scales it will be less elliptical than the light. We may end up concluding that either (1) the gas distribution is elliptical (which we would not expect) or (2) our result is inconsistent with MOND. However, further study and simulations of this is clearly needed.

We thank Erin Sheldon and Benjamin Koester for providing us with galaxy catalogues and for very helpful comments and suggestions. We also thank the anonymous referee for many helpful comments and suggestions. We also thank Timothy McKay, Alexandre Refregier, Jochen Weller, Håkon Dahle, Andreas Jaunsen, Margrethe Wold, Shirley Ho, Eduardo Cypriano, Laurie Shaw, Richard Cook, David Sutton, Andrey Kravtsov, Øystein Elgarøy, Morad Amarzguoui, Terje Fredvik, and Stein Vidar Hagfors Haugan for helpful discussions. A.K.D.E. acknowledges support from the Research Council of Norway, Project No. 162830. S.L.B. acknowledges support from the Royal Society in the form of a University Research Fellowship.

REFERENCES

- Albrecht, A., et al. 2006, arXiv:astro-ph/0609591
- Allgood, B., Flores, R. A., Primack, J. R., Kravtsov, A. V., Wechsler, R. H., Faltenbacher, A., & Bullock, J. S. 2006, *MNRAS*, **367**, 1781
- Bartelmann, M. 1996, *A&A*, **313**, 697
- Bernstein, G. M., & Jarvis, M. 2002, *AJ*, **123**, 583
- Bode, P., Ostriker, J. P., Weller, J., & Shaw, L. 2007, *ApJ*, **663**, 139
- Bridle, S., & Abdalla, F. B. 2007, *ApJ*, **655**, L1
- Bridle, S., Kneib, J.-P., Bardeau, S., & Gull, S. 2002, in *The Shapes of Galaxies and Their Dark Matter Halos*, Proceedings of the Yale Cosmology Workshop, New Haven, Connecticut, USA, 28–30 May 2001, ed. P. Natarajan (Singapore: World Scientific), 38 (ISBN 9810248482)
- Buote, D. A., & Xu, G. 1997, *MNRAS*, **284**, 439
- Ciotti, L., & Dutta, S. N. 1994, *MNRAS*, **270**, 390
- Clowe, D., Bradač, M., Gonzalez, A. H., Markevitch, M., Randall, S. W., Jones, C., & Zaritsky, D. 2006, *ApJ*, **648**, L109
- Cypriano, E. S., Sodr , L. J., Kneib, J.-P., & Campusano, L. E. 2004, *ApJ*, **613**, 95
- de Theije, P. A. M., Katgert, P., & van Kampen, E. 1995, *MNRAS*, **273**, 30
- Evrard, A. E., Mohr, J. J., Fabricant, D. G., & Geller, M. J. 1993, *ApJ*, **419**, L9
- Faltenbacher, A., Jing, Y. P., Li, C., Mao, S., Mo, H. J., Pasquali, A., & van den Bosch, F. C. 2008, *ApJ*, **675**, 146
- Floor, S. N., Melott, A. L., Miller, C. J., & Bryan, G. L. 2003, *ApJ*, **591**, 741
- Flores, R. A., Allgood, B., Kravtsov, A. V., Primack, J. R., Buote, D. A., & Bullock, J. S. 2007, *MNRAS*, **377**, 883
- Hirata, C., & Seljak, U. 2003, *MNRAS*, **343**, 459
- Ho, S., Bahcall, N., & Bode, P. 2006, *ApJ*, **647**, 8
- Ho, S., & White, M. 2004, *ApJ*, **607**, 40
- Hoekstra, H., Yee, H. K. C., & Gladders, M. D. 2004, *ApJ*, **606**, 67
- Hopkins, P. F., Bahcall, N. A., & Bode, P. 2005, *ApJ*, **618**, 1
- Jing, Y. P., & Suto, Y. 2002, *ApJ*, **574**, 538
- Johnston, D. E., et al. 2007, arXiv:0709.1159
- Kassiola, A., & Kovner, I. 1993, *ApJ*, **417**, 450
- Kasun, S. F., & Evrard, A. E. 2005, *ApJ*, **629**, 781
- Keeton, C. R. 2001, arXiv:astro-ph/0102341
- Knebe, A., Draganova, N., Power, C., Yepes, G., Hoffman, Y., Gottl ber, S., & Gibson, B. K. 2008, *MNRAS*, **386**, L52
- Koester, B. P., et al. 2007a, *ApJ*, **660**, 239
- Koester, B. P., et al. 2007b, *ApJ*, **660**, 221
- Kormann, R., Schneider, P., & Bartelmann, M. 1994, *A&A*, **284**, 285
- Kuhlen, M., Diemand, J., & Madau, P. 2007, *ApJ*, **671**, 1135
- Mandelbaum, R., Hirata, C. M., Broderick, T., Seljak, U., & Brinkmann, J. 2006, *MNRAS*, **370**, 1008
- Natarajan, P., & Refregier, A. 2000, *ApJ*, **538**, L113
- Navarro, J. F., Frenk, C. S., & White, S. D. M. 1997, *ApJ*, **490**, 493
- Parker, L. C., Hoekstra, H., Hudson, M. J., van Waerbake, L., & Mellier, Y. 2007, *ApJ*, **669**, 21
- Pereira, M. J., Bryan, G. L., & Gill, S. P. D. 2008, *ApJ*, **672**, 825
- Plionis, M., Barrow, J. D., & Frenk, C. S. 1991, *MNRAS*, **249**, 662
- Rahman, N., Krywult, J., Motl, P. M., Flin, P., & Shandarin, S. F. 2006, *MNRAS*, **367**, 838
- Rahman, N., Shandarin, S. F., Motl, P. M., & Melott, A. L. 2004, arXiv:astro-ph/0405097
- Rhee, G. F. R. N., van Haarlem, M. P., & Katgert, P. 1991, *A&AS*, **91**, 513
- Sanders, R. H. 2003, *MNRAS*, **342**, 901
- Schramm, T. 1990, *A&A*, **231**, 19
- Scranton, R., et al. 2002, *ApJ*, **579**, 48
- Seljak, U. 2000, *MNRAS*, **318**, 203
- Sheldon, E. S., et al. 2004, *AJ*, **127**, 2544
- Sheldon, E. S., et al. 2007a, arXiv:0709.1162
- Sheldon, E. S., et al. 2007b, arXiv:0709.1153
- Sheldon, E. S., et al. 2001, *ApJ*, **554**, 881
- Splinter, R. J., Melott, A. L., Linn, A. M., Buck, C., & Tinker, J. 1997, *ApJ*, **479**, 632
- Strazzullo, V., Paolillo, M., Longo, G., Puddu, E., Djorgovski, S. G., De Carvalho, R. R., & Gal, R. R. 2005, *MNRAS*, **359**, 191
- Suwa, T., Habe, A., Yoshikawa, K., & Okamoto, T. 2003, *ApJ*, **588**, 7
- Takahashi, R., & Chiba, T. 2007, *ApJ*, **671**, 45
- Wang, Y., Yang, X., Mo, H. J., Li, C., van den Bosch, F. C., Fan, Z., & Chen, X. 2008, *MNRAS*, **385**, 1511
- West, M. J., & Bothun, G. D. 1990, *ApJ*, **350**, 36
- West, M. J., Dekel, A., & Oemler, A. J. 1989, *ApJ*, **336**, 46
- Wright, C. O., & Brainerd, T. G. 2000, *ApJ*, **534**, 34
- York, D. G., et al. 2000, *AJ*, **120**, 1579

Paper II

Shaw, L., Evans, A. K. D.; Bridle, S.,
Predictions of dark matter halo ellipticities measured by lensing,
To be submitted to Astrophysical Journal (Ap.J.)

PREDICTIONS OF DARK MATTER HALO ELLIPTICITIES MEASURED BY LENSING

ANNA KATHINKA DALLAND EVANS¹, LAURIE SHAW², SARAH BRIDLE³

Draft version April 29, 2009

ABSTRACT

We study the ellipticity of galaxy cluster dark matter halos using N-body simulations. Unlike previous work we simulate the expected ellipticity that would be observed using gravitational lensing. Our analysis is tuned to match the recent detection of cluster halo ellipticity by Evans & Bridle (2008), and we find results which are very consistent with those observed. We investigate the ellipticity measured using lensing, as compared to the more conventional measure of ellipticity that is applied to simulations. We find good agreement, although the lensing ellipticity appears to show some dependence on the isolation criteria applied.

Subject headings: cosmology: dark matter — cosmology: galaxy clusters — cosmology: large-scale structure of universe — cosmology: simulations — galaxies: clusters: general galaxies: halos —

1. INTRODUCTION

Galaxy clusters are gravitationally bound aggregations of galaxies, hot gas and dark matter ranging in richness from a few tens to several thousands of galaxy members. Methods utilizing clusters to probe the large-scale structure in the universe have proliferated in recent years. For example, the number of clusters has a useful dependence on cosmological model (Peacock et al. 2006; Albrecht et al. 2006). Since clusters trace the highest peaks in the matter distribution in the universe, their number density as a function of mass and redshift can be exploited to investigate the growth rate of structure, and thus the dark energy equation of state (see e.g. Holder et al. 2001; Levine et al. 2002).

Weak gravitational lensing can be used to infer the distribution of mass in clusters (e.g. Clowe et al. 2006, 2004; Hoekstra et al. 2004; Marshall et al. 2002; Bridle et al. 1998). The three-dimensional mass distribution in halos is complex due to differences in substructure and merger histories. To simplify comparisons with simulations, one often just considers the radially-averaged mass profile. This can be done on a per cluster basis (e.g. Pedersen & Dahle 2007; Hoekstra 2007), however the mass estimates of individual clusters are typically very noisy due to the small number of lensed galaxies. The precision of these measurements can be greatly improved by stacking clusters to obtain a mean mass profile (Johnston et al. 2007; Mandelbaum et al. 2008; Dahle et al. 2003; Sheldon et al. 2001). The general conclusion is that cluster profiles largely agree with the Navarro-Frenk-White (NFW; Navarro et al. 1997) profile predicted by N-body simulations.

Internal properties of clusters themselves have also been used to place constraints on cosmology. Richstone et al. (1992) explores how the presence of substructure in clusters, as a measure for the formation epoch of the cluster, can be used to constrain the density parameter of the universe (see also Evrard et al. 1993; Mohr et al. 1995). In

a universe with a low matter density, clusters form earlier and are hence expected to be more relaxed today. Several studies also look for patterns in the cluster-to-cluster alignment (Kasun & Evrard 2005; Hopkins et al. 2005) as a means to investigate the idea of hierarchical clustering, wherein clusters would be expected to be aligned with their neighbours due to matter having converged in dense regions along filamentary structures (Plionis & Basilakos 2002; West et al. 1995).

A property of clusters that has perhaps been studied in less detail is their ellipticity. There have been some observational studies of the ellipticities of galaxy clusters in recent years (Wang et al. 2007; Cypriano et al. 2004; Evans & Bridle 2008), but most of the work has been theoretical, using large-scale simulations of structure formation (e.g. Jing 2002; Floor et al. 2003). In general, cosmological N-body simulations predict that gravitation causes matter on cluster scales to collapse into aspherical shapes (Kasun & Evrard 2005), in particular triaxial prolate ellipsoids (Dubinski & Carlberg 1991; Warren et al. 1992). Hopkins et al. (2005) and Paz et al. (2006) also measure the two-dimensional projected cluster ellipticity in their simulations, thus enabling a direct comparison with observations via gravitational lensing.

Studies find that ellipticities of clusters are interesting because of their implications for differentiating between cosmological models (Suwa et al. 2003; Flores et al. 2005), their dependence on cosmological parameters (Ho et al. 2006; Rahman et al. 2004; Splinter et al. 1997) and their effects on estimates of cluster density profiles (Meneghetti et al. 2007).

Evans & Bridle (2008) reported a detection of dark matter ellipticity using the combined weak lensing shear signal from about 4000 clusters from the Sloan Digital Sky Survey (SDSS) using the cluster catalogue of Koester et al. (2007). In the current paper, our aim is to compare those observational results to results from applying the same weak lensing method to clusters extracted from a large-scale N-body simulation. In Sec. 2.1 we describe these simulations. In the rest of Sec. 2, we briefly review the method of Evans & Bridle (2008), highlighting the modifications to the method needed in order to facilitate analysis of the simulated data set. Our results are presented

¹ Institute of Theoretical Astrophysics, University of Oslo, Box 1029, 0315 Oslo, Norway.

² Department of Physics, McGill University, 3600 rue University, Montreal, QC, Canada

³ Department of Physics and Astronomy, University College London, Gower Street, London, WC1E 6BT, UK.

in Sec. 3, and a discussion of the results follows in Sec. 4.

2. ANALYSING SIMULATED DATA

Evans & Bridle (2008) measured the ellipticities of cluster dark matter halos using the tangential shear signal resulting from weak gravitational lensing of background galaxies by foreground clusters. To increase the signal-to-noise they combined the measurements from many clusters of galaxies by stacking the shear maps according to the cluster center, while retaining any ellipticity information by rotating the clusters before stacking so that the major axes of the light were aligned. The ellipticity of the dark matter halo was then estimated by fitting an elliptical mass density profile to the stacked shear map. The ellipticity of the cluster member distribution was estimated by fitting an elliptical profile to the stacked galaxy distribution.

The main purpose of the present paper is to apply this same technique on simulated clusters. Earlier work on simulated cluster ellipticities (Hopkins et al. 2005; Flores et al. 2005; Ho et al. 2006) has used the distribution of simulation particles in halos to measure their ellipticity. However the only way to *observe* the halo ellipticity is from gravitational lensing, which measures the projected mass along the line of sight. Ellipticities measured using gravitational lensing are therefore potentially increased by the inclusion of physically close neighbors and filaments. However they may also be decreased by the contribution from coincidental overlaps by physically separated objects projected along the line of sight. Until now, such effects have not been accounted for in the simulations.

The convergence κ is defined in General Relativity by rescaling the projected mass per unit area in the lens, and is given in terms of the projected surface mass density of the lens, Σ , as:

$$\kappa(\theta) = \frac{\Sigma(\theta)}{\Sigma_{\text{crit}}}, \quad (1)$$

where θ is an axis vector on the plane of the sky and Σ_{crit} is the critical surface density of the lens, given by

$$\Sigma_{\text{crit}} = \frac{c^2}{4\pi G} \frac{D_s}{D_d D_{ds}}. \quad (2)$$

In this expression, D_s , D_d and D_{ds} are, respectively, the angular diameter distances between observer and source, observer and lens (deflector) and between lens and source.

2.1. Description of the simulations

To create our sample of convergence (or κ) maps, we begin with the output of a large ($N = 1024^3$ particles) cosmological dark matter simulation. The cosmology was chosen to be consistent with that measured from the 3rd-year WMAP data combined with large-scale structure observations (Spergel et al. 2007), namely a spatially flat LCDM model with parameters: baryon density $\Omega_b = 0.044$; total matter density $\Omega_m = 0.26$; cosmological constant $\Omega_\Lambda = 0.74$; linear matter power spectrum amplitude $\sigma_8 = 0.77$; primordial scalar spectral index $n_s = 0.95$; and Hubble constant $H_0 = 72 \text{ km s}^{-1} \text{ Mpc}^{-1}$ (i.e. $h = 0.72 = H_0/100 \text{ km s}^{-1} \text{ Mpc}^{-1}$). The simulated volume is a periodic cube of size $L = 320 h^{-1} \text{ Mpc}$; the particle mass $m_p = 2.2 \times 10^9 h^{-1} M_\odot$, and the cubic spline softening length $\epsilon = 3.2 h^{-1} \text{ kpc}$.

The matter distribution in a light cone covering one octant of the sky ($\approx 5200 \text{ deg}^2$) extending to $z = 0.5$ was

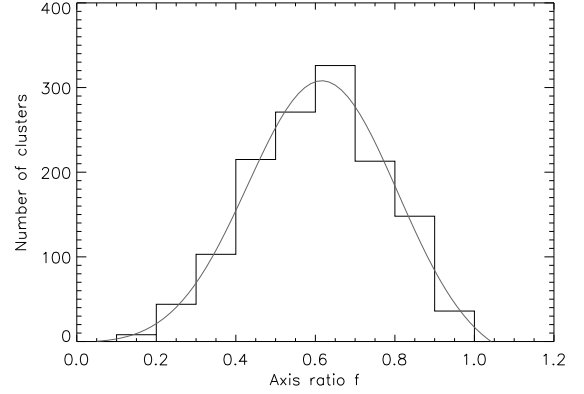


FIG. 1.— Histogram of the projected minor to major axis ratio f_p for our sample of simulated halos. The sample was chosen using our default parameters, such that no halo had a larger neighbor closer than $5h^{-1} \text{ Mpc}$, and with a threshold mass of $6 \times 10^{13} h^{-1} M_\odot$. Note that f_p in this particular plot was calculated *without* applying a central mask.

saved in 315 time slices. Dark matter halos were identified using the Friends-of-Friends (FoF) algorithm with a co-moving linking length parameter $b = 0.2$. We set the minimum halo mass to 50 particles ($M_{\text{FoF}} < 1.09 \times 10^{11} M_\odot$); all particles in halos with M_{FoF} less than this are discarded. For the remainder, a 3D mesh (with cell side-length $4\epsilon = 17.6 h^{-1} \text{ kpc}$) is placed around each halo, onto which we interpolate the halo particles. By summing up the mass in each mesh cell along one direction, we produce a 2D ‘postage-stamp’ projected mass-map for each cluster. Note that each postage-stamp is produced having rotated the 3D mesh around the cluster so that one face lies tangential to the plane of the lightcone ‘sky’. Following this step, we are left with a library containing the angular positions, redshifts and mass planes for the one million lightcone halos above our mass threshold, encompassing the redshift range $0 < z < 0.5$.

Convergence maps are produced by projecting down the lightcone, summing up the contribution of all the clusters along the line of sight of each map pixel. The value of each map pixel is given by

$$\kappa(\theta, \phi) = \sum_i g(z_i) \Sigma_i(z_i), \quad (3)$$

where the sum is over each cluster i that intersects the line of sight of the pixel (with angular co-ordinates θ, ϕ), z_i is the redshift of the cluster and Σ_i is the projected mass density of the cluster at this position. The factor $g(z_i)$ is given by

$$g(z_i) = \frac{4\pi G}{c^2} \int_0^{z_s} n(z'_s) \frac{D_A(z_i)(D_A(z'_s) - D_A(z_i))}{D_A(z'_s)} dz'_s, \quad (4)$$

where $n(z_s)$ is the redshift distribution of background (lensed) galaxies (normalised such that the integral over $0 < z < 0.5$ is unity), and $D_A(z)$ is the angular diameter distance at redshift z . In this work we use the same $n(z_s)$ as in Evans & Bridle (2008), estimated from Fig. 3 and Eq. 8 in Sheldon et al. (2001), with $z_c = 0.22$.

We produce a base sample of 28 $10 \times 10 \text{ deg}$ convergence maps encompassing the full mass and redshift range of our halo catalogue, with a pixel size of 0.25 arcminutes. Each map has an accompanying halo catalogue giving R_{200} (the radius in which the spherically-average density is $200\rho_{\text{crit}}$),

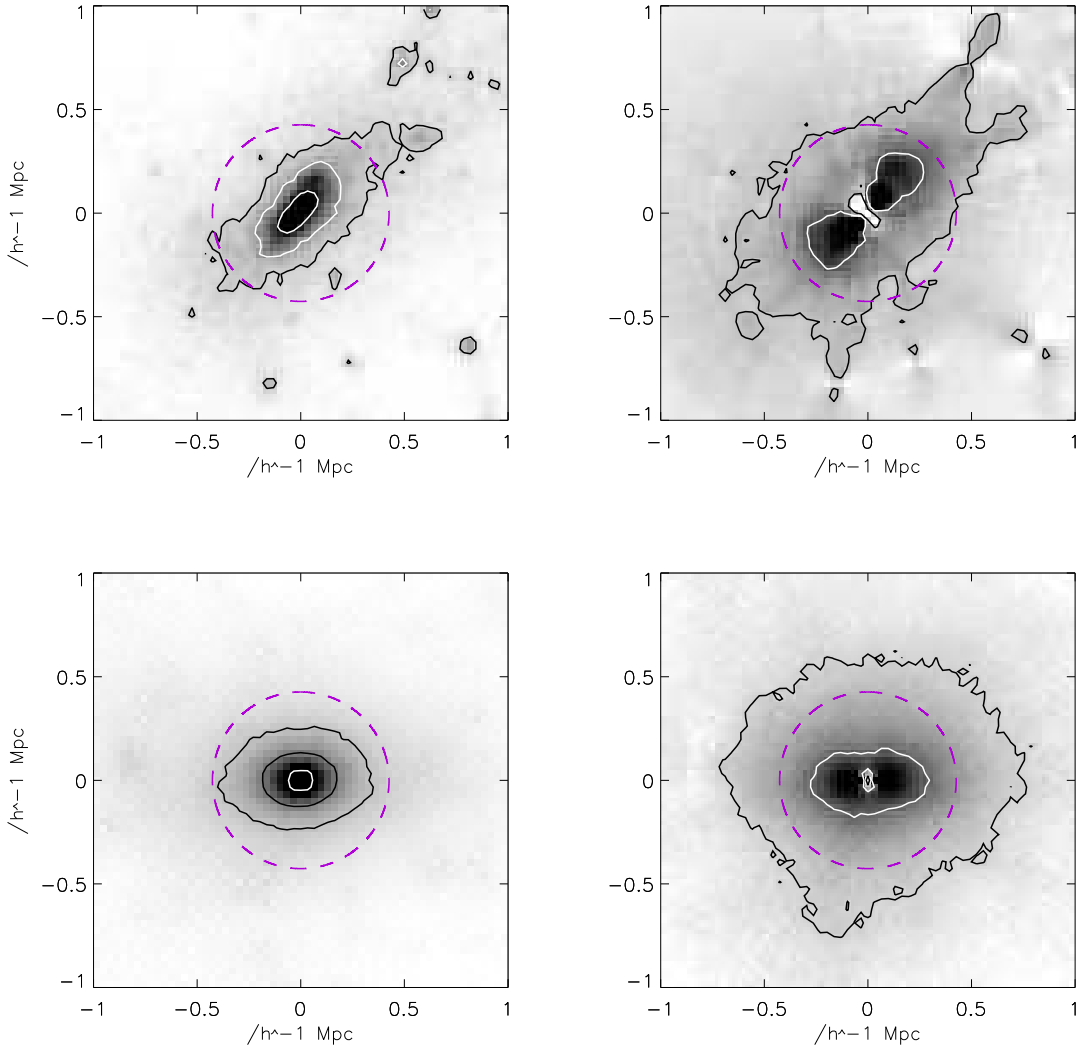


FIG. 2.— Illustrating a typical individual cluster (top row) as well as a stacked cluster (bottom row), in which the clusters have been rotated to have their major axes along the x -axis. The left hand panels show the convergence maps, and the right hand panels show the tangential shear. Contours for the convergence maps are at 10, 20 and 50 % of the maximum individual and stacked convergence values, while contours for the shear maps are at 20 and 50% of the maximum individual and stacked shear values. The individual cluster (top panels) has $f_p = 0.6$ and a rotation angle of ~ 35 deg anticlockwise to the positive horizontal axis, as calculated using two-dimensional quadrupole moments of particles isolated in three-dimensions around the cluster. The stacked cluster contains ~ 200 clusters in the redshift range $0.15 < z < 0.20$. The dashed circle shows the location of the mask.

M_{200} and the redshift of every cluster in the map. We also include in this catalogue an estimate for the projected ellipticity and orientation of each cluster. This is calculated by measuring the 2D moment of inertia tensor from the individual mass-planes for each cluster, including the contribution of all matter within 3Mpc (comoving) of the cluster potential minimum. Solving for the eigenvectors gives the minor to major principle axis ratio for each halo. Before calculating the axis ratio, a central mask of radius $0.5h^{-1}$ Mpc was applied to the halos, see Sec. 2.4.

The orientation of a cluster is defined as the angle between the principle axis and the line of constant declination at the angular position of the cluster in the map. This information is used in the following section to stack clusters so that their principle axes are aligned before measuring ellipticity from their combined shear profiles.

In Fig. 1 we show a histogram of the f_p axis ratio calculated from quadrupole moments of the particles in the

simulation, from all clusters above the mass threshold of $6 \times 10^{13} h^{-1} M_\odot$ that are accepted for the main analysis (see Section 2.2). We fit a Gaussian to the histogram, and in Fig. 1 show the best fit plot which is centred at $f = 0.6$ and has a standard deviation of 0.2. Note that, in order to facilitate comparisons with other simulation studies, the axis ratios in Fig. 1 are calculated without applying the mask, whereas in the rest of this paper the mask has been applied to the simulated halos.

One advantage of our map-making procedure is that it is straightforward to reproduce maps that contain only the contribution of halos that lie within a particular mass or redshift range. In order to assess the impact of surrounding and intervening structure on the weak-lensing estimates of cluster ellipticity, we also have produced a sub-sample of 48 maps (at the same resolution), each containing only a single cluster. These single cluster κ maps are discussed further in Section 3.1.

2.2. From projected mass maps to shear maps

Our aim is to study the shear maps made from our simulated convergence maps to quantify the accuracy of measurements of cluster ellipticity, both on a cluster-by-cluster basis and via stacking. The first step is thus to convolve the convergence maps to make corresponding shear maps. The shear pattern can be expressed as a convolution in terms of the convergence κ . We use

$$\gamma(\theta) = \frac{1}{\pi} \int \mathcal{D}(\theta - \theta') \kappa(\theta') d^2\theta', \quad (5)$$

$$\mathcal{D}(\theta) = \frac{\theta_2^2 - \theta_1^2 - 2i\theta_1\theta_2}{|\theta|^4} \quad (6)$$

(e.g. Bridle et al. 1998) where θ_1 and θ_2 are components of θ (axis vectors on the sky).

We use all halos with a FoF mass above $6 \times 10^{13} h^{-1} M_\odot$, which corresponds to the minimum number of galaxies used in Evans & Bridle (2008), which was 10 galaxies within R_{200} . We restrict the redshift range of our halo sample to $0.1 < z < 0.3$, as in Evans & Bridle (2008). Due to the redshift-dependant galaxy number density distribution we have adopted, ($n(z_s)$, see Sec. 2.1) higher redshift clusters have very small shear signals. We further divide this redshift range into four bins, each of width 0.05 in z . We did not use clusters that were too close to the projected mass map edge, using the requirement that the distance from a cluster centre to the map edge be greater than $12 h^{-1} \text{Mpc}$ (at the redshift of the cluster).

2.3. Isolating, stacking and rotating the shear maps

Clusters that are close to each other on the sky require careful consideration. As the shear field of a cluster is contaminated by neighbouring clusters, a study interested in making a raw measurement of cluster ellipticities must attempt to find clusters which are isolated on the sky. An alternative option would be to include all clusters; The stacked shear map would then be a two-dimensional galaxy shear - cluster position two point correlation function. Extraction of the cluster ellipticities would then require careful modelling including the two-dimensional two point function of cluster positions, taking into account the tendency of cluster neighbors to sit preferentially along the cluster major axis, for physically close clusters. We choose the first option here, but show results for different neighbor distance criteria.

We follow the isolation criteria of Evans & Bridle (2008) who required that there be no larger neighbouring clusters within a projected physical distance of $5 h^{-1} \text{Mpc}$ from any one cluster. Procedurally, we work through all the clusters from low to high redshift, and for each we calculate the angular separation of the nearest cluster, considering all clusters from all redshifts. We compare this to our physical cut-off distance at the redshift of the cluster in question. If the separation between two clusters is below $5 h^{-1} \text{Mpc}$ then we remove the least massive from our analysis. Evans & Bridle (2008) defined cluster ‘size’ using the richness measured by the number of cluster members within a circular aperture of radius R_{200} . In the current paper, we use the same isolation distance but compare size as measured by the halo mass M_{200} measured from the simulations. This process resulted in a list of 1364 clusters. We also investigate the effect on our results by decreasing or increasing this radius by 50%.

We extract a postage stamp of shears in a region $10 \times 10 h^{-1} \text{Mpc}$ around each cluster centre. This matches the size used in Evans & Bridle (2008) which was motivated by reducing the contamination from neighboring large-scale structure.

The halo ellipticity constraint from individual clusters is usually very noisy and therefore more useful constraints can be obtained by stacking many clusters on top of each other. To retain the ellipticity information we must rotate the clusters before stacking so that the features of interest are aligned (as suggested by Natarajan & Refregier 2000). In this way, a single ellipticity for a typical cluster can be obtained for the cluster sample. We rotate the clusters according to the rotation angle calculated from particles in the simulation, as described in Section 2.1. We then calculate the mean of the tangential shear in each pixel in the stacked shear map.

Fig. 2 illustrates projected convergence (left panels) and tangential shear (right panels) for a single cluster (upper row) and a stack of ~ 200 clusters (lower row). The upper panels show that the single cluster is aligned at an angle with respect to the horizontal axis (~ 35 deg anticlockwise for this particular cluster), whereas in the lower panel all clusters in the stack have been rotated to align with the horizontal axis in order to retain any ellipticity information when stacking. When running our main analysis we apply a mask at the centre of the cluster, see Section 2.4, which completely removes this central region. The dashed circle shows the location of the mask.

2.4. Modelling

To model the cluster mass distribution, we use the Navarro-Frenk-White (NFW) model. We fix the NFW concentration parameter to 5 for the analysis presented here. The shear for an elliptical mass distribution is calculated using the equations in Keeton (2001) which are derived from those in Schramm (1990). A shear map using these equations is illustrated in Fig. 1 of Bridle & Abdalla (2007).

To estimate the ellipticity of the dark matter distribution we calculate probability as a function of (projected) cluster minor-to-major axis ratio f_l and cluster mass M_{200} . We calculate the probability of the predicted (or model) shear using the χ^2 statistic and a Jeffrey’s prior on the mass, as appropriate when the order of magnitude of the mass is unknown. Because the simulated shear maps have no noise, we set the uncertainty in the χ^2 -calculation to an arbitrary value that still gives a well-defined peak in the probability distribution. We marginalize over the cluster mass to obtain the probability as a function of the axis ratio f_l .

We make stacked shear maps in four redshift bins between $0.1 < z < 0.3$ and fit each as a function of mass and axis ratio, marginalising over mass to obtain the one dimensional probability as a function of f_l . A single result for f_l is then obtained by multiplying the probabilities for all four redshift bins. In using this procedure we implicitly assume that f_l is identical in all redshift bins but that the others parameters can vary.

We use the angular diameter distance at the center of each redshift bin to calculate for each cluster the size of the postage stamp, the size of the mask and the minimum closest distance to a neighbouring cluster.

When using shear catalogues without spectroscopic red-

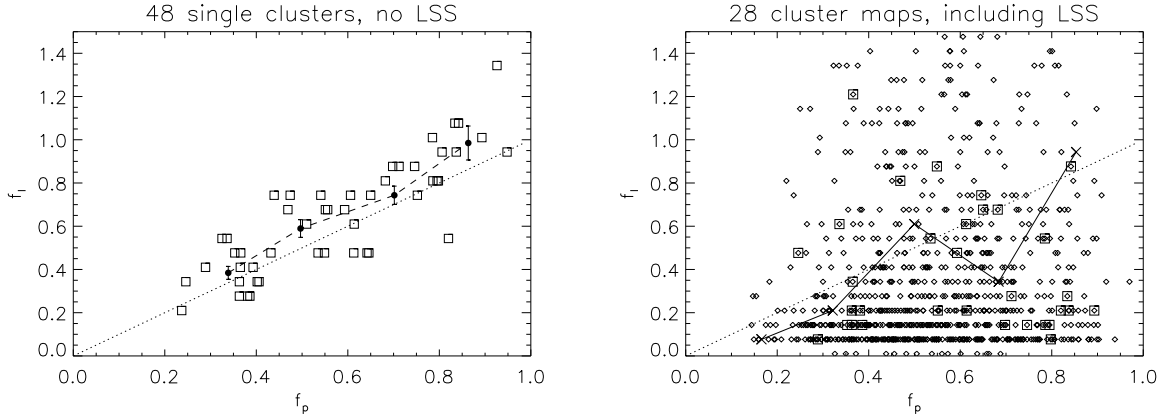


FIG. 3.— The squares and diamonds in the two panels show the axis ratio measured using lensing (f_l) versus the conventional method for measuring cluster ellipticities from simulations (f_p). There is one point per cluster. The shear maps used for the analysis in the left hand panel are the 48 maps each containing only a single cluster i.e. no surrounding large-scale structure. The right panel contains all individual clusters (after neighbour removal) from the 28 original projected mass maps including surrounding large-scale structure. Clusters that are marked with squares in the left panel are also marked with squares in the right panel. The dotted line in each panel shows the line $f_l = f_p$. Left panel: square symbols show a good match between f_p and f_l . Number of clusters in each f_p bin: 4, 20, 13 and 11, giving 48 in total. Filled circles joined by dashed line show the mean f_l from the individual cluster results (i.e. filled circles are mean of the square symbols in each f_p bin). Error bars on these points show the standard deviation of f_l values divided by $\sqrt{n_{\text{clust}}}$ in each f_p bin. Right panel: There is a large scatter in the individual analysis, showing that the surrounding structure affects our results even though we try to isolate the clusters using the close neighbour distances. We excluded from the right-hand panel the 520 clusters that resulted in $f_l > 2$. Crosses joined by a solid line show f_l obtained from stacking the respective individual clusters in five bins of f_p , versus the mean f_p value in each bin.

shift information, there will always be some degree of contamination of the shear catalogue by cluster members. This can to a large extent be corrected for *a posteriori* using a correction factor which increases towards the centre, but has a non-negligible uncertainty and therefore the central regions are best excluded from the lensing analysis. The central regions are also best avoided due to obscuration and contamination of the shear measurements by cluster members, and potential problems identifying the center on which to stack the shear maps. The central regions in Evans & Bridle (2008) were omitted using a circular mask with $r_{\text{mask}} = 0.5h^{-1}$ Mpc. In the present paper we have also applied the mask in order to mimic observational results.

3. RESULTS

We first measure cluster ellipticities from shear maps of individual clusters (i.e. omitting all foreground and background halos from the simulated maps). We compare the average of such ellipticities to the ellipticity measured from stacked shear maps. We calculate this as a function of the ellipticity calculated directly from the cluster particles in the simulation. We then investigate how the stacked ellipticity depends on the isolation criteria.

3.1. Results from individual clusters

We start by analysing shear maps containing signal purely from the cluster of interest. This is achieved by making a convergence map using only the particles identified to be in the cluster. This is performed for a subset of the whole cluster catalogue, using just the first three of the 28 fields, yielding 48 clusters. The squares in the left hand panel of Fig. 3 show the lensing axis ratios (f_l) found from each individual cluster, without stacking. This is plotted as a function of the axis ratio found from the quadrupole moments of the individual projected mass-maps of each cluster (f_p), as described in Section 2.1. We see that there is a good correlation between the two.

The scatter is expected because of the different effec-

tive radial weighting in a lensing analysis than in the quadrupole moments. By fitting an NFW profile we effectively measure weighted quadrupole moments in which the importance of the outer regions is reduced. The filled circles joined by a dashed line are the mean of the square shapes (f_l) in each f_p bin, plotted versus the mean of f_p in each bin. The error bars show the error on this mean, calculated by dividing the standard deviation of the points by the square root of the number of clusters in the bin. We can see that on average the two ellipticity estimation methods give consistent results within the errors.

We now produce lensing convergence maps for the whole field – including fore- and background structures along the line-of-sight – and convert them into shear maps. The shear map around a cluster will now contain contamination from surrounding structures. We now use all 28 fields available, in which 1364 clusters survive our mass, redshift and isolation criteria. The diamonds in the right-hand panel of Fig. 3 show the axis ratio estimated from each postage stamp around each individual cluster. We see that there is a huge scatter between the f_p calculated from the simulations and the f_l calculated from the lensing analysis. This scatter is due to the disturbing influence of the surrounding large-scale structure.

A large number (520) of clusters for the individual analysis shown in the right-hand panel of Fig. 3 resulted in $f_l > 2$. An axis ratio above unity means that the best-fit cluster is aligned along the y -axis, despite the fact that we have rotated the shear map so the major axis of the cluster particles lies along the x -axis. This is to be expected when there is significant uncorrelated neighboring structure that survives our isolation criteria. For example, clusters that appear close in projection, but which are at different redshifts.

There are also a large number of diamonds at $f_l \sim 0.2$. Surrounding structure predominantly along the horizontal axis will give a highly elliptical f_l . Structure that is physically associated with the cluster will tend to lie along this axis, possibly due to formation along a filament. This

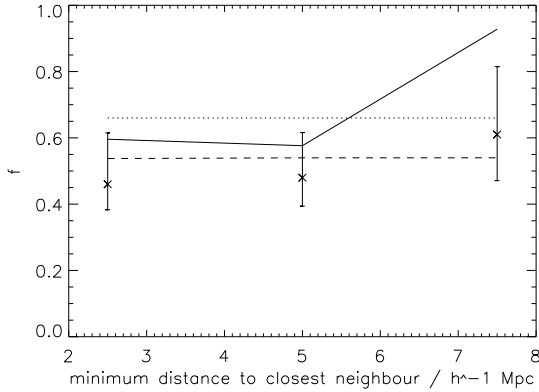


FIG. 4.— Stacked results for different minimum close neighbour distances. Crosses with error bars: Axis ratio f_{DM} combined from all redshift bins, reproduced from table 3 of Evans & Bridle (2008), as a function of minimum distance allowed to the closest neighbouring cluster. Number of clusters used in that analysis for each close neighbor distance (i.e. 2.5, 5 and $7h^{-1}$ Mpc): 6934, 4281, 2542. Solid line shows results f_l from lensing, combining results from all redshift bins. Number of clusters used for each value of the closest neighbour distance: 2193, 1364, 815. Dashed line shows the mean of all f_p from particles in the simulation. This is practically a constant since the calculations of f_p were independent of close neighbour distance. Dotted line shows results from Hopkins et al. (2005) in good agreement with our f_p -line (dashed).

structure is not included in the f_p -values.

The clusters in the left-hand panel of Fig. 3 are a subset of those in the right. In order to see the difference that the large-scale structure makes for a particular sample, we have identified the clusters in the sub-sample (individual points in the left panel) with a square symbol in the right panel.

In summary, Fig. 3 illustrates the fact that, although the simulations are noise-free, we still need to stack the clusters in order to obtain a reasonable result. If we stack enough clusters, the substructures in the surrounding structure will tend to cancel out.

3.2. Results from stacking clusters

The crosses connected by a solid line in the right panel of Fig. 3 shows the result of stacking the clusters five bins, each of width 0.2 in f_p . Resulting lensing axis ratios f_l are plotted against the mean f_p -value in each bin. We stacked the clusters in four bins of redshift within each f_p bin, and then combined them to obtain a single, one-dimensional marginalised probability function for f_l for each f_p bin. We see that there is broad agreement between the stacked lensing axis ratios and the conventional method, although there is some noise.

These figures suggest that the cluster ellipticity as measured from particles in the simulations is a reasonable proxy for the ellipticity as measured by lensing.

3.3. Lensing ellipticity as a function of isolation criterion

The solid line in Fig. 4 shows the ellipticity of the stacked simulated shear map as a function of the closest neighbor distance used in our isolation criterion. The equivalent results obtained using SDSS data are shown by the points and error bars, which are taken from table 3 in Evans & Bridle (2008). We see excellent agreement between the two studies. Note that the error bars are strongly correlated since there is an overlap between the samples of clusters used.

The clusters appear slightly more circular for larger cut radii which is to be expected if the main effect is to exclude more physically associated clusters which are more likely to lie along the major axis of the cluster. For a smaller close neighbor distance value, we expect more clusters to be accepted. For the crosses in Fig. 4, the number of clusters accepted for each cut radius was 6934, 4281, 2542 in increasing order of radius size. The corresponding number of clusters used in the analysis of the simulated data is 2193, 1364, 815.

The dashed line in Fig. 4 shows the mean value of f_p for all clusters in the sample for each close neighbour distance, as discussed in Section 2.1. This is roughly a constant with close neighbour distance. We expect this line to be flatter than that for the lensing stack because these axis ratios have been calculated from the particles identified to be within the cluster and therefore are not contaminated by neighboring structures.

This result suggests that it may not always be reasonable to use the ellipticities from the conventional method, using quadrupole moments of cluster particles, as a proxy for the ellipticity expected from lensing.

The dotted line shows the results from Hopkins et al. (2005) (for clusters at redshift $z = 0.2$) and is in very good agreement with our results from a similar method.

4. CONCLUSIONS AND DISCUSSIONS

Through the pattern imprinted on the shear maps by the intervening massive cluster halos, Evans & Bridle (2008) detected a dark matter ellipticity of these halos at a 99.6% level, with an axis ratio of $f = 0.48^{+0.14}_{-0.09}$ from a joint χ^2 -analysis for an NFW model. We have repeated this analysis for simulated clusters and found excellent agreement with the observational results.

We have illustrated the need to stack cluster shear maps to average out the effect of neighboring structures, and found that on doing so, the resulting axis ratios agree well with those calculated using the conventional method for a given isolation criterion. The trend with isolation criterion appears slightly different for the conventional method than the lensing method though, as might be expected due to contamination by uncorrelated structures when more lax isolation criteria are applied.

Hopkins et al. (2005) use N -body simulations out to $z = 3$ to examine the evolution of ellipticity and alignment of clusters with redshift in a Λ CDM cosmology. They have results for the full 3-dimensions of their simulations as well as projected on the sky in two dimensions. Their results show that the mean dark matter ellipticity lies at $\langle\epsilon\rangle = 1 - f \sim 0.3 - 0.5$. Their results show an increasing ellipticity with redshift, i.e. a decreasing axis ratio from $\langle f \rangle \sim 0.7$ at $z = 0$ to $\langle f \rangle \sim 0.5$ at $z = 0.5$. The authors also conclude that ellipticities increase with cluster mass and cluster radius, and that higher mass clusters are more elliptical at all z . For our redshift range, the increase of ellipticities with redshift reported by Hopkins et al. (2005) is imperceptible. However, our simulated results f_p agree extremely well with theirs.

We would like to thank Terje Fredvik, Stein Vidar Haggfors Haugan and Øystein Elgarøy for helpful discussions. AKDE acknowledges support from the Research Council of Norway, Project No. 162830. SLB acknowledges sup-

REFERENCES

- Albrecht, A. et al. 2006
 Bridle, S. & Abdalla, F. B. 2007, *ApJ*, 655, L1
 Bridle, S. L., Hobson, M. P., Lasenby, A. N., & Saunders, R. 1998, *MNRAS*, 299, 895
 Clowe, D., Bradač, M., Gonzalez, A. H., Markevitch, M., Randall, S. W., Jones, C., & Zaritsky, D. 2006, *ApJ*, 648, L109
 Clowe, D., Gonzalez, A., & Markevitch, M. 2004, *ApJ*, 604, 596
 Cypriano, E. S., Sodré, L. J., Kneib, J.-P., & Campusano, L. E. 2004, *ApJ*, 613, 95
 Dahle, H., Hannestad, S., & Sommer-Larsen, J. 2003, *ApJ*, 588, L73
 Dubinski, J. & Carlberg, R. G. 1991, *ApJ*, 378, 496
 Evans, A. K. D. & Bridle, S. 2008, *ApJ*
 Evrard, A. E., Mohr, J. J., Fabricant, D. G., & Geller, M. J. 1993, *ApJ*, 419, L9+
 Floor, S. N., Melott, A. L., Miller, C. J., & Bryan, G. L. 2003, *ApJ*, 591, 741
 Flores, R. A., Allgood, B., Kravtsov, A. V., Primack, J. R., Buote, D. A., & Bullock, J. S. 2005, *ArXiv Astrophysics e-prints*
 Ho, S., Bahcall, N., & Bode, P. 2006, *Astrophys. J.*, 647, 8
 Hoekstra, H. 2007, *MNRAS*, 379, 317
 Hoekstra, H., Yee, H. K. C., & Gladders, M. D. 2004, *ApJ*, 606, 67
 Holder, G., Haiman, Z., & Mohr, J. J. 2001, *ApJ*, 560, L111
 Hopkins, P. F., Bahcall, N. A., & Bode, P. 2005, *Astrophys. J.*, 618, 1
 Jing, Y. P. 2002, *MNRAS*, 335, L89
 Johnston, D. E., Sheldon, E. S., Wechsler, R. H., Rozo, E., Koester, B. P., Frieman, J. A., McKay, T. A., Evrard, A. E., Becker, M. R., & Annis, J. 2007, *ArXiv e-prints*
 Kasun, S. F. & Evrard, A. E. 2005, *ApJ*, 629, 781
 Keeton, C. R. 2001, *ArXiv Astrophysics e-prints*
 Koester, B. P., McKay, T. A., Annis, J., Wechsler, R. H., Evrard, A., Bleem, L., Becker, M., Johnston, D., Sheldon, E., Nichol, R., Miller, C., Scranton, R., Bahcall, N., Barentine, J., Brewington, H., Brinkmann, J., Harvanek, M., Kleinman, S., Krzesinski, J., Long, D., Nitta, A., Schneider, D. P., Sneddin, S., Voges, W., & York, D. 2007, *ApJ*, 660, 239
 Levine, E. S., Schulz, A. E., & White, M. 2002, *ApJ*, 577, 569
 Mandelbaum, R., Seljak, U., & Hirata, C. M. 2008, *ArXiv e-prints*, 805
 Marshall, P. J., Hobson, M. P., Gull, S. F., & Bridle, S. L. 2002, *MNRAS*, 335, 1037
 Meneghetti, M., Bartelmann, M., Jenkins, A., & Frenk, C. 2007, *MNRAS*, 381, 171
 Mohr, J. J., Evrard, A. E., Fabricant, D. G., & Geller, M. J. 1995, *ApJ*, 447, 8
 Natarajan, P. & Refregier, A. 2000, *ApJ*, 538, L113
 Navarro, J. F., Frenk, C. S., & White, S. D. M. 1997, *ApJ*, 490, 493
 Paz, D. J., Lambas, D. G., Padilla, N., & Merchán, M. 2006, *MNRAS*, 366, 1503
 Peacock, J. A. et al. 2006, *ESA-ESO Working Group on "Fundamental Cosmology"*, Tech. rep.
 Pedersen, K. & Dahle, H. 2007, *ApJ*, 667, 26
 Plionis, M. & Basilakos, S. 2002, *MNRAS*, 329, L47
 Rahman, N., Shandarin, S. F., Motl, P. M., & Melott, A. L. 2004, *ArXiv Astrophysics e-prints*
 Richstone, D., Loeb, A., & Turner, E. L. 1992, *ApJ*, 393, 477
 Schramm, T. 1990, *A&A*, 231, 19
 Sheldon, E. S. et al. 2001, *Astrophys. J.*, 554, 881
 Spergel, D. N. et al. 2007, *ApJS*, 170, 377
 Splinter, R. J., Melott, A. L., Linn, A. M., Buck, C., & Tinker, J. 1997, *ApJ*, 479, 632
 Suwa, T., Habe, A., Yoshikawa, K., & Okamoto, T. 2003, *ApJ*, 588, 7
 Wang, Y., Yang, X., Mo, H. J., Li, C., van den Bosch, F. C., Fan, Z., & Chen, X. 2007, *ArXiv e-prints*, 710
 Warren, M. S., Quinn, P. J., Salmon, J. K., & Zurek, W. H. 1992, *ApJ*, 399, 405
 West, M. J., Jones, C., & Forman, W. 1995, *ApJ*, 451, L5+

Paper III

Evans, A. K. D.; Wehus, I. K.; Grøn, Ø.; Elgarøy, Ø.,
Geometrical constraints on dark energy,
Astron. and Astrophys., **430** (2005), 399-410

Geometrical constraints on dark energy

A. K. D. Evans¹, I. K. Wehus², Ø. Grøn^{3,2}, and Ø. Elgarøy¹

¹ Institute of Theoretical Astrophysics, University of Oslo, PO Box 1029, Blindern, 0315 Oslo, Norway
e-mail: oelgaroy@astro.uio.no

² Department of Physics, University of Oslo, PO Box 1048, Blindern, 0316 Oslo, Norway

³ Oslo College, Faculty of Engineering, Cort Adelers gt. 30, 0254 Oslo, Norway

Received 3 July 2004 / Accepted 23 September 2004

Abstract. We explore the recently introduced statefinder parameters. After reviewing their basic properties, we calculate the statefinder parameters for a variety of cosmological models, and investigate their usefulness as a means of theoretical classification of dark energy models. We then go on to consider their use in obtaining constraints on dark energy from present and future supernovae type Ia data sets. We find that it is non-trivial to extract the statefinders from the data in a model-independent way, and one of our results indicates that parametrizing the dark energy density as a polynomial of second order in the redshift is inadequate. Hence, while a useful theoretical and visual tool, applying the statefinders to observations is not straightforward.

Key words. cosmology: theory – cosmology: cosmological parameters

1. Introduction

It is generally accepted that we live in an accelerating universe. Early indications of this fact came from the magnitude-redshift relationship of galaxies (Solheim 1966), but the reality of cosmic acceleration was not taken seriously until the magnitude-redshift relationship was measured recently using high-redshift supernovae type Ia (SNIa) as standard candles (Riess et al. 1998; Perlmutter et al. 1999). The observations can be explained by invoking a contribution to the energy density with negative pressure, the simplest possibility being Lorentz Invariant Vacuum Energy (LIVE), represented by a cosmological constant. Independent evidence for a non-standard contribution to the energy budget of the universe comes from e.g. the combination of the power spectrum of the cosmic microwave background (CMB) temperature anisotropies and large-scale structure: the position of the first peak in the CMB power spectrum is consistent with the universe having zero spatial curvature, which means that the energy density is equal to the critical density. However, several probes of the large-scale matter distribution show that the contribution of standard sources of energy density, whether luminous or dark, is only a fraction of the critical density. Thus, an extra, unknown component is needed to explain the observations (Efsthathiou et al. 2002; Tegmark et al. 2004).

Several models describing an accelerated universe have been suggested. Typically, they are tested against the SNIa data on a model-by-model basis using the relationship between luminosity distance and redshift, $d_L(z)$, defined by the model. Another popular approach is to parametrize classes of dark energy models by their prediction for the so-called equation of

state $w(z) \equiv p_x/\rho_x$, where p_x and ρ_x are the pressure and the energy density, respectively, of the dark energy component in the model. One can then Taylor expand $w(z)$ around $z = 0$. The current data allow only relatively weak constraints on the zeroth-order term w_0 to be derived. A problem with this approach is that some attempts at explaining the accelerating Universe do not involve a dark component at all, but rather propose modifications of the Friedmann equations (Deffayet 2001; Deffayet et al. 2002; Dvali et al. 2000; Freese & Lewis 2002; Gondolo & Freese 2003; Sahni & Shtanov 2003). Furthermore, it is possible for two different dark energy models to give the same equation of state, as discussed by Padmanabhan (2002) and Padmanabhan & Choudhury (2003).

Recently, an alternative way of classifying dark energy models using geometrical quantities was proposed (Sahni et al. 2003, Alam et al. 2003). These so-called statefinder parameters are constructed from the Hubble parameter $H(z)$ and its derivatives, and in order to extract these quantities in a model-independent way from the data, one has to parametrize H in an appropriate way. This approach was investigated at length in Alam et al. (2003) using simulated data from a SNAP¹-type experiment. In this paper, we present a further investigation of this formalism. We generalize the formalism to universe models with spatial curvature in Sect. 2, and give expressions for the statefinder parameters in several specific dark energy models. In the same section, we also take a detailed look at how the statefinder parameters behave for quintessence models, and show that some of the statements about these models in Alam et al. (2003) have to be modified. In Sect. 3 we discuss what can

¹ see <http://snap.lbl.gov>

be learned from current SNIa data, considering both direct χ^2 fitting of model parameters to data, and statefinder parameters. In Sect. 4 we look at simulated data from an idealized SNIa survey, showing that reconstruction of the statefinder parameters from data is likely to be non-trivial. Finally, Sect. 5 contains our conclusions.

2. Statefinder parameters: Definitions and properties

The Friedmann-Robertson-Walker models of the universe have earlier been characterized by the Hubble parameter and the deceleration parameter, which depend on the first and second derivatives of the scale factor, respectively:

$$H = \frac{\dot{a}}{a} \quad (1)$$

$$q = -\frac{\ddot{a}a}{\dot{a}^2} = -\frac{\ddot{H}}{H^2} - 1, \quad (2)$$

where dots denote differentiation with respect to time t . The proposed SNAP satellite will provide accurate determinations of the luminosity distance and redshift of more than 2000 supernovae of type Ia. These data will permit a very precise determination of $a(z)$. It will then be important to include also the third derivative of the scale factor in our characterization of different universe models.

Sahni and coworkers (Sahni et al. 2003; Alam et al. 2003) recently proposed a new pair of parameters (r, s) called *statefinders* as a means of distinguishing between different types of dark energy. The statefinders were introduced to characterize flat universe models with cold matter (dust) and dark energy. They were defined as

$$r = \frac{\ddot{a}}{aH^3} = \frac{\ddot{H}}{H^3} + 3\frac{\dot{H}}{H^2} + 1 \quad (3)$$

$$s = \frac{r-1}{3\left(q-\frac{1}{2}\right)}. \quad (4)$$

Introducing the cosmic redshift $1+z = 1/a \equiv x$, we have $\dot{H} = -H'H/a$, where $H' = dH/dx$, the deceleration parameter is given by

$$q(x) = \frac{H'}{H}x - 1. \quad (5)$$

Calculating r , making use of $a' = -a^2$, we obtain

$$r(x) = 1 - 2\frac{H'}{H}x + \left(\frac{H'^2}{H^2} + \frac{H''}{H}\right)x^2. \quad (6)$$

The statefinder $s(x)$, for flat universe models, is then found by inserting the expressions (5) and (6) into Eq. (4). The generalization to non-flat models will be given in the next subsection.

The Friedmann equation takes the form²

$$H^2 = \frac{8\pi G}{3}(\rho_m + \rho_x) - \frac{k}{a^2}, \quad (7)$$

where ρ_m is the density of cold matter and ρ_x is the density of the dark energy, and $k = -1, 0, 1$ is the curvature parameter

with $k = 0$ corresponding to a spatially flat universe. The dust component is pressureless, so the equation of energy conservation implies

$$\rho_m = \rho_{m0}a^{-3}. \quad (8)$$

This gives for the density of dark energy:

$$\begin{aligned} \rho_x &= \rho_c - \rho_m - \frac{3k}{8\pi G a^2} \\ &= \frac{3}{8\pi G}(H^2 + kx^2 - \Omega_{m0}H_0^2x^3), \end{aligned} \quad (9)$$

where Ω_{m0} and Ω_{x0} are the present densities of matter and dark energy, respectively, in units of the present critical density $\rho_{c0} = 3H_0^2/8\pi G$. In the following, we will use the notation $\Omega_i \equiv 8\pi G\rho_i(t)/3H^2(t)$, $\Omega_{i0} \equiv \Omega_i(t=t_0)$, where t_0 is the present age of the Universe, and also $\Omega = \sum_i \Omega_i$. From Friedmann's acceleration equation

$$\frac{\ddot{a}}{a} = -\frac{4\pi G}{3} \sum_i (\rho_i + 3p_i), \quad (10)$$

where p_i is the contribution to the pressure from component i , it follows that

$$p_x = \frac{H^2}{4\pi G} \left(q - \frac{\Omega}{2} \right) = \frac{3}{8\pi G} \left[\frac{1}{3}(H^2)'x - \frac{k}{3}x^2 - H^2 \right]. \quad (11)$$

Hence, if dark energy is described by an equation of state $p_x = w(x)\rho_x$, we have

$$w(x) = \frac{\frac{1}{3}(H^2)'x - H^2 - \frac{k}{3}x^2}{H^2 + kx^2 - H_0^2\Omega_{m0}x^3}. \quad (12)$$

In the following subsections, we calculate statefinder parameters for universe models with different types of dark energy.

2.1. Models with an equation of state $p = w(z)\rho$

First we consider dark energy obeying an equation of state of the form $p_x = w\rho_x$, where w may be time-dependent. Quintessence models (Wetterich 1988; Peebles & Ratra 1988), where the dark energy is provided by a scalar field evolving in time, fall in this category. The formalism in Sahni et al. (2003) and Alam et al. (2003) will be generalized to permit universe models with spatial curvature. Then Eq. (4) is generalized to

$$s = \frac{r - \Omega}{3(q - \Omega/2)}, \quad (13)$$

where $\Omega = \Omega_m + \Omega_x = 1 - \Omega_k$, and $\Omega_k = -k/(a^2H^2)$.

The deceleration parameter can be expressed as

$$q = \frac{1}{2}[\Omega_m + (1 + 3w)\Omega_x] = \frac{1}{2}(\Omega + 3w\Omega_x). \quad (14)$$

After differentiation of Eq. (2) and some simple algebra one finds

$$r = 2q^2 + q - \frac{\dot{q}}{H}, \quad (15)$$

and further manipulations lead to

$$r = \Omega_m + \left[1 + \frac{9}{2}w(1+w) \right] \Omega_x - \frac{3}{2} \frac{\dot{w}}{H} \Omega_x. \quad (16)$$

² Throughout this paper we use units where the speed of light $c = 1$.

Inserting Eq. (16) into Eq. (13) gives

$$s = 1 + w - \frac{1}{3} \frac{\dot{w}}{wH}. \quad (17)$$

For a flat universe $\Omega_m + \Omega_x = 1$ and the expression for r simplifies to

$$r = 1 + \frac{9}{2}w(1+w)\Omega_x - \frac{3}{2}\frac{\dot{w}}{H}\Omega_x. \quad (18)$$

Note that for the case of LIVE, $w = -1 = \text{constant}$, and one finds $r = \Omega$, $s = 0$ for all redshifts. For a model with curvature and matter only one gets $r = 2q = \Omega_m$, $s = 2/3$. The same result is obtained for a flat model with matter and dark energy with a constant equation of state $w = -1/3$, which is the equation of state of a frustrated network of non-Abelian cosmic strings (Eichler 1996; Bucher & Spergel 1999). Thus, the statefinder parameters cannot distinguish between these two models. However, neither of these two model universes are favoured by the current data (for one thing, they are both decelerating), so this is probably an example of academic interest only.

For a constant w , and $\Omega_{m0} + \Omega_{x0} = 1$, the q - r plane for different values of Ω_x and w is shown in Fig. 1. Quintessence with $w = \text{constant}$ is called quiescence. The relation between q and r for flat universe models with matter+quiescence is found by eliminating Ω_x between Eq. (14), with $\Omega = 1$, and Eq. (16). This gives

$$r = 3(1+w)q - \frac{1}{2}(1+3w), \quad (19)$$

which is the equation of the dotted straight lines in Fig. 1. When $\Omega_x = 1$, all models lie on the solid curve given by

$$q = \frac{3}{2}w + \frac{1}{2} \quad (20)$$

$$r = \frac{9}{2}w(1+w) + 1, \quad (21)$$

or

$$r = 2q^2 + q, \quad (22)$$

in accordance with Eq. (15) since $\dot{q} = 0$ for these models. This curve is the lower bound for all models with a constant w . For $-1 \leq w \leq 0$, all matter+quiescence models will at any time fall in the sector between this curve and the $r = 1$ -line which corresponds to Λ CDM. The results shown in Alam et al. (2003) seem to indicate that all matter+quiescence models will fall within this same sector as the matter+quiescence models do. However, as we will show below, this is not strictly correct.

2.2. Scalar field models

If the source of the dark energy is a scalar field ϕ , as in the quintessence models (Wetterich 1988; Peebles & Ratra 1988), the equation of state factor w is

$$w = \frac{\dot{\phi}^2 - 2V(\phi)}{\dot{\phi}^2 + 2V(\phi)}. \quad (23)$$

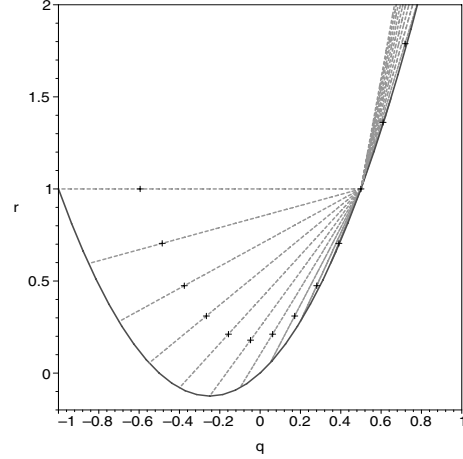


Fig. 1. The q - r -plane for flat matter+quiescence models. The horizontal curve has $w = -1$ (Λ CDM). Then w increases by $1/10$ counterclockwise until we reach $w = 1$ in the upper right. When $\Omega_{x0} = 0$ all models start at the point $q = 0.5$, $r = 1$ (Einstein-de Sitter model). As Ω_{x0} increases every model moves towards the solid curve which marks $\Omega_{x0} = 1$. The crosses mark the present epoch.

Then,

$$r = \Omega + 12\pi G \frac{\dot{\phi}^2}{H^2} + 8\pi G \frac{\dot{V}}{H^3}, \quad (24)$$

and furthermore,

$$q - \frac{\Omega}{2} = \frac{3}{2}w\Omega_x = 4\pi G \frac{p_x}{H^2} = \frac{4\pi G}{H^2} \left(\frac{1}{2}\dot{\phi}^2 - V \right). \quad (25)$$

Hence the statefinder s is

$$s = \frac{2 \left(\dot{\phi}^2 + \frac{2}{3}\frac{\dot{V}}{H} \right)}{\dot{\phi}^2 - 2V}. \quad (26)$$

For models with matter+quintessence+curvature, the Friedmann and energy conservation equations give

$$\dot{H} = -3H^2 + \frac{1}{2M^2} \left(\frac{1}{2}\rho_m - V(\phi) + \frac{2}{3}\rho_k \right) \quad (27)$$

$$\frac{1}{2}\dot{\phi}^2 = 3H^2M^2 - \rho_m - V(\phi) - \rho_k \quad (28)$$

$$\dot{\rho}_m = -3H\rho_m \quad (29)$$

$$\dot{\rho}_k = -2H\rho_k, \quad (30)$$

and

$$q = \frac{1}{2}\Omega_m + 2\Omega_{kin} - \Omega_{pot} \quad (31)$$

$$r = \Omega_m + 10\Omega_{kin} + \Omega_{pot} + 3\sqrt{6\Omega_{kin}} \frac{MV'}{\rho_c}. \quad (32)$$

As customary when discussing quintessence, we have introduced the Planck mass $M^2 = 1/8\pi G$. Furthermore, we have defined $\Omega_{kin} = \dot{\phi}^2/2\rho_c$, and $\Omega_{pot} = V(\phi)/\rho_c$. For an exponential potential, $V(\phi) = A \exp(-\lambda\phi/M)$, looking at values at the present epoch, and eliminating Ω_{pot0} , using $\Omega_{m0} + \Omega_{kin0} + \Omega_{pot0} + \Omega_{k0} = 1$, one obtains

$$q_0 = \frac{3}{2}\Omega_{m0} - (1 - \Omega_{k0}) + 3\Omega_{kin0} \quad (33)$$

$$r_0 = (1 - \Omega_{k0}) + 9\Omega_{kin0} - 3\lambda\sqrt{6\Omega_{kin0}(1 - \Omega_{k0} - \Omega_{m0} - \Omega_{kin0})}. \quad (34)$$

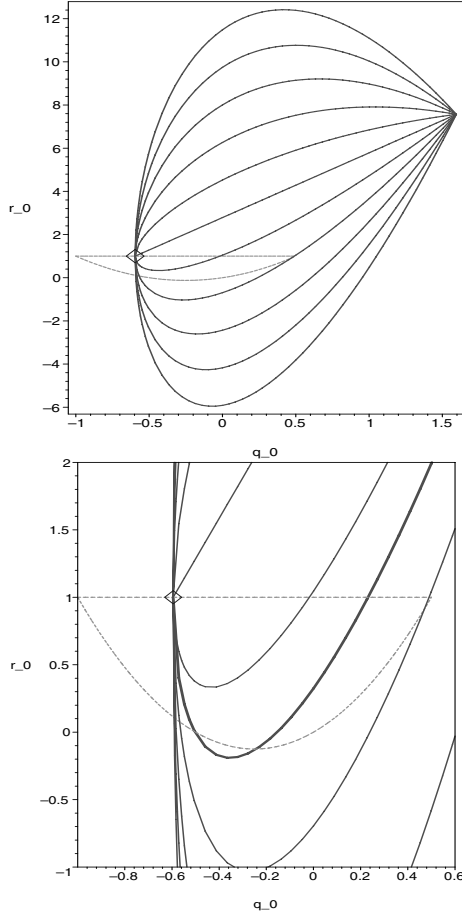


Fig. 2. Present values of q and r for matter+quintessence with an exponential potential. *Top panel:* from top to bottom the different curves have $\lambda = -5, -4, -3, -2, -1, 0, 1, 2, 3, 4, 5$. They all start at the point $(q_0(\Omega_{\text{kin}} = .73) = 1.595, r_0(\Omega_{\text{kin}} = .73) = 7.57)$ (matter+Zeldovich gas ($p_x = \rho_x$)). As Ω_{kin} decreases when we move to the left, they join at the point $(q_0(\Omega_{\text{kin}} = 0) = -0.595, r_0(\Omega_{\text{kin}} = 0) = 1)$ (Λ CDM, marked with a diamond). The dotted curve shows the area all matter+quintessence models must lie within at all times. *Bottom panel:* zoom-in of the figure above. Here the curve having $\lambda^2 = 2$ is also plotted (thick line).

By choosing for instance $\Omega_{m0} = 0.27$ and $\Omega_{k0} = 0$ we can plot the values of q_0 and r_0 for varying $\Omega_{\text{kin}0}$; see Fig. 2. As we can see from Eqs. (33)–(34), when $\Omega_{\text{kin}0} = 0$, q_0 and r_0 are independent of λ , and have the same values as in the Λ CDM model. This is obvious, since taking away the kinetic term will reduce quintessence to LIVE. However, when $\Omega_{\text{kin}0}$ is slightly greater than 0 we can make r_0 as large or as small as we like, by choosing $|\lambda|$ sufficiently large. There is no reason all quintessence models should lie inside the constant- w -curve. However, in order to get an accelerating universe today we must have $\lambda^2 < 2$. But also for $\lambda^2 < 2$ the present values of q_0 and r_0 can lie outside the constant- w -curve. In fact, when we move on to the time-evolving statefinders, plotting q and r as functions of time for given initial conditions, we obtain plots like Fig. 3. Here we have chosen as initial conditions $\Omega_{m0} = 0.27$ and $\Omega_{k0} = 0$ as above, and $h = 0.71$. The last initial condition, for the quintessence field, we have chosen to be $\phi_0 = M/100$ combined with the overall constant A

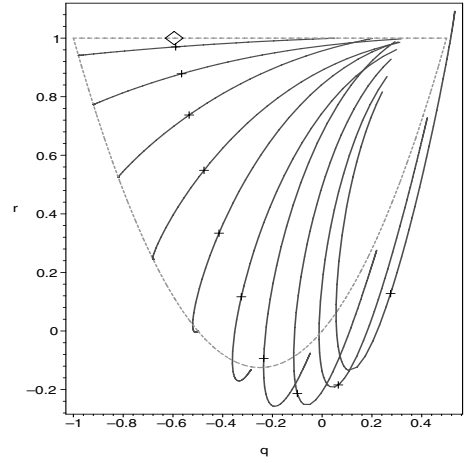


Fig. 3. Time-evolution of q and r for models with matter and quintessence with an exponential potential. The crosses mark the present epoch. The diamond represents the present Λ CDM model. The curve on top has $\lambda = 0.2$ and then λ increases by 0.2 for each curve going counter-clockwise until we reach $\lambda = 2$ to the right. The corresponding values for Ω_{kin} today are $\Omega_{\text{kin}0} = 0.002, 0.01, 0.02, 0.04, 0.06, 0.09, 0.12, 0.165, 0.22, 0.29$. The dotted curve shows the area all matter+quintessence models must lie within at all times. We see that all models will eventually move towards this curve.

in the potential chosen to give $\Omega_{\text{kin}0}$ as stated in the caption of Fig. 3. This corresponds to the universe being matter dominated at earlier times. When $\Omega_{\text{pot}0} \gg \Omega_{\text{kin}0}$ we have high acceleration today. Choosing $\Omega_{\text{kin}0} = 0$ will again give us Λ CDM. The three rightmost curves in the figure have $\lambda^2 > 2$ and no eternal acceleration, although the $\lambda = 1.6$ universe accelerates today. It seems that in order to get a universe close to what we observe, r and q for models with matter+quintessence with an exponential potential will essentially lie within the same area as matter+quintessence models. In Fig. 4 we have plotted the trajectories in the s_0 – r_0 -plane and the s_0 – q_0 -plane for the same models as in Fig. 2, to be compared with Figs. 5c and 5d in Alam et al. (2003).

Choosing instead a power-law potential $V(\phi) = A\phi^{-\alpha}$ gives $V' = -\frac{\alpha}{\phi}V$ and

$$q = \frac{1}{2}\Omega_m + 2\Omega_{\text{kin}} - \Omega_{\text{pot}} \quad (35)$$

$$r = \Omega_m + 10\Omega_{\text{kin}} + \Omega_{\text{pot}} - 3\alpha \frac{M}{\phi} \sqrt{6\Omega_{\text{kin}}\Omega_{\text{pot}}}. \quad (36)$$

We see that for $\phi_0 = M$ we get the same curves in the q_0 – r_0 -plane when varying α as we got when varying λ in the exponential potential, see Fig. 2. We also see that varying ϕ_0 for a given value of α is essentially the same as varying α . Figure 5 shows the q_0 – r_0 -plane for the case $\alpha = 2$. Figure 6 shows an example of time-evolving statefinders ($\phi_0 = M$, $\Omega_{\text{kin}0} = 0.05$, $\Omega_{m0} = 0.27$, $\Omega_{k0} = 0$, $h = 0.71$). If one compares this plot with Fig. 1b in Alam et al. (2003), the two do not quite agree. Alam et al. (2003) do not give detailed information about the initial conditions for the quintessence field. Our initial conditions correspond to a universe which was matter-dominated up to now, when quintessence is taking over.

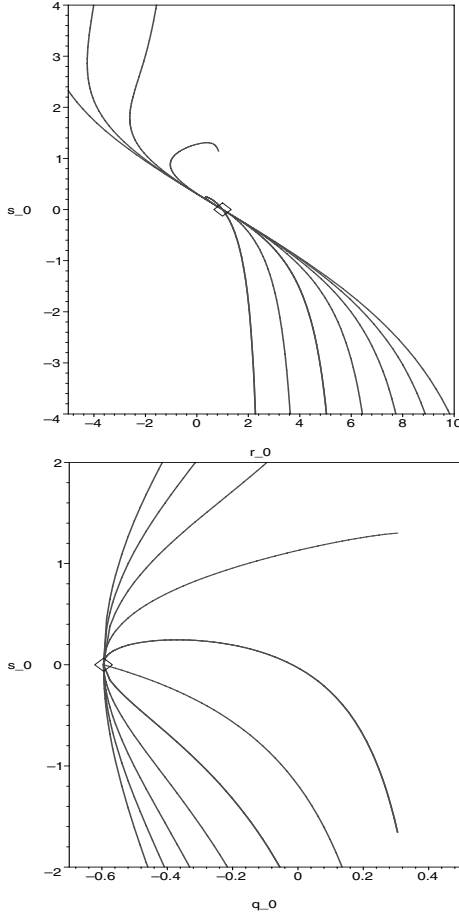


Fig. 4. Present values of the statefinder parameters and the deceleration parameter for models with matter and quintessence with an exponential potential. The diamond represents the Λ CDM model. *Top panel:* from left to right the different curves have $\lambda = -5, -4, -3, -2, -1, 0, 1, 2, 3, 4, 5$. *Bottom panel:* from top to bottom the different curves have $\lambda = -5, -4, -3, -2, -1, 0, 1, 2, 3, 4, 5$.

2.3. Dark energy fluid models

We will now find expressions for r and s which are valid even if the dark energy does not have an equation of state of the form $p_x = w\rho_x$. This is the case e.g. in the Chaplygin gas models (Kamenshchik, Moschella & Pasquier 2001; Bilic et al. 2002). The expression for the deceleration parameter can be written as

$$q = \frac{1}{2} \left(1 + 3 \frac{p_x}{\rho_x} \right) \Omega, \quad (37)$$

and using this in Eq. (15) we find

$$r = \left(1 - \frac{3}{2} \frac{\dot{p}_x}{H \rho_x} \right) \Omega \quad (38)$$

$$s = -\frac{1}{3H} \frac{\dot{p}_x}{p_x}. \quad (39)$$

For a universe with cold matter and dark energy one finds

$$r = \left(1 + \frac{9}{2} \frac{\rho_x + p_x}{\rho_m + \rho_x} \frac{\partial p_x}{\partial \rho_x} \right) \Omega \quad (40)$$

$$s = \left(1 + \frac{\rho_x}{p_x} \right) \frac{\partial p_x}{\partial \rho_x}. \quad (41)$$

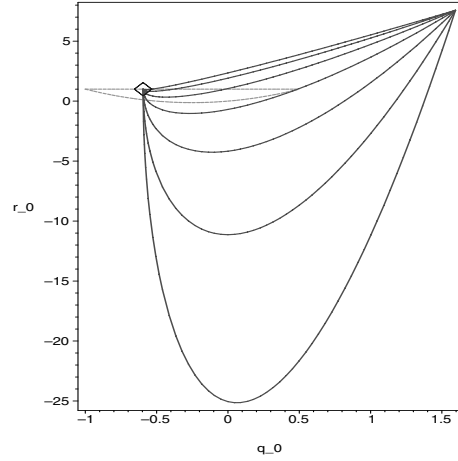


Fig. 5. Present values of q and r for matter+quintessence with a power-law potential with $\alpha = 2$. From top to bottom the different curves have $\phi_0 = 8M, 4M, 2M, M, \frac{M}{2}, \frac{M}{4}, \frac{M}{8}$. The diamond represents the Λ CDM model. The dotted curve shows the area all matter+quintessence models must lie within at all times.

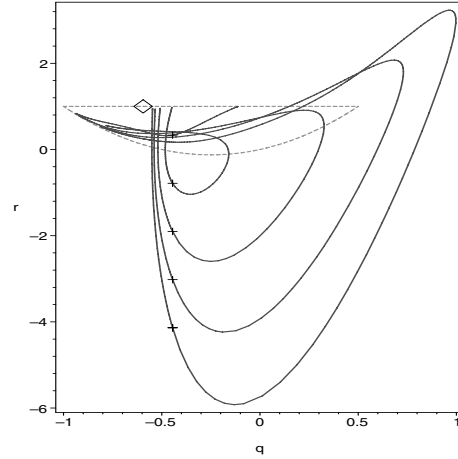


Fig. 6. Time-evolution of q and r for models with matter and quintessence with a power-law potential. The crosses mark the present epoch, the diamond represents the present Λ CDM model. All models start out from the horizontal Λ CDM line and will eventually end up as a de Sitter universe ($q = -1, r = 1$). The curve going deepest down has $\alpha = 5$ and moving upwards we have $\alpha = 4, 3, 2, 1$. The dotted curve shows the area all matter+quintessence models must lie within at all times. Obviously the same is not the case for matter+quintessence models.

The Generalized Chaplygin Gas (GCG) has an equation of state (Bento et al. 2002)

$$p = -\frac{A}{\rho^\alpha}, \quad (42)$$

and integration of the energy conservation equation gives

$$\rho = \left[A + B a^{-3(1+\alpha)} \right]^{\frac{1}{1+\alpha}}, \quad (43)$$

where B is a constant of integration. This can be rewritten as

$$\rho = \rho_0 \left[A_s + (1 - A_s) x^{3(1+\alpha)} \right]^{\frac{1}{1+\alpha}}, \quad (44)$$

where $\rho_0 = (A+B)^{1/(1+\alpha)}$, and $A_s = A/(A+B)$. For a flat universe with matter and a GCG, the Hubble parameter is given by

$$\frac{H^2(x)}{H_0} = \Omega_{m0}x^3 + (1 - \Omega_{m0}) \left[A_s + (1 - A_s)x^{3(1+\alpha)} \right]^{\frac{1}{1+\alpha}}. \quad (45)$$

This leads to the following expressions for $q(x)$ and $r(x)$:

$$q(x) = \frac{3}{2} \frac{\Omega_{m0}x^3 + (1 - \Omega_{m0})(1 - A_s)v^{\frac{3}{\beta}-1}x^\beta}{\Omega_{m0}x^3 + (1 - \Omega_{m0})v^{3/\beta}} - 1 \quad (46)$$

$$r(x) = 1 - 3 \frac{x}{h^2(x)}f(x) + \frac{3}{2} \frac{x^2}{h^2(x)}f'(x), \quad (47)$$

where $\beta = 3(1 + \alpha)$, $h(x) = H(x)/H_0$, and

$$v = A_s + (1 - A_s)x^\beta \quad (48)$$

$$f(x) = \Omega_{m0}x^2 + (1 - \Omega_{m0})(1 - A_s)v^{\frac{3}{\beta}-1}x^{\beta-1}. \quad (49)$$

In the r - s plane, the GCG models will lie on curves given by (see Gorini et al. 2003)

$$r = 1 - \frac{9}{2} \frac{s(s + \alpha)}{\alpha}. \quad (50)$$

We note that a recent comparison of GCG models with SNIa data found evidence for $\alpha > 1$ (Bertolami et al. 2004).

2.4. Cardassian models

As an alternative to adding a negative-pressure component to the energy-momentum tensor of the Universe, one can take the view that the present phase of accelerated expansion is caused by gravity being modified, e.g. by the presence of large extra dimensions. For a general discussion of extra-dimensional models and statefinder parameters, see Alam & Sahni (2002).

As an example, we will consider the Modified Polytropic Cardassian ansatz (MPC) (Freese & Lewis 2002; Gondolo & Freese 2003), where the Hubble parameter is given by

$$H(x) = H_0 \sqrt{\Omega_{m0}x^3(1 + u)^{1/\psi}}, \quad (51)$$

with

$$u = u(x) = \frac{\Omega_{m0}^{-\psi} - 1}{x^{3(1-n)\psi}}, \quad (52)$$

and where n and ψ are new parameters (ψ is usually called q in the literature, but we use a different notation here to avoid confusion with the deceleration parameter). For this model, the deceleration parameter is given by

$$q(x) = \frac{3}{2} \left[\frac{1 + nu}{1 + u} \right] - 1 \quad (53)$$

and the statefinder r by

$$r(x) = 1 - \frac{9}{4} \frac{1 + nu}{1 + u} \left[1 + \frac{u(1 - n) - (1 + nu)}{1 + u} - 2q \frac{(1 - n)^2 u}{(1 + u)(1 + nu)} \right]. \quad (54)$$

2.5. The luminosity distance to third order in z

The luminosity distance is given by

$$d_L = \frac{1 + z}{H_0 \sqrt{|\Omega_{k0}|}} S_k(\sqrt{|\Omega_{k0}|}I), \quad (55)$$

where $S_k(x) = \sin x$ for $k = 1$, $S_k(x) = x$ for $k = 0$, $S_k(x) = \sinh x$ for $k = -1$, and

$$I = H_0 \int_0^z \frac{dz}{H(z)}. \quad (56)$$

The statefinder parameters appear when one expands the luminosity distance to third order in the redshift z . This expansion has been carried out by Chiba & Nakamura (1998) and Visser (2003). The result is

$$d_L \approx \frac{z}{H_0} \left[1 + \frac{1}{2}(1 - q_0)z - \frac{1}{6}(1 + r_0 - q_0 - 3q_0^2 - \Omega_{k0})z^2 \right]. \quad (57)$$

One can also find an expression for the present value of the time derivative of the equation of state parameter w in terms of the statefinder r_0 . A Taylor expansion to first order in z gives

$$w(z) \approx w_0 - \frac{2}{3} \left[1 + \frac{9}{2}w_0(1 + w_0) + \frac{\Omega_{m0} - r_0}{\Omega_{x0}} \right] z. \quad (58)$$

3. Lessons drawn from current SNIa data

In this section we will consider the SNIa data presently available, in particular whether one can use them to learn about the statefinder parameters. We will use the recent collection of SNIa data in Riess et al. (2004), their “gold” sample consisting of 157 supernovae at redshifts between ~ 0.01 and ~ 1.7 .

3.1. Model-independent constraints

The approximation to d_L in Eq. (57) is independent of the cosmological model, the only assumption made is that the Universe is described by the Friedmann-Robertson-Walker metric. We see that, in addition to H_0 , this third-order expansion of d_L depends on q_0 and the combination $r_0 - \Omega_{k0}$. Fitting these parameters to the data, we find the constraints shown in Fig. 7. The results are consistent with those of similar analyses in Caldwell & Kamionkowski (2004) and Gong (2004). In Fig. 8 we show the marginalized distributions for q_0 and $r_0 - \Omega_{k0}$. We note that the supernova data firmly support an accelerating universe, $q_0 < 0$ at more than 99% confidence. However, about the statefinder parameter r_0 , little can be learned without an external constraint on the curvature. Imposing a flat universe, e.g. by inflationary prejudice or by invoking the CMB peak positions, there is still a wide range of allowed values for r_0 . This is an indication of the limited ability of the current SNIa data to place constraints on models of dark energy. There is only limited information on anything beyond the present value of the second derivative of the Hubble parameter.

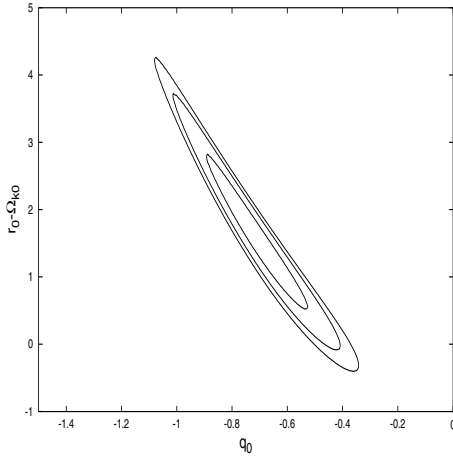


Fig. 7. Likelihood contours (68, 95 and 99%) resulting from a fit of the expansion of the luminosity distance to third order in z .

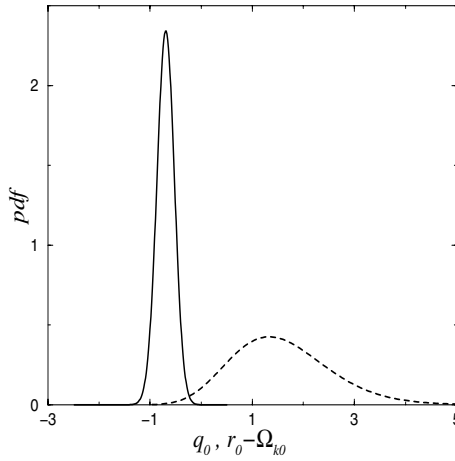


Fig. 8. Marginalized probability distributions for q_0 (full line) and $r_0 - \Omega_{k0}$ (dotted line).

Under the assumption of a spatially flat universe, $\Omega_{k0} = 0$, with $\Omega_{m0} = 0.3$, one can use Eq. (58) to obtain constraints on w_0 and w_1 in the expansion $w(z) = w_0 + w_1 z$ of the equation of state of dark energy. The resulting likelihood contours are shown in Fig. 9. As can be seen in this figure, there is no evidence for time evolution in the equation of state, the observations are consistent with $w_1 = 0$. The present supernova data show a slight preference for a dark energy component of the ‘phantom’ type with $w_0 < -1$ (Caldwell 2002). Note, however, that the relatively tight contours obtained here are caused by the strong prior $\Omega_{m0} = 0.3$. It should also be noted that the third-order expansion of d_L is not a good approximation to the exact expression for high z and in some regions of the parameter space.

3.2. Direct test of models against data

The standard way of testing dark energy models against data is by maximum likelihood fitting of their parameters. In this

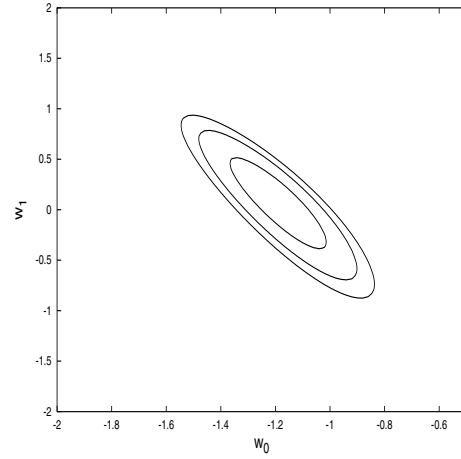


Fig. 9. Likelihood contours (68, 95 and 99%) for the coefficients w_0 and w_1 in the linear approximation to the equation of state $w(z)$ of dark energy, resulting from a fit of the expansion of the luminosity distance to third order in z .

subsection we will consider the following models:

1. The expansion of d_L to second order in z , with h and q_0 as parameters.
2. The third-order expansion of d_L , with h , q_0 , and $r_0 - \Omega_{k0}$ as parameters.
3. Flat Λ CDM models, with Ω_{m0} and h as parameters to be varied in the fit.
4. Λ CDM with curvature, so that Ω_{m0} , $\Omega_{\Lambda0}$ (the contribution of the cosmological constant to the energy density in units of the critical density, evaluated at the present epoch), and h are varied in the fits.
5. Flat quiescence models, that is, models with a constant equation of state w for the dark energy component. The parameters to be varied in the fit are Ω_{m0} , w , and h .
6. The Modified Polytropic Cardassian (MPC) ansatz, with Ω_{m0} , q , n , and h as parameters to be varied.
7. The Generalized Chaplygin Gas (GCG), with Ω_{m0} , A_s , α , and h as parameters to be varied.
8. The ansatz of Alam et al. (2003),

$$H = H_0 \sqrt{\Omega_{m0} x^3 + A_0 + A_1 x + A_2 x^2}, \quad (59)$$

where we restrict ourselves to flat models, so that $A_0 = 1 - \Omega_{m0} - A_1 - A_2$. The parameters to be varied are Ω_{m0} , A_1 , A_2 , and h .

Note that these models have different numbers of free parameters. To get an idea of which of these models is actually preferred by the data, we therefore employ the Bayesian Information Criterion (BIC) (Schwarz 1978; Liddle 2004). This is an approximation to the Bayes factor (Jeffreys 1961), which gives the posterior probability of one model relative to another assuming that there is no objective reason to prefer one of the models prior to fitting the data. It is given by

$$\mathcal{B} = \chi^2_{\min} + N_{\text{par}} \ln N_{\text{data}}, \quad (60)$$

where χ^2_{\min} is the minimum value of the χ^2 for the given model against the data, N_{par} is the number of free parameters, and N_{data}

Table 1. Results of fitting the models considered in this subsection to the SNIa data.

Model	χ^2_{\min}	# parameters	\mathcal{B}
2. order expansion	177.1	2	187.2
3. order expansion	162.3	3	177.5
Flat Λ CDM	163.8	2	173.9
Λ CDM with curvature	161.2	3	176.4
Flat + constant EoS	160.0	3	175.2
MPC	160.3	4	180.5
GCG	161.4	4	181.6
Alam et al.	160.5	4	180.7

is the number of data points used in the fit. As a result of the approximations made in deriving it, \mathcal{B} is given in terms of the minimum χ^2 , even though it is related to the integrated likelihood. The preferred model is the one which minimizes \mathcal{B} . In Table 1 we have collected the results for the best-fitting models. When comparing models using the BIC, the rule of thumb is that a difference of 2 in the BIC is positive evidence against the model with the larger value, whereas if the difference is 6 or more, the evidence against the model with the larger BIC is considered strong. The second-order expansion of d_L is then clearly disfavoured, thus the current supernova data give information, although limited, on $r_0 - \Omega_{k0}$. We see that there is no indication in the data that curvature should be added to the Λ CDM model. Also, the last three models in Table 1 seem to be disfavoured. One can conclude that there is no evidence in the current data that anything beyond flat Λ CDM is required. This does not, of course, rule out any of the models, but tells us that the current data are not good enough to reveal physics beyond spatially flat Λ CDM. A similar conclusion was reached by Liddle (2004) using a more extensive collection of cosmological data sets and considering adding parameters to the flat Λ CDM model with scale-invariant adiabatic fluctuations.

3.3. Statefinder parameters from current data

If the luminosity distance d_L is found as a function of redshift from observations of standard candles, one can obtain the Hubble parameter formally from

$$H(x) = \left[\frac{d}{dx} \left(\frac{d_L}{x} \right) \right]^{-1}. \quad (61)$$

However, since observations always contain noise, this relation cannot be applied straightforwardly to the data. Alam et al. (2003) suggested parametrizing the dark energy density as a second-order polynomial in x , $\rho_x = \rho_{c0}(A_0 + A_1x + A_2x^2)$, leading to a Hubble parameter of the form

$$H(x) = H_0 \sqrt{\Omega_{m0}x^3 + A_0 + A_1x + A_2x^2}, \quad (62)$$

and fitting A_0 , A_1 , and A_2 to data. This parametrization reproduces exactly the cases $w = -1$ ($A_1 = A_2 = 0$), $w = -2/3$

($A_0 = A_2 = 0$), and $w = -1/3$ ($A_0 = A_1 = 0$), and the luminosity distance-redshift relationship is given by

$$d_L = \frac{1+z}{H_0} \int_1^{1+z} \frac{dx}{\sqrt{\Omega_{m0}x^3 + A_0 + A_1x + A_2x^2}}. \quad (63)$$

Having fitted the parameters A_0 , A_1 , and A_2 to e.g. supernova data using Eq. (63), one can then find q and r by substituting Eq. (62) into Eqs. (5) and (6):

$$q(x) = \frac{1}{2} \left(1 - \frac{A_2x^2 + 2A_1x + 3A_0}{\Omega_{m0}x^3 + A_2x^2 + A_1x + A_0} \right) \quad (64)$$

$$r(x) = \frac{\Omega_{m0}x^3 + A_0}{\Omega_{m0}x^3 + A_0 + A_1x + A_2x^2}, \quad (65)$$

and furthermore the statefinder s is found to be

$$s(x) = \frac{2}{3} \frac{A_1x + A_2x^2}{3A_0 + 2A_1x + A_2x^2}, \quad (66)$$

and the equation of state is given by

$$w(x) = -1 + \frac{1}{3} \frac{A_1x + 2A_2x^2}{A_0 + A_1x + A_2x^2}. \quad (67)$$

The simulations of Alam et al. (2003) indicated that the statefinder parameters can be reconstructed well from simulated data based on a range of dark energy models, so we will for now proceed on the assumption that the parametrization in Eq. (62) is adequate for the purposes of extracting q , r and s from SNIa data. We comment this issue in Sect. 4.

In Fig. 10 we show the deceleration parameter q and the statefinder r extracted from the current SNIa data. The error bars in the figure are 1σ limits. We have also plotted the model predictions for the same quantities (based on best-fitting parameters with errors) for Λ CDM, quiescence, and the MPC. The figure shows that all models are consistent at the 1σ level with q and r extracted using Eq. (62). Thus, with the present quality of SNIa data, the statefinder parameters are, not surprisingly, no better at distinguishing between the models than a direct comparison with the SNIa data. We next look at simulated data to get an idea of how the situation will improve with future data sets.

4. Future data sets

We will now make an investigation of what an idealized SNIa survey can teach us about statefinder parameters and dark energy, following the procedure in Saini et al. (2004).

A SNAP-like satellite is expected to observe ~ 2000 SN up to $z \sim 1.7$. Dividing the interval $0 < x \leq 1.7$ into 50 bins, we therefore expect ~ 40 observations of SN in each bin. Empirically, SNIa are very good standard candles with a small dispersion in apparent magnitude $\sigma_{\text{mag}} = 0.15$, and there is no indication of redshift evolution. The apparent magnitude is related to the luminosity distance through

$$m(z) = \mathcal{M} + 5 \log D_L(z), \quad (68)$$

where $\mathcal{M} = M_0 + 5 \log[H_0^{-1} \text{Mpc}^{-1}] + 25$. The quantity M_0 is the absolute magnitude of type Ia supernovae, and

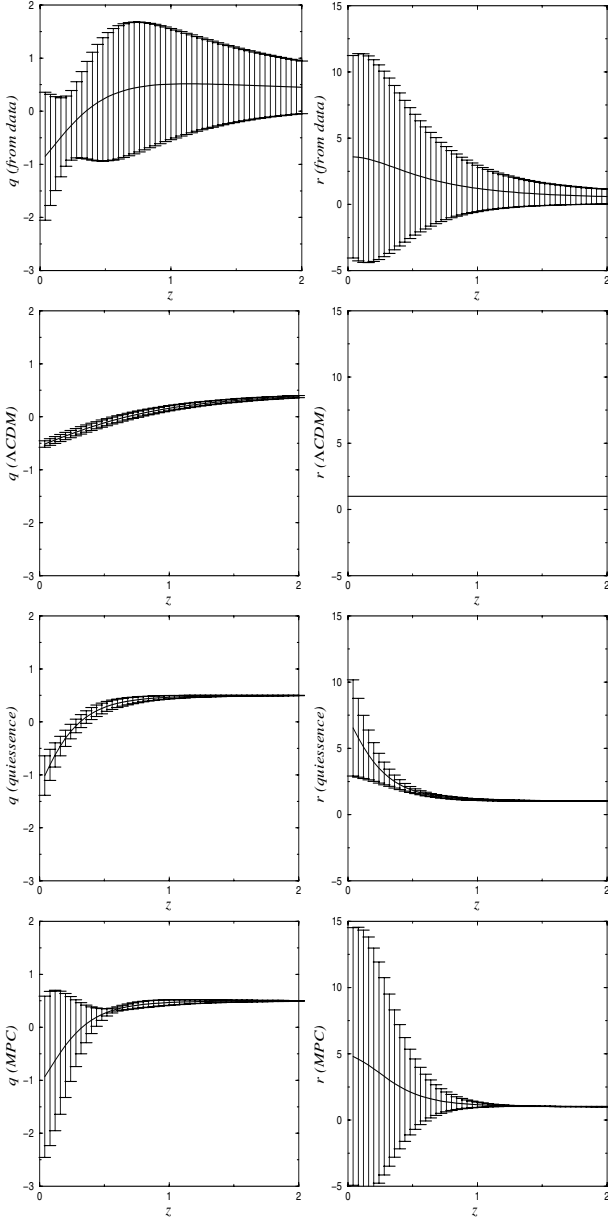


Fig. 10. The deceleration parameter q and the statefinder r extracted from current SNIa data using the Alam parametrization of H (top row), for Λ CDM (second row), quiescence (third row), and the Modified Polytropic Cardassian ansatz (bottom row)

$D_L(z) = H_0 d_L(z)$ is the Hubble constant free luminosity distance. The combination of absolute magnitude and the Hubble constant, \mathcal{M} , can be calibrated by low-redshift supernovae (Hamuy et al. 1993; Perlmutter et al. 1999). The dispersion in the magnitude, σ_{mag} , is related to the uncertainty in the distance, σ , by

$$\frac{\sigma}{d_L(z)} = \frac{\ln 10}{5} \sigma_{\text{mag}}, \quad (69)$$

and for $\sigma_{\text{mag}} = 0.15$, the relative error in the luminosity distance is $\sim 7\%$. If we assume that the d_L we calculate for each z value is the mean of all d_L s in that particular bin, the errors reduce from 7% to $0.07/\sqrt{40} \approx 0.01 = 1\%$. We do not add noise

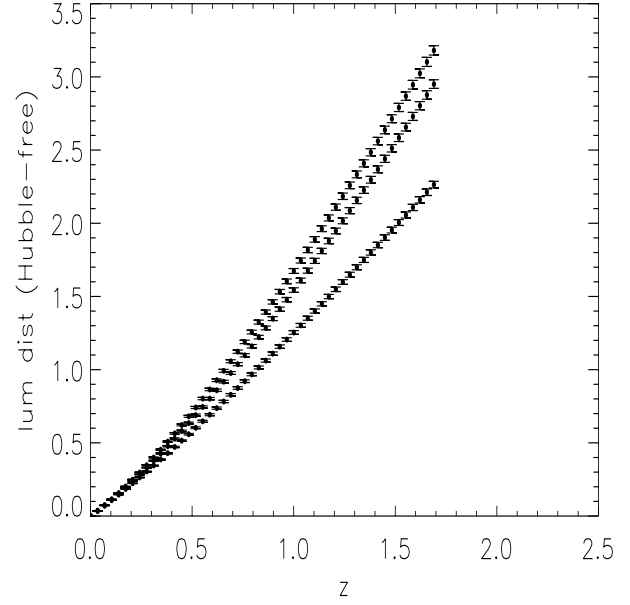


Fig. 11. Binned, simulated data set for a Cardassian model with $\psi = 1$, $n = -1$ (upper curve), a flat Λ CDM universe with $\Omega_{m0} = 0.3$ (middle curve), and for a Generalized Chaplygin Gas with $A_s = 0.4$, $\alpha = 0.7$ (lower curve). The 1σ error bars are also shown.

to the simulated d_L , and hence our results give the ensemble average of the parameters we fit to the simulated data sets.

4.1. A Λ CDM universe

We first simulate data based on a flat Λ CDM model with $\Omega_{m0} = 0.3$, $h = 0.7$, giving the data points shown in the middle curve in Fig. 11. To this data set we first fit the quiescence model, the MPC, the GCG, and the parametrization of H from Eq. (62). Since all models reduce to Λ CDM for an appropriate choice of parameters, distinguishing between them based on the χ^2 per degree of freedom alone is hard. Based on the best-fitting values and error bars on the parameters A_0 , A_1 , and A_2 in Eq. (62) we can reconstruct the statefinder parameters from Eqs. (64)–(66). In Fig. 12 we show the deceleration parameter and statefinder parameters reconstructed from the simulated data. The statefinders can be reconstructed quite well in this case, e.g. we see clearly that r is equal to one, as it should for flat Λ CDM. In Fig. 13 we show the statefinders for a selection of models, obtained by fitting their respective parameters to the data, and using the expressions for q and r for the respective models derived in earlier sections, e.g. Eqs. (46) and (47) for the Chaplygin gas. Since all models reduce to Λ CDM for the best-fitting parameters, their q and r values are also consistent with Λ CDM. Thus, if the dark energy really is LIVE, a SNAP-type experiment should be able to demonstrate this.

4.2. A Chaplygin gas universe

We have also carried out the same reconstruction exercise using simulated data based on the GCG with $A_s = 0.4$, $\alpha = 0.7$, see Fig. 11. Figure 14 shows q and r reconstructed using the parametrization of H . The same quantities for the models

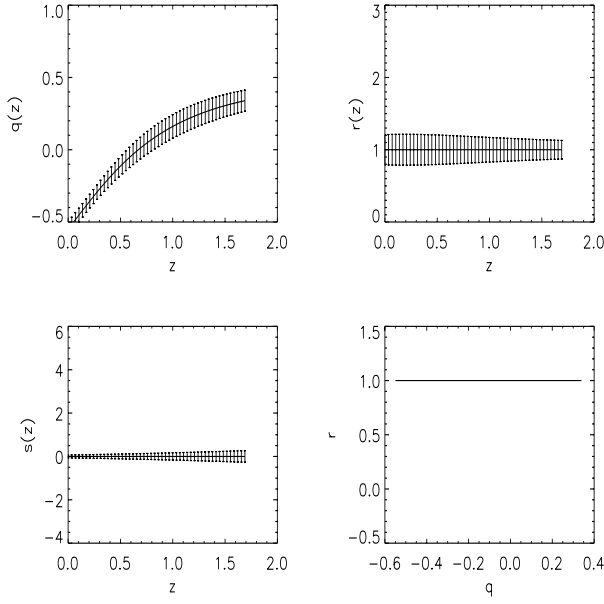


Fig. 12. The statefinder parameters and the deceleration parameter for the best-fitting reconstruction of the simulated data based on Λ CDM, using the parametrization of Alam et al. The 1σ error bars are also shown.

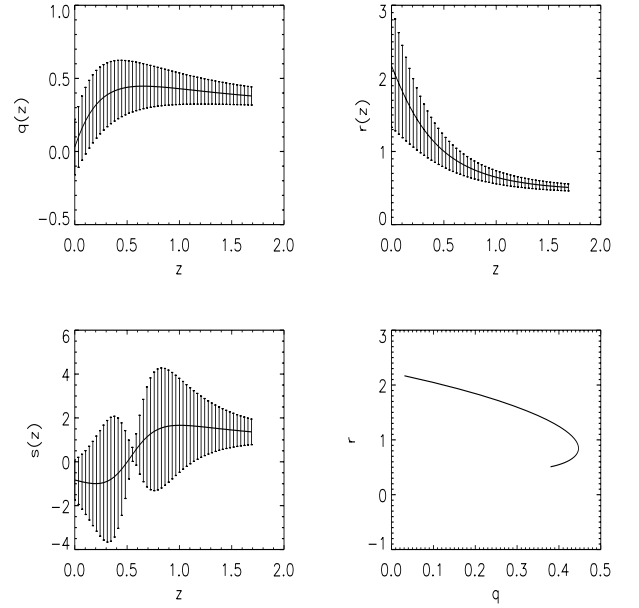


Fig. 14. The statefinder parameters and the deceleration parameter for the best-fitting reconstruction of the simulated data based on the GCG, using the parametrization of Alam et al. The 1σ error bars are also shown.

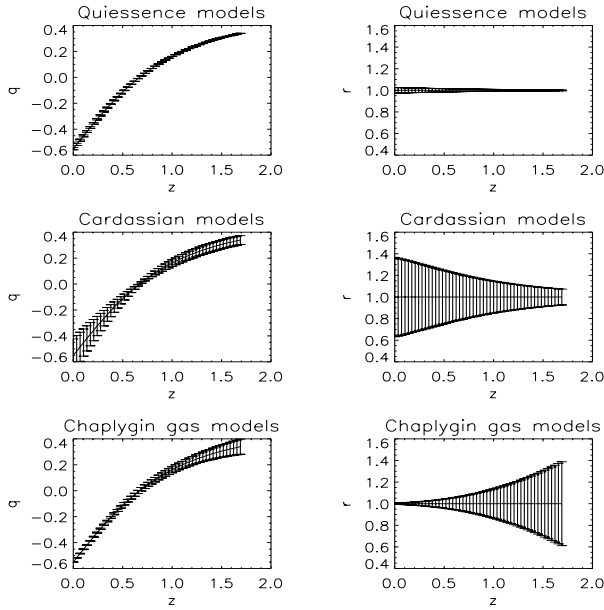


Fig. 13. The statefinder parameters for a selection of models, evaluated at the best-fitting values of their respective parameters to the simulated Λ CDM dataset, with 1σ errors included.

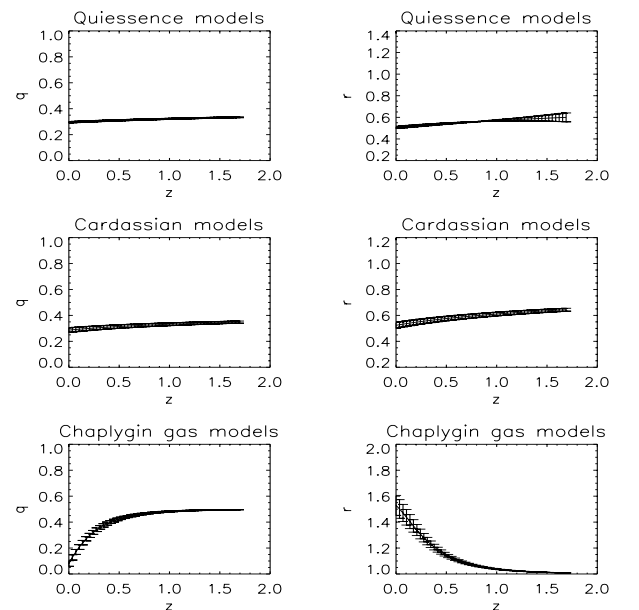


Fig. 15. The statefinder parameters for a selection of models, evaluated at the best-fitting values of their respective parameters to the simulated Chaplygin gas data set, with 1σ errors included.

considered, based on their best-fitting parameters to the simulated data, are shown in Fig. 15. For the Cardassian model, the best-fitting value for the parameter n , n_{bf} , depends on the extent of the region over which we allow n to vary. Extending this region to larger negative values for n moves n_{bf} in the same direction. However, the minimum χ^2 value does not change significantly. This is understandable, since $H(x)$ for the MPC model is insensitive to n for large, negative values of n . The quantities $r(x)$ and $q(x)$ also depend only weakly on the allowed range for n , whereas their error bars are sensitive to this parameter. We

chose to impose a prior $n > -1$, producing the results shown in Fig. 15. The best-fitting values for ψ and n were, respectively, 0.06 and -0.94 .

Figure 16 shows the deceleration parameter extracted from the Alam et al. parametrization (full line), with 1σ error bars. Also plotted is the best fit $q(z)$ from the quiescence (squares), Cardassian (triangles) and Chaplygin (asterisk) models. We note that the $q(z)$ from the Alam et al. parametrization has a somewhat deviating behaviour from the input model, especially

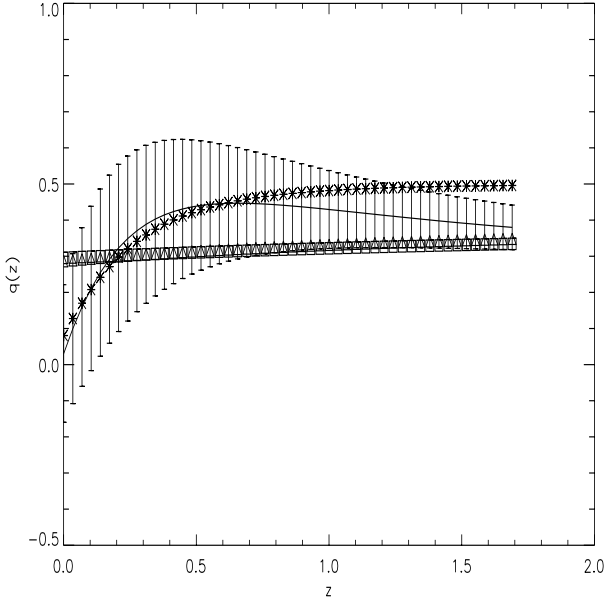


Fig. 16. Comparison of $q(z)$ extracted using the parametrized $H(z)$ with $q(z)$ for the various best-fitting models. The input model is a GCG model with $A_s = 0.4$, $\alpha = 0.7$. Error bars are only shown on the values extracted using the Alam et al. parametrization, but in the other cases they are roughly of the same size as the symbols. See text for more details.

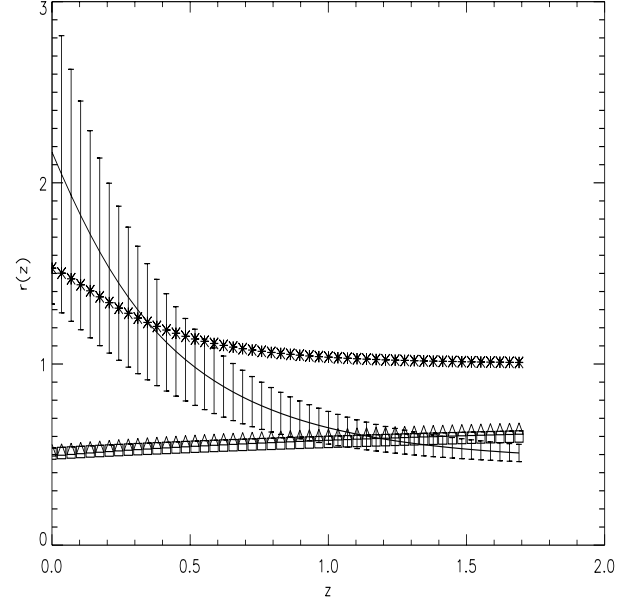


Fig. 17. Comparison of $r(z)$ extracted using the parametrized $H(z)$ with $r(z)$ for the various best-fitting models. The input model is a GCG model with $A_s = 0.4$, $\alpha = 0.7$. Error bars are only shown on the values extracted using the Alam et al. parametrization, but in the other cases they are roughly of the same size as the symbols. See text for details.

at larger z . Also, no model can be excluded on the basis of their predictions for $q(z)$

Figure 17 shows the same situation for the statefinder parameter $r(z)$. Note again that for large z , the recovered statefinder from the Alam et al. parametrization does not correspond well with the input model. As with the case for $q(z)$, the quiescence and Cardassian models follow each other closely. These, however, do not agree with the input model for low values of z (similar to the case for $q(z)$ they diverge for low z). Comparing the statefinder r for the quiescence and Cardassian models with that of the input GCG model, indicates that, not surprisingly, neither of them is a good fit to the data.

4.3. A Cardassian universe

We repeated the analysis described in Sects. 4.1 and 4.2, this time based on an underlying Cardassian model. The values of the input parameters were chosen to be $\psi = 1$, $n = -1$. The luminosity distance for this model is shown in Fig. 11. Figures 18 and 19 show, respectively, the deceleration parameter $q(z)$ and the statefinder $r(z)$ for the input Cardassian model (triangles) compared to the reconstructed parameters (full line) using the Alam et al. parametrization for $H(z)$. For clarity, only the error bars for the reconstructed parameters are shown. As before, the error bars for the input model are roughly the size of the symbols, except in the case of $z = 0-0.7$ for $r(z)$ where they are somewhat larger (up to two symbol sizes in each direction). We see that the deceleration parameter is reconstructed quite well. However, the behaviour of the reconstructed $r(z)$ does not seem to agree well with the input model, although the input model is more or less within the 1σ errors bars of the

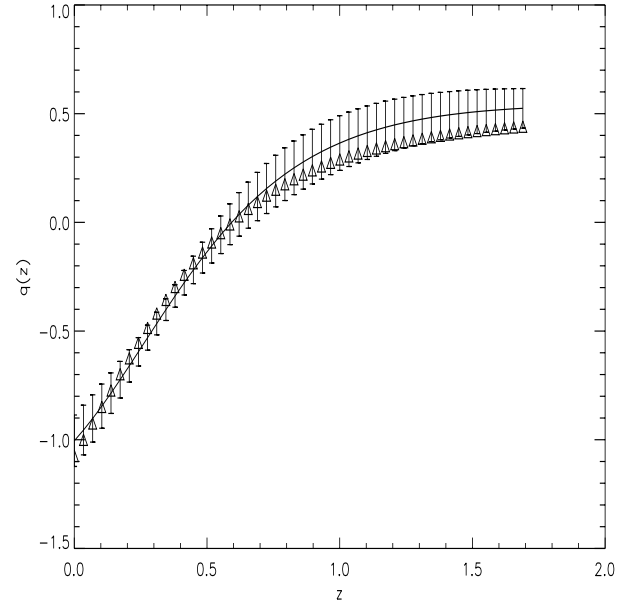


Fig. 18. Comparison of $q(z)$ extracted using the parametrized $H(z)$ with $q(z)$ for the input Cardassian model.

reconstructed statefinder. For the Cardassian universe, the discrepancy between input and reconstructed parameter is most conspicuous for low z ($z < 0.7$). This further corroborates the conclusion in Sect. 4.2 that a better parametrization for $H(z)$ is needed. The best fit quiescence and Chaplygin gas models are not shown in these figures. We only remark in passing that with the quiescence model we managed to reproduce the input model quite well, while the Chaplygin gas model was a very poor fit to these simulated data.

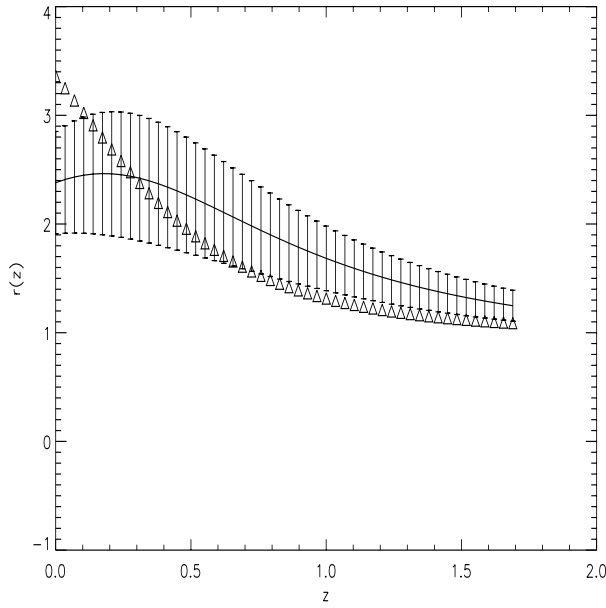


Fig. 19. Comparison of $r(z)$ extracted using the parametrized $H(z)$ with $r(z)$ for the input Cardassian model.

The exercises in this subsection and the previous one indicate that there are potential problems with extracting the statefinders from data in a reliable, model-independent way. The fact that r extracted from the simulated data using the Alam et al. parametrization deviates from $r(z)$ for the input model in the two cases, indicates that one needs a better parametrization in order to use statefinder parameters as empirical discriminators between dark energy models. In fact, a potential problem with this approach is that since the equation governing the expansion of the Universe is a second-order differential equation, all derivatives of dynamical variables of order higher than the second have intrinsic correlations. In the case of the statefinders, Eq. (15) shows that r is correlated with q . When extracting statefinders from data, one always has to parametrize some quantity, e.g. H , and it is hard to do this without introducing bias in the correlation between r and q .

5. Conclusions

We have investigated the statefinder parameters as a means of comparing dark energy models. As a theoretical tool, they are useful for visualizing the behaviour of different dark energy models. Provided they can be extracted from the data in a reliable, model-independent way, they can give a first insight into the type of model which is likely to describe the data. However, SNIa data of quality far superior to those presently available are needed in order to distinguish between the different models. And even with SNAP-quality data, there may be difficulties in distinguishing between models based on the statefinder parameters alone.

Furthermore, there are potential problems in reconstructing the statefinders from observations as shown in Sects. 4.2 and 4.3. A similar conclusion was reached in a recent investigation by Jönsson et al. (2004) (but contested by Alam et al. 2004), where they considered reconstruction of the equation of

state $w(x)$ from SNIa data using Eq. (67). They found that this parametrization forces the behaviour of $w(x)$ onto a specific set of tracks, and may thus give spurious evidence for redshift evolution of the equation of state. Since there are intrinsic correlations between the statefinders, finding an unbiased reconstruction procedure, and demonstrating that it really is so, is likely to be very hard.

Acknowledgements. We acknowledge support from the Research Council of Norway (NFR) through funding of the project 159637/V30 “Shedding Light on Dark Energy”. The authors wish to thank Håvard Alnes for interesting discussions and the anonymous referee for valuable comments and suggestions.

References

- Alam, U., Sahni, V. 2002 [arXiv:astro-ph/0209443]
- Alam, U., Sahni, V., Saini, T. D., Starobinsky, A. A. 2003, MNRAS, 344, 1057
- Alam, U., Sahni, V., Saini, T. D., Starobinsky, A. A. 2004 [arXiv:astro-ph/0406672]
- BBento, M. C., Bertolami, A. A., Sen, A. A., 2002, Phys. Rev. D, 66, 043507
- Bertolami, O., Sen, A. A., Sen, S., Silva, P. T., 2004, MNRAS, in press [arXiv:astro-ph/0402387]
- Bilic, N., Tupper, G. G., Viollier, R. 2002, Phys. Lett. B, 535, 17
- Bucher, M., Spergel, D. 1999, Phys. Rev. D, 60, 043505
- Caldwell, R. R. 2002, Phys. Lett. B, 545, 23
- Caldwell, R. R., Kamionkowski M. 2004, preprint [arXiv:astro-ph/0403003]
- Chiba, T., Nakamura T. 1998, Prog. Theor. Phys., 100, 1077
- Deffayet, C. 2001, Phys. Lett. B, 502, 199
- Deffayet, C., Dvali, G., Gabadadze, G. 2002, Phys. Rev. D, 65, 044023
- Dvali, G., Gabadadze, G., Porrati, M. 2000, Phys. Lett. B, 485, 208
- Efstathiou, G., Moody, S., Peacock, J. A., et al. 2002, MNRAS, 330, L29
- Eichler, D. 1996, ApJ, 468, 75
- Freese, K., Lewis, M. 2002, Phys. Lett. B, 540, 1
- Gondolo, P., Freese, K. 2003, Phys. Rev. D, 68, 063509
- Gong, Y. 2004, preprint [arXiv:astro-ph/0405446]
- Gorini, V., Kamenshchik, A., Moschella U. 2003, Phys. Rev. D, 67, 063509
- Hamuy, M., Maza, J., Phillips, M. M., et al. 1993, AJ, 106, 2392
- Jeffreys, H. 1961, Theory of probability, 3rd ed. (Oxford University Press)
- Jönsson, J., Goobar, A., Amanullah, R., Bergström, L. 2004, preprint [arXiv:astro-ph/0404468]
- Kamenshchik, A., Moschella, U., Pasquier, V. 2001, Phys. Lett. B, 511, 265
- Liddle, A. 2004, MNRAS, 351, L49
- Padmanabhan, T. 2002, Phys. Rev. D, 66, 021301
- Padmanabhan, T., Choudhury, R. 2003, MNRAS, 344, 823
- Peebles, P. J. E., Ratra, B. 1988, ApJ, 325, L17
- Perlmutter, S., Aldering, G., Goldhaber, G., et al. 1999, ApJ, 517, 565
- Riess, A. G., Filippenki, A. V., Challis, P., et al. 1998, AJ, 116, 1009
- Riess, A. G., Matsubara, T., Szalay, A. S., et al. 2004, ApJ, 607, 655
- Sahni, V., Shtanov, Y. 2003, JCAP, 0311, 014
- Sahni, V., Saini, T. D., Starobinsky, A. A., Alam, U. 2003, JETP Lett., 77, 201
- Saini, T. D., Weller, J., Bridle S. L. 2004, MNRAS, 348, 603
- Schwarz, G. 1978, Ann. Stat., 6, 461
- Solheim, J.-E. 1966, MNRAS, 133, 32
- Tegmark, M., Strauss, M. A., Blanton, M. R., et al. 2004, Phys. Rev. D, 69, 103501
- Visser, M. 2004, Class. Quant. Grav., 21, 2603
- Wetterich, C. 1988, Nucl. Phys. B, 302, 668